Monthly Scientific-Technical and Production Journal

The Paton WELDING JOURNAL

January
2001
1

English translation of the monthly «Avtomaticheskaya Svarka» journal published in Russian since 1948

The National Academy of Sciences of Ukraine
The E.O. Paton Electric Welding Institute of the NAS of Ukraine
International Association «Welding»

«The Paton Welding Journal»
is published monthly by the
International Association «Welding»

Promotion group:
V.N.Lipodaev, V.I.Lokteva
A.T.Zelnichenko (Exec. director)
Translators:
S.A.Fomina, I.N.Kutianova,
T.K.Vasilenko

Editorial and advertising offices
are located at PWI,
International Association «Welding»,
11, Bozhenko str., 03680,
Kyiv, Ukraine
Tel.: (38044) 227 67 57
Fax: (38044) 268 04 86
E-mail: tomik@mac.relc.com
E-mail: office@paton.kiev.ua

State Registration Certificate
KV 4790 of 09.01.2001

Subscriptions:
$460, 12 issues, postage included

«The Paton Welding Journal» Website:
http://www.nas.gov.ua/pwj

CONTENTS

NUMERICAL STUDIES OF THERMOMECHANICAL PROCESSES IN SURFACING OF SHAFTS OF SHIP MECHANISMS

V.I. MAKHNENKO[1], **E.A. VELIKOIVANENKO**[1], **T.G. KRAVTSOV**[2] and **V.V. SEVRYUKOV**[3]
[1]The E.O. Paton Electric Welding Institute, NASU, Kyiv, Ukraine
[2]Odessa State Marine Academy, Odessa, Ukraine
[3]Ministry of Transportation of Ukraine, Kyiv, Ukraine

ABSTRACT

Calculation method is presented for evaluation of the range of optimal parameters for the technology of corrosion-resistant surfacing of shafts in ship mechanisms and systems. The method is based on taking into account the potential formation of fatigue cracks at cyclic loading in service.

Key words: *shafts of ship mechanisms, surfacing, defects, hot and cold cracks, microstructures, residual stresses, fatigue resistance*

Surfacing of parts of the shaft assembly in ship mechanisms and systems, both in manufacturing and restoration, traditionally has been an effective method for extension of their service life [1, 2, etc.]. Intensive development has been conducted in this field in FSU territory over the last 50 years [1 – 4]. Significant results have been achieved in research and its practical application. With progress of engineering, application of more perfect structural materials, increase of service requirements to the parts under consideration, however, a whole range of new problems are encountered, whose solution requires a rather dedicated effort in development of the appropriate technologies.

Use of purely experimental methods for these purposes involves a considerable amount of funds and time (a surfacing process normally has many more controllable parameters, than a welding process). In this connection quite understandable is the increased interest to numerical modelling of the main physical phenomena in surfacing, depending on the initial conditions and process parameters [5, 6, etc.].

The paper sets forth the procedure of such modelling for the case of deposition of a protective or wear-resistant layer onto a shaft of a heat-hardenable steel of high or increased strength. Unlike [5], which considers the thermal and deformational processes in deposition of a protective layer onto a shaft (pipe) of an unalloyed steel, the paper describes a calculation algorithm constructed by the authors, taking into account the possible kinetics of microstructural changes, both in the HAZ and in the deposited layer.

Calculation algorithms for forecasting microstructural changes in the base material (HAZ) and penetration zone were constructed using a quite well-established approach [7, 8], based on forecasting the weight fractions v_j of the main microstructural constituents: austenite ($j = a$), ferrite ($j = f$), pearlite ($j = p$), bainite ($j = b$), martensite ($j = m$). The features of the fine structure, grain boundary morphology, impurities distribution, etc. were neglected. The latter, in the authors' opinion, has a slight influence on thermomechanical processes considered in the paper, which, however, does not make their description less interesting in the appropriate investigations [9, etc.], but this is beyond the scope of this paper.

The gained experience [2, 4] shows that the main problems in shaft surfacing are related to providing the required resistance of the surfaced shaft to fatigue loads. Unfavourable residual stresses, microstructures and mechanical properties developing during surfacing, as well as defects in the form of hot (cold) cracks in the surfacing zone, can significantly lower the fatigue properties of the surfaced part. Therefore, one of the chief goals in selection of rational conditions for this process is obtaining through computer means, predicable results on the above factors for concrete modes and conditions. These results allow making some judgement on the quality of the surfaced part and, thus essentially reducing the scope of experiments when searching for optimal variants of the technology.

Proceeding from these goals, the procedure envisages the following steps: the specified dimensions of the shaft (diameter d, length L), modes of arc surfacing along a helix (welding current I, arc voltage U_a, surfacing speed v_s, surfacing step H, thickness of surfaced layer δ, electrode wire feed rate v_f and its diameter d_e), as well as thermophysical properties of the base and surfacing materials (heat conductivity λ, heat capacity per unit volume c_γ, solidus T_S and liquidus T_L temperatures) are used to calculate temperature fields $T(r, z, \beta, t)$ in the base and the deposited metal, where t is time; r, z, β are space coordinates of appropriate points of the shaft and the deposit [10]. The dimensions of the penetration zone are determined based on known values of $T(r, z, \beta, t)$, which permits calculation of its average composi-

tion, allowing for that of the base and filler metals, as well as of the deposited layers and the adjacent beads [10].

Kinetic changes of microstructural condition $v_j(t)$ in each point of the shaft being surfaced, are found from composition and thermal cycles, allowing for appropriate diagrams of anisothermal decay of austenite (ADA) or Schaeffler–DeLong diagrams. Unlike [10, 11] in this study, the calculation algorithm for $v_j(t)$ determination allows for the probability of a complex thermal cycle in surfacing along a small lead helix.

For a complex thermal cycle (Figure 1) the approach of [10, 11] can be used without any changes for forecasting $v_j(t)$ in the first stage of this cycle, when $0 < t < t_{\min 1}$ (Figure 1). At $t > t_{\min 1}$, various variants of changing $v_j(t)$ are possible. If $T(t_{\min 1}) < T_e^m$, then at $t > t_{\min 1}$ $dv_j \equiv 0$. If $T(t_{\min 1}) > T_e^m$, then for $j = f, p, b$ further transformation is possible at $t > T_{\min 1}$. For $j = m$ it stops, until the temperature has dropped to the temperature $T < T(t_{\min 1})$.

According to [10, 11] for a simple cycle at $dT/dt < 0$ in the interval of $T_s^j > T > T_e^j$, value $v_j(t) = v_j(T)$ is calculated in the following form:

$$v_j(t) = v_{j\max}\, f_j(T). \qquad (1)$$

Values of $v_{j\max}$ for low- and medium-alloyed steels are found from ADA diagram at $T < T_e^j$ [12, 13], or with sufficient engineering accuracy through $t_{8/5}$ and two points of this ADA diagram — τ_{50}^j and τ_{85}^j, corresponding to the time of cooling from 800 to 500 °C, at which $v_j = 0.50$ and 0.85, respectively.

For instance, according to [7]

$$v_{j\max} = \frac{1}{2}\left[1 + \operatorname{erf}\left(\frac{\ln t_{8/5}/\ln \tau_{50}^j}{S_j}\right)\right], \qquad (2)$$

where $S_j = \sqrt{2}\,\ln \dfrac{\tau_{85}^j}{\tau_{50}^j}$.

In keeping with [10], $f_j(T)$ is taken to have the form of

$$f_j(T) = 1 - \exp\left(-k_j \frac{T_s^j - T}{T_s^j - T_e^j}\right) \text{ at } T_s^j > T > T_e^j, \qquad (3)$$

where $k_j = 2.5 - 3.0$ is the coefficient.

$f_j(T) = 0$ at $T > T_s^j$.

For high-alloyed steels $v_{j\max}$ is found from Schaeffler–DeLong type diagram. In this case $f_j(T)$ has the form of expression (3) only for martensite, and $T_s^j = T_e^j = T_L$ can be assumed for δ-ferrite. It is more convenient to calculate the values of T_s^m and T_e^m, depending on the composition, according to [14]. So, at $0.05 \le C \le 0.35$

$$T_s^m = 454 - 210\ C + \frac{4.2}{C} - A_1 Ni - A_2 Mn - A_3 Cr_{eq} - 21 Cu, \qquad T_e^m \approx T_s^m - 126, \qquad (4)$$

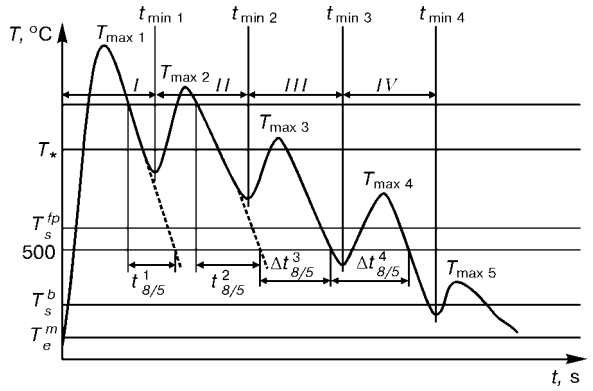

Figure 1. Schematic of a complex thermal cycle in shaft surfacing along a small lead spiral

$$A_1 = 21, \quad A_2 = 10.5, \quad A_3 = 16.8 \text{ at Ni} > 5\ \%,$$

$$A_1 = \left(1.6\ \text{Ni} + \frac{65}{\text{Ni}}\right), \quad A_2 = 10.5,$$

$$A_3 = 16.8 \text{ at } 1.4 < \text{Ni} < 5\ \%,$$

$$A_1 = 27, \quad A_2 = 7.8, \quad A_3 = 9.5 \text{ at Ni} < 1.4\ \%,$$

where C, Ni, Cu is the weight fraction, %, of the respective elements; Cr_{eq} is the equivalent of chromium content, equal to

$$Cr_{eq} = Cr + Mo + 1.5\ Si. \qquad (5)$$

The above is valid for a section of the thermal cycle with $0 < t < t_{\min 1}$. At $t > t_{\min 1}$ the rules for a simple thermal cycle are disturbed. For a complex thermal cycle it is proposed to use the method of conditional simple cycles (see Figure 1): *I* cycle at $0 < t < t_{\min 1}$, *II* — at $t_{\min 1} < t < t_{\min 2}$, etc.

Each *i*-th cycle has the maximal heating temperature $T_{\max i}$ and initial microstructural state at the moment $t = t_{\min(i-1)}$, duration $t_{8/5}^j$ (cycles *I* and *II* in Figure 1), as well as time of staying above 500 °C — $\Delta t_{8/5}^j$ at $T_{\max i} < T_*$ (T_* is the temperature of the start of austenite decomposition).

If for any cycle $T_{\max i} > T_*$, the principal rules of the simple cycle can be used for it, i.e. it can be assumed that at the stage of heating up to $T \le T_*$ the initial structures are preserved at $t = t_{\min(i-1)}$. This is attributable to the fact that heating duration for such a simple cycle is usually short, compared to cooling, and relationships (1) and (4) are valid at the stage of the latter. A not very complicated rule holds for the conditionally simple *i*-th cycle, if $T_{\max i} < 500$ °C, and $T(t_{\min(i-1)}) < T_s^m$ (see Figure 1). In this case there is no reason to anticipate any further diffusion transformations of austenite, i.e. the microstructure recorded at the moment $t_{\min(i-1)}$, remains unchanged, until the temperature in this cycle has dropped below $T(t_{\min(i-1)})$, when intensive martensite transformation goes on till $T = T_e^m$. It is natural that, if $T(t_{\min(i-1)}) < T_e^m$, transformations in such conditionally simple cycles ($T_{\max i} < 500$ °C) are absent.

The situation is more complex when $T_* > T_{\max i} < 500$ °C. In this case time $t_{8/5}^{j-1}$ of the previous cycle

Table 1. Element content in materials used, wt.%

Material	*C*	*Mn*	*Si*	*Cr*	*Ni*	*Mo*	*Nb*	*S*	*P*
Steel 35	0.33	0.80	0.36	0.07	0.06	–	–	0.030	0.01
PP-AN163	0.07	2.00	0.90	13.00	3.00	2.00	–	< 0.012	< 0.04
Sv-08Kh20N9S2BTYu	0.07	1.36	2.16	19.60	9.42	–	0.82	< 0.012	< 0.04

Table 2. Initial parameters for different surfacing variants

Variant number	*Shaft diameter, mm*	*Layer number*	*Bead thickness, mm*	*Filler material*	*Modes of arc surfacing*						
					d_e, *mm*	v_f, *m/h*	*H, mm*	*I, A*	U_a, *V*	v_s, *cm/s*	q_h, *cal/cm*
1	72	1 – 4	1.5	A	1.2	200	4.0	110	28	0.7	650
2	72	1 – 3	1.5	M	1.2	200	4.0	120	26	0.7	650
3	72	1	1.5	M	1.2	200	4.0	120	26	0.7	650
		2, 3	1.5	A	1.2	200	4.0	110	28	0.7	650
4	300	1, 2	3.0	A	2.0	140	10.0	280	29	0.5	2730
5	300	1	3.0	M	2.0	140	10.0	280	29	0.5	2730
		2	3.0	A	2.0	140	10.0	280	29	0.5	2730

Note: A – Sv-08Kh20N9S2BTYu; M – PP-AN163.

Table 3. Mechanical and thermophysical properties of materials used

T, °C	*Steel 35*			*Austenite*			$\sigma_y(T)/\sigma_y(20\ ^\circ C)$ *for*			
	$E\cdot10^{-5}$, *MPa*	λ, *J/(cm·°C)*	c_γ, *J/(cm³·°C)*	$E\cdot10^{-5}$, *MPa*	$\lambda\cdot10^{2}$, *J/(cm·°C)*	c_γ, *J/(cm³·°C)*	*austenite*	*martensite*	*bainite*	*ferrite, pearlite*
20	2.12	0.52	3.79	1.97	0.13	3.60	1.00	1.00	1.00	1.00
100	2.08	0.50	3.85	1.97	0.15	3.90	0.92	0.92	0.92	0.94
150	2.05	0.50	3.99	1.88	0.16	4.05	0.88	0.90	0.90	0.90
200	2.03	0.48	4.08	1.84	0.17	4.21	0.83	0.88	0.87	0.87
250	2.00	0.47	4.13	1.81	0.17	4.25	0.79	0.86	0.86	0.86
300	4.90	0.45	4.38	1.77	0.18	4.29	0.75	0.84	0.84	0.85
350	1.93	0.44	4.58	1.73	0.18	4.35	0.68	0.82	0.82	0.83
400	1.89	0.42	4.65	1.68	0.19	4.42	0.62	0.80	0.80	0.80
450	1.83	0.40	5.00	1.64	0.20	4.42	0.56	0.75	0.76	0.76
500	1.77	0.38	5.21	1.60	0.20	4.42	0.50	0.70	0.73	0.72
550	1.70	0.36	5.42	1.56	0.21	4.46	0.45	0.63	0.65	0.64
600	1.63	0.33	5.62	1.52	0.22	4.50	0.39	0.56	0.56	0.56
650	1.51	0.32	5.88	1.48	0.23	4.54	0.35	0.42	0.43	0.43
700	1.40	0.30	6.31	1.43	0.23	4.58	0.31	0.28	0.30	0.31
750	1.40	0.27	13.26	1.37	0.23	4.68	0.28	0.18	0.20	0.25
800	1.40	0.25	4.38	1.30	0.24	4.79	0.25	0.08	0.10	0.20
850	1.40	0.25	4.50	1.19	0.25	4.85	0.22	0.08	0.10	0.20
900	1.40	0.26	4.57	1.08	0.26	4.92	0.20			
950	1.40	0.26	4.67	0.95	0.27	4.96	0.15			
1000	1.40	0.27	4.90	0.82	0.27	5.00	0.10			
1050	1.40	0.27	4.92	0.57	0.28	5.00	0.07			
1100	1.40	0.28	4.96	0.32	0.29	5.00	0.05			
1150	1.40	0.29	5.04	0.20	0.30	5.00	0.04			
1200	1.40	0.30	5.17	0.07	0.30	5.00	0.03			

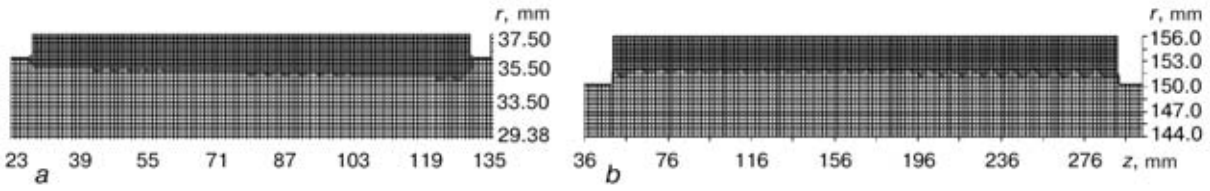

Figure 2. Examples of computation of the penetration zone for first layer of variant No.1 at D = 72 mm (a) and after second layer for variant No.4 at D = 300 mm (b)

increases by value $\Delta t^{j}_{8/5}$, i.e. $t^{j}_{8/5} = t^{j-1}_{8/5} + \Delta t^{j}_{8/5}$. This value of $\Delta t^{j}_{8/5}$ is used to determine $\Delta v_j(t)$ relative to the initial condition at $t = t_{\min(i-1)}$ by the simple cycle rules, according to expressions (1) – (5). We assume $v_a = v_a(t_{i-1})$ in the initial condition, instead of $v_a = 1$, as in equation (2).

When $v_j(t)$ is known, it is possible to determine all the required initial data for calculation of the kinetics of stresses and strains [15, 16]. So, the function of free relative elongation

$$\varphi = \frac{\sum\limits_{j} v_j(T)\,\gamma_j(T) - \sum\limits_{j} v_j(T_0)\,\gamma_j(T_0)}{3\sum\limits_{j} v_j(T_0)\,\gamma_1(T_0)}, \qquad (6)$$

where $\gamma_j(T)$ is the volume of one gram of mass of j-th microstructure at temperature T; T_0 is the initial temperature.

According to experimental data [17]

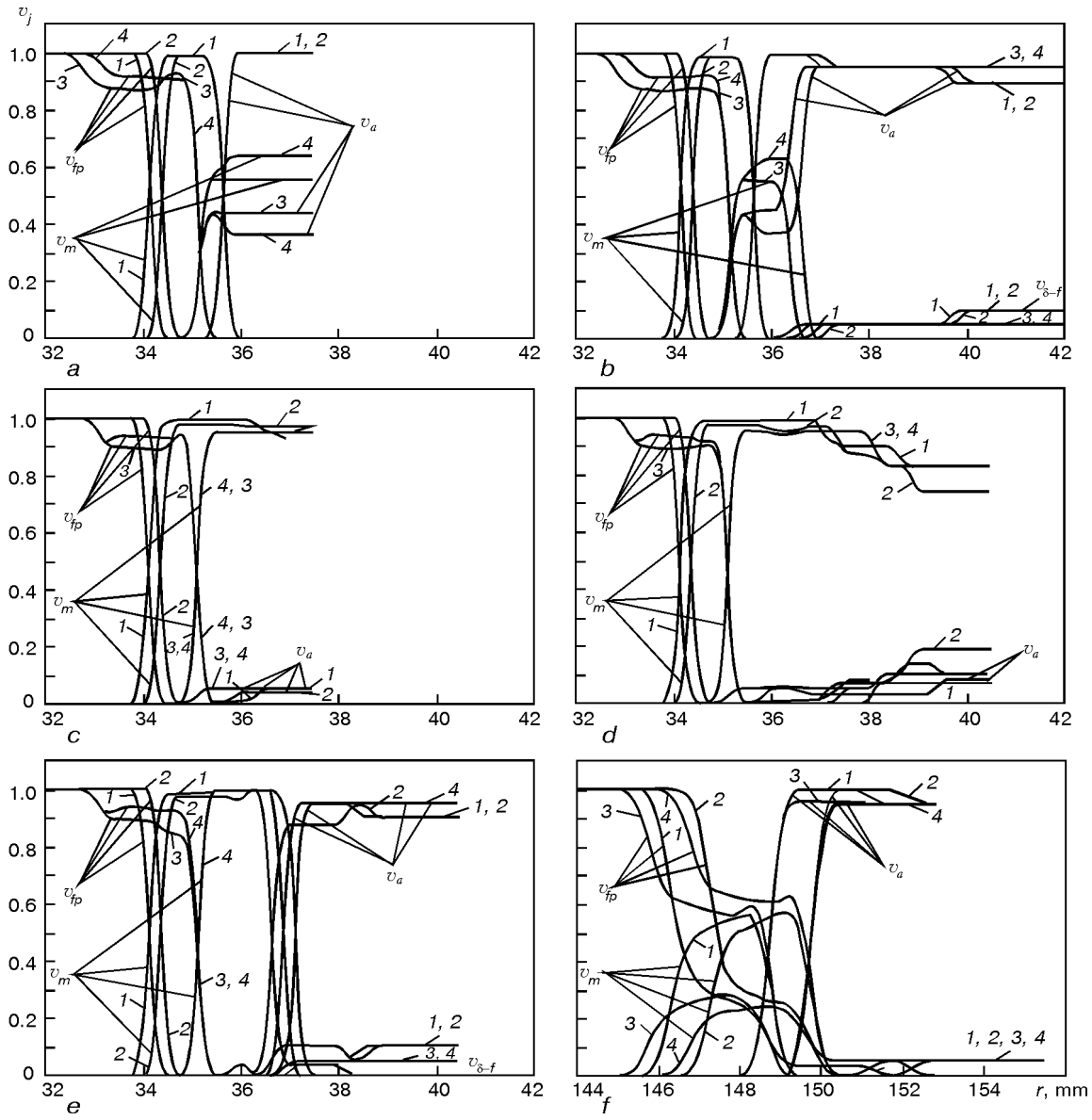

Figure 3. Distribution of weight fractions v_j in the microstructure along radius r in different sections with z = const of the shaft for variant No.1 in layers *1* (a) and *4* (b), variant No.2 in layers *1* (c) and *3* (d), variant No.3 in layer *3* (e) and variant No.4 in layer *2* (f) at D = 72 (a – e) and 300 mm (f); for designations *1* – *4* see the text

Table 4. Composition of the penetration zone

Surfacing variant No.	Parameter	Section No. 1 I	1 II	1 III	2 I	2 II	2 III	3 I	3 II	3 III	4 I	4 II	4 III
1	Cr_{eq}, %	17.21	14.04	12.41	21.02	19.22	17.59	22.32	21.40	17.59	22.86	22.40	21.73
	Ni_{eq}, %	11.71	11.45	11.32	12.02	11.87	11.74	12.12	12.05	11.96	12.17	11.87	11.74
	κ_W	1.26	1.02	1.28	1.54	1.40	1.48	1.63	1.56	1.59	1.67	1.64	1.59
3	Cr_{eq}, %	12.41	10.42	9.22	19.62	18.29	16.61	21.98	19.20	20.13			
	Ni_{eq}, %	7.17	7.71	8.03	10.53	10.49	10.29	11.62	11.50	11.29			
	κ_W	–	–	–	1.68	1.55	1.42	1.69	1.64	1.58			
4	Cr_{eq}, %	16.85	16.28	14.80	20.82	20.73	20.00						
	Ni_{eq}, %	11.68	11.63	11.51	12.00	12.00	11.94						
	κ_W	1.54	1.19	1.10	1.52	1.52	1.46						
5	Cr_{eq}, %	12.15	12.15	11.27	19.57	19.64	18.75						
	Ni_{eq}, %	7.24	7.24	7.47	20.54	10.58	10.42						
	κ_W	–	–	–	1.67	1.67	1.61						

Note: *I* – beginning of deposit (1st bead), *II* – middle (15th bead), *III* – end (25th bead).

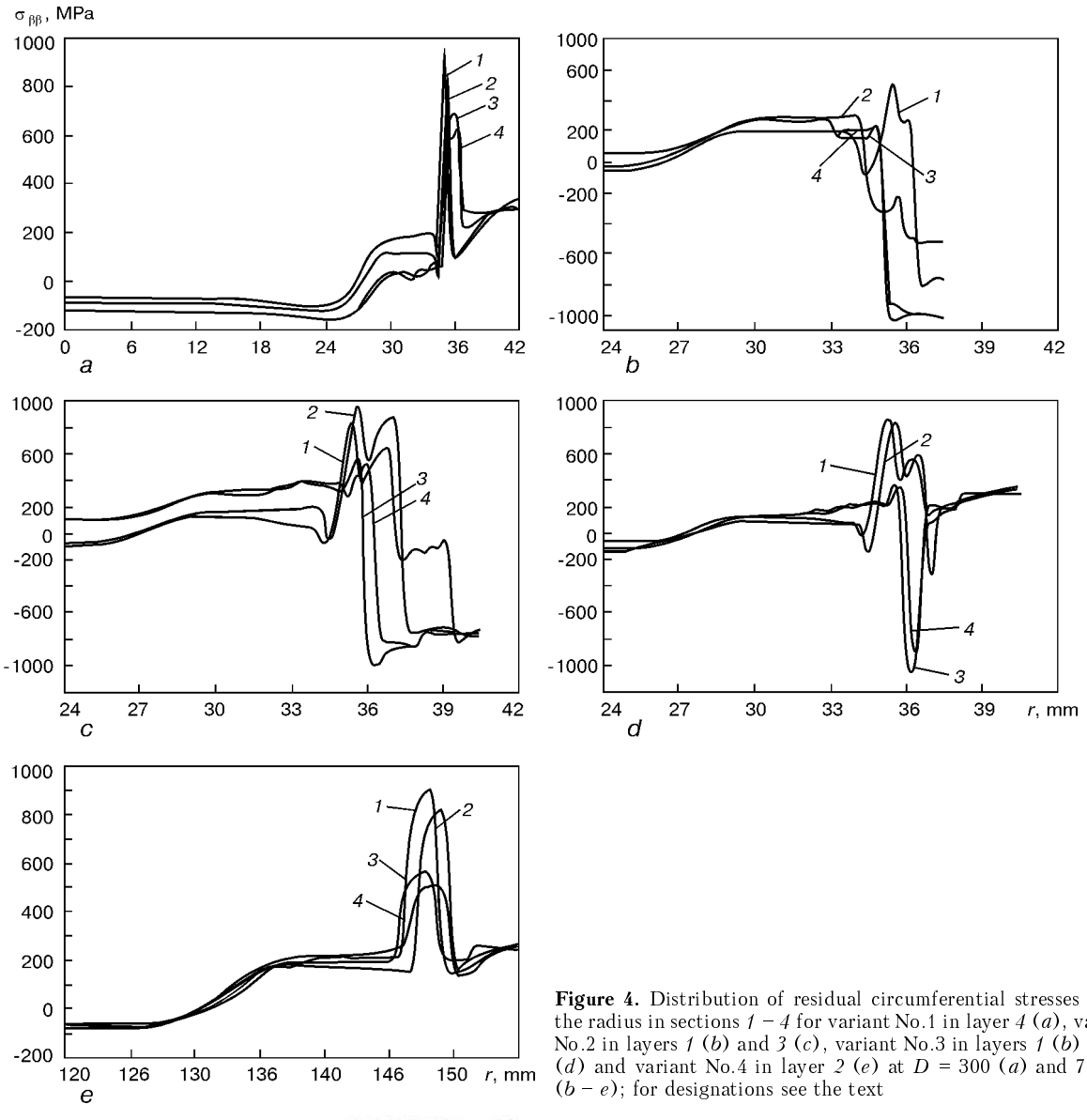

Figure 4. Distribution of residual circumferential stresses along the radius in sections *1* – *4* for variant No.1 in layer *4* (*a*), variant No.2 in layers *1* (*b*) and *3* (*c*), variant No.3 in layers *1* (*b*) and *3* (*d*) and variant No.4 in layer *2* (*e*) at D = 300 (*a*) and 72 mm (*b* – *e*); for designations see the text

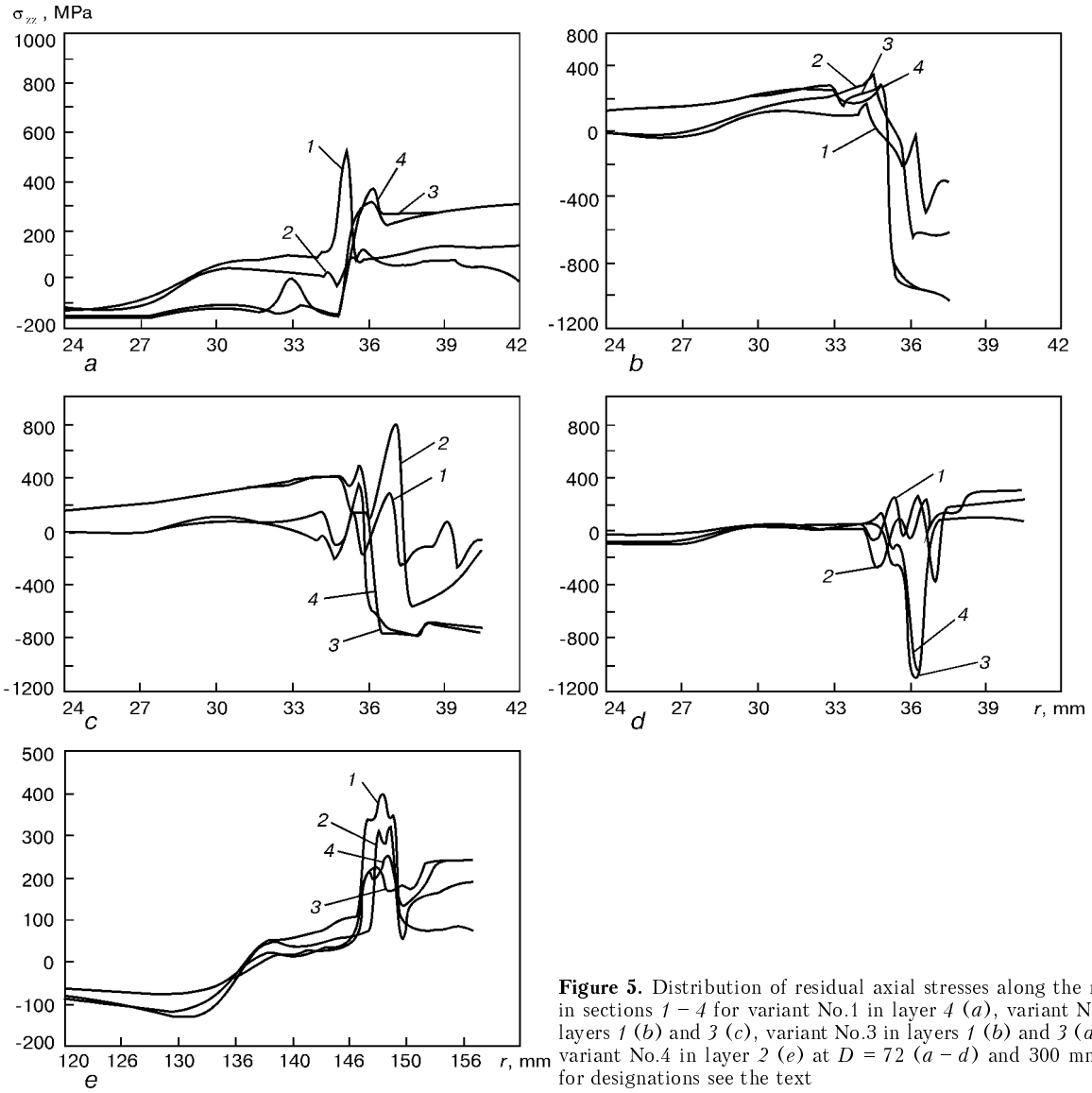

Figure 5. Distribution of residual axial stresses along the radius in sections *1* – *4* for variant No.1 in layer *4* (*a*), variant No.2 in layers *1* (*b*) and *3* (*c*), variant No.3 in layers *1* (*b*) and *3* (*d*) and variant No.4 in layer *2* (*e*) at D = 72 (*a* – *d*) and 300 mm (*e*); for designations see the text

$$\gamma_a = 0.12282 + 8.36\cdot10^{-6}(T + 273) + 2.15\cdot10^{-6}\ \text{C, cm}^3/\text{g},$$
$$\gamma_m = 0.12708 + 4.448\cdot10^{-6}(T + 273) + 2.79\cdot10^{-6}\text{C, cm}^3/\text{g}, \quad (7)$$
$$\gamma_f \approx \gamma_p \approx \gamma_b = 0.12708 + 5.528\cdot10^{-6}(T + 273), \text{ cm}^3/\text{g}.$$

The yield point is calculated from the following equation:

$$\sigma_y(T) = \sum_j \sigma_y^j(T)\, v_j(T), \quad (8)$$

where $\sigma_y^j(T)$ is the yield point of the appropriate phase (j = a, f, p, b, m) at temperature T [10].

A whole range of other macroscopic properties can be also synthesised (thermophysical, etc.) in a similar fashion.

Given below are the results of applying the described approach in calculation of temperatures, microstructures and stresses (strains) in surfacing along a small lead helix the models of shafts of steel 35 with high-alloyed filler materials PP-AN163 (07Kh12N3M2G2S) and Sv-08Kh20N9S2BTYu, the composition of which is given in Table 1.

A computer program for numerical solution of similar problems has been developed at the E.O. Paton Electric Welding Institute. The program has a standard interface, which takes care for the user of all the issues related to numerical solution (selection of finite elements, time steps, etc.) and presentation of calculation results in a form convenient for engineering analysis.

For individual variants of surfacing the shaft models, the calculated distributions of σ_{rr} and $\sigma_{\beta\beta}$ residual stresses were compared with experimental measurement results, obtained when boring and turning the discs cut out of the surfaced shafts [18]. As such cutting of discs involves a significant relaxation of σ_{zz} stresses and partial relaxation of σ_{rr} and $\sigma_{\beta\beta}$ stresses, this operation was also modelled numerically, which was followed by comparison of the derived data.

Given below are some results of numerical calculation for three variants of surfacing a model of shafts of 70 – 72 mm diameter and two variants for 300 mm

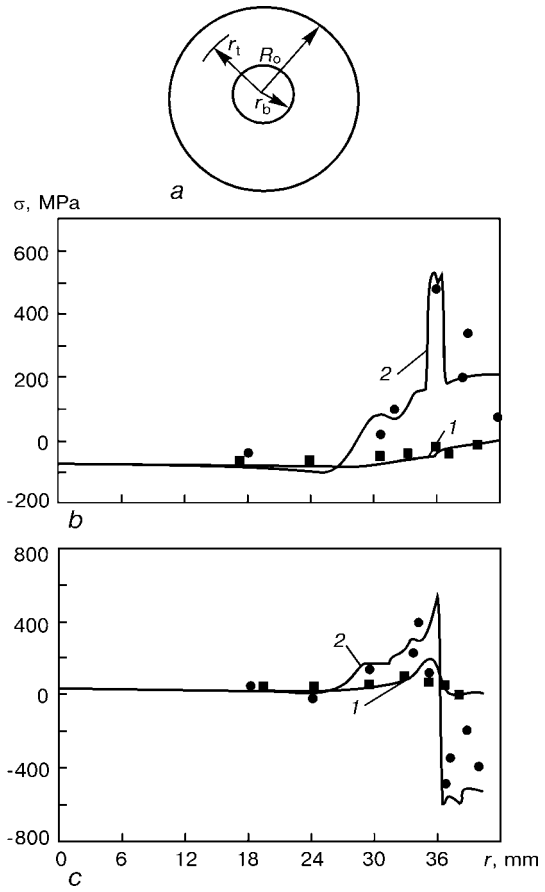

Figure 6. Diagram of the boring-turning process (*a*) and results of comparison of the calculated and experimental data for the radial σ^{d}_{rr} (*1*) and circumferential $\sigma^{d}_{\beta\beta}$ (*2*) stresses in discs of shafts for variants No.1 in layer *4* (*b*) and No.2 in layer *3* (*c*) at D = 72 mm

diameter. The main initial parameters for surfacing the above variants are given in Table 2. The values of the above material characteristics from Table 3, were used in calculation.

The data in Figure 2 and Table 4 show the change of the dimensions of the penetration zone and the appropriate changes in its composition through equivalent chromium Cr_{eq} and nickel Ni_{eq} by Schaeffler–DeLong dependencies [19]

$$Cr_{eq} = Cr + Mo + 1.5\ Si + 0.5\ Nb,\ \%,$$
$$Ni_{eq} = Ni + 30\ C + 0.5\ Mn,\ \%. \qquad (9)$$

These dependencies were the basis for evaluation of the final microstructure in the penetration zone, namely the amount of austenite v_a, martensite v_m and δ-ferrite $v_{\delta\text{-}f}$ (see Figure 3). In addition, $\kappa_W = Cr^W/Ni^W$ index was calculated, where Cr^W and Ni^W is the equivalent content of chromium and nickel, respectively, for WRC–1992 diagram [19], i.e.

$$Cr^W = Cr + Mo + 0.7\ Nb,$$
$$Ni^W = Ni + 35\ C + 20\ N + 0.25\ Cu. \qquad (10)$$

Level of κ_W characterises the hot cracking susceptibility of austenitic chromium-nickel alloy. A rather high resistance to these cracks is found at $1.47 < \kappa_W < 2.0$ [19].

From the data given in Table 4, it follows that for all the considered variants of surfacing with austenitic wire, rather favourable metallurgical conditions for hot cracking are in place in the first layer, as $\kappa_W < 1.47$. In deposition of the next layers κ_W value increases and is within the above-given interval, which corresponds to a high resistance to hot cracking.

An interlayer of metal deposited with flux-cored wire PP-AN163 with a higher content of chromium (variants No.3 and 5 from Table 4), also promotes an increase of κ_W index and of hot cracking resistance, respectively.

Figure 3 gives the calculated data of v_j distribution for microstructural components, depending on r coordinate for different characteristic sections. The latter are designated by the following numbers in Figures 3 – 5: *1, 2* — at the start of surfacing, *3, 4* — in the steady middle part. On the other hand, *1* and *3* correspond to section z = const along the middle of deposited bead, and *2* and *4* — between the adjacent beads. From the data given in Figure 3 one can see that the initial ferrite-pearlite structure of the shaft is preserved over its entire cross-section, except for a relatively small surface layer heated above T_*. At $T_* < T_{max} < T_{melt}$ microstructural changes proceed in the base metal of this layer, namely appearance of martensite and bainite (the latter is determined in the form of $v_b = 1 - v_a - v_m - v_{fp}$). In surfacing without preheating, the amount of martensite depends on heat input q_h. For variants with q_h = 650 cal/cm (see Table 2) a martensite layer ($v_m \approx 1$) of about 1 mm thickness forms at the beginning of the deposit. In the middle part of the surfaced shaft martensite content in the base metal is not higher than 0.65 – 0.55.

Martensite, however, appears in the deposited metal of the first layer even in the austenitic deposit (Figure 3, *a*), which is due to a greater dilution of the weld metal in the penetration zone.

At q_h = 2730 cal/cm (variants No.4 and 5 from Table 2), the amount of martensite in the base material is markedly reduced. At the start of surfacing $v_m < 0.55$, and in the middle part it is not more than 0.3. These higher values of q_h do not lead to a greater proportion of the base metal in the molten zone (with surfacing variants given in Table 2), because of the greater thickness of the deposited layer, so martensite is absent in the first layer. The second layer has the phase composition rather stable along the shaft length: $v_a = 0.95$, $v_{fp} = 0.05$.

Analysis of the microstructural state of the considered variants shows that a microstructure containing martensite in the range of $v_m = 0.35 - 0.65$ in the main part of the deposit and $v_m = 0.65 - 1.00$ at the start of the deposit, forms near the penetration zone from the base metal side. At certain levels of tensile stresses and hydrogen concentration, this can lead to cold (hydrogen) cracking in this zone. The given in Figures 4 and 5 distributions of normal stresses $\sigma_{\beta\beta}$ and σ_{zz} in sections *1 – 4* show that the surfacing zone

and the HAZ can develop quite significant circumferential $\sigma_{\beta\beta}$ and axial σ_{zz} normal components of the stress tensor (components σ_{rr} and σ_{zz} being comparatively small). In the case of a purely austenitic deposit (variants No.1 and 4 from Table 4), tensile stresses $\sigma_{\beta\beta}$ and σ_{zz} develop in the area of the penetration zone. It should be noted, however, that for variant No.1 in the stable part of the deposit after the first layer, $\sigma_{\beta\beta}$ and σ_{zz} stresses are compressive in the microstructure of this zone at the expense of the martensite component. After the fourth pass, however (Figures 4, *a* and 5, *a*), they become tensile. The above circumstance, in combination with the mentioned unfavourable factors (presence of martensite and hydrogen), can facilitate cold cracking and lower the fatigue resistance of the surfaced part, respectively.

In case of an underlayer of a martensitic material (variants No.3 and 5), during deposition of the first layer (underlayer) of a martensitic material (Figures 4, *b* and 5, *b*) $\sigma_{\beta\beta}$ and σ_{zz} stresses are compressive in the area of the fusion zone (beginning of the deposit, i.e. sections *1* and *2*, is an exception). In deposition of subsequent layers of austenitic metal (Figures 4, *c, d* and 5, *c, d*) the compressive nature of $\sigma_{\beta\beta}$ and σ_{zz} stresses in this zone does not change, which with other conditions being equal, should promote an improvement of the surfaced shaft fatigue resistance.

Considering the importance of the obtained information on residual stress distribution in shaft surfacing, experimental measurements were taken of residual stresses in the discs cut out of models of surfaced shafts (variants No.1 and 2 from Table 2). As shown above, Zaks method was applied, i.e. successive boring of the central hole of r_b radius in the disc (Figure 6, *a*), to determine residual stresses $\sigma^d_{rr}(r_b)$ by the average reading of three strain gauges on surface $r = R_o$. The measured elastic circumferential deformation $\varepsilon^e_{\beta\beta}(R_o)$ was used to find $\sigma_{rr}(r_b)$:

$$\sigma^d_{rr}(r_b) = -\frac{E\,\varepsilon^e_{\beta\beta}(R_o)}{2}\left(\frac{R_o^2}{r_b^2} - 1\right), \quad 0 < r_b < R_b. \qquad (11)$$

Boring was finished when r_b reached the values of $R_b \approx R_o/2$. This was followed by successive turning to a radius of r_t at $R_o > r_t > R_b$.

Strain gauges were also mounted on the surface $r = R_b$. In this case deformations $\varepsilon^e_{\beta\beta}(R_b)$ were measured.

Stresses $\sigma_{rr}(r_t)$ were calculated by $\varepsilon^e_{\beta\beta}(R_b)$ values, depending on r_t, from the following equation:

$$\sigma^d_{rr}(r_t) = \sigma^b_{rr}(R_b)\,\frac{R_b^2}{R_o^2(1 - R_b^2/R_o^2)}\left(\frac{R_o^2}{r_t^2} - 1\right) + \qquad (12)$$

$$+\,\frac{E\,\varepsilon^e_{\beta\beta}(R_b)}{2}\left(\frac{r_t^2}{R_o^2} - 1\right), \quad R_o > r > R_b,$$

where $\sigma^b_{rr}(R_b)$ are the stresses on surface $r = R_b$ developing during boring. Having determined relative residual stresses $\sigma^d_{rr}(r)$ from relationships (11), (12), let us find $\sigma^d_{\beta\beta}(r)$ stresses by numerical differentiation

$$\sigma^d_{\beta\beta}(r) = \frac{\partial}{\partial r}\left[r\,\sigma^b_{rr}(r)\right]. \qquad (13)$$

The results of processing the experimental data by expressions (11) – (13), in combination with the calculated data for variants No.1 and 2 (see Table 2) are given in Figure 6, *b, c*. As we can see, their agreement is quite good.

Considering that the described models of calculation of the thermal deformation processes have been verified more than once in various studies [15, 16, 20, etc.], as well as the agreement of the calculation and experimental data given in this paper, it can be quite confidently stated that the stressed state features determined above in deposition of an austenitic metal on a shaft of 35 type steel without an underlayer and with the considered underlayer, are valid.

CONCLUSIONS

1. Based on the modern approaches to a mathematical description of thermal deformation processes in corrosion-resistant surfacing along a small lead helix of parts of the type of shafts, it is possible, using computer means, to forecast the dimensions and shape of the penetration zone, its chemical composition and microstructure, and assess the risk of hot cracking. In a similar way it is possible to compute the base metal microstructure in the HAZ and the deformation kinetics, respectively, up to the residual state, assess the risk of cold cracking and, thus, search for more favourable variants in terms of provision of a high fatigue resistance of the surfaced shafts.

2. Numerical studies performed in this work demonstrate that in arc surfacing (without preheating) of shafts of 35 type steel with austenitic wire Sv-08Kh20N9S2BTYu, the required fatigue resistance values can be achieved if an underlayer deposited with PP-AN163 wire is used. This drastically reduces the risk of hot cracking at the expense of increase of κ_W index, and a favourable distribution of residual stresses is created in the potential zone of fatigue damage initiation.

REFERENCES

1. Frumin, I.I. (1961) *Automatic electric arc surfacing*. Kharkiv: Metallurgia.
2. Kravtsov, T.G., Stalnichenko, O.I., Olejnik, N.V. (1994) *Parts restoration by surfacing and assessment of their strength*. Kyiv: Vyshcha Shkola.
3. Makhnenko, V.I., Kravtsov, T.G. (1976) *Thermal processes in mechanised surfacing of parts of round cylinder type*. Kyiv: Naukova Dumka.
4. Vajnerman, A.E., Filimonov, G.N., Zakharov, V.F. *et al.* (1978) Fatigue and corrosion-fatigue strength of surfaced parts. *Fizika i Khimia Mekhaniki Materialov*, **2**, 80 – 84.
5. Taliat, B., Zacharia, T., Wang, X.-L. *et al.* (1998) Numerical analysis of residual stress distribution in tubes with spiral weld cladding. *Welding J.*, **8**, 328 – 335.

6. Murugan, N., Parmar, R.S. (1997) Effect of welding conditions on microstructure and properties of type 316L stainless steel submerged arc cladding. *Ibid.*, **4**, 210 – 220.
7. Seyffarth, P., Kassatkin, O. (1982) *Calculation of structural transformation in the welding process*. IIW Doc. IX–82.
8. Ueda, J., Murakawa, H., Luo Ju. (1995) A computation model of phase transformation for welding processes. *Transact. JWR*, **1**, 95 – 100.
9. Dilthey, U., Pavlyk, V. (2000) Recent advances in computer modelling of microstructure. In: *Proc. of 10th Int. Conf. on Computer Technology in Welding and Manufacturing*, Copenhagen, June 6 – 7 (to be publ.).
10. Makhnenko, V.I., Velikoivanenko, E.A., Rozynka, G.F. *et al.* (1999) Selection of rational dimensions of welded component mock-ups in development of welding technology. *Avtomaticheskaya Svarka*, **7**, 3 – 14.
11. Makhnenko, V.I., Velikoivanenko, E.A., Rozynka, G.F. *et al.* (1999) Computer modelling of welding processes as a tool for predicting defects in welded joints. *Ibid.*, **12**, 10 – 19.
12. Seyffarth, P., Meyer, B., Scharff, A. (1992) *Groβer Atlas Schweiβ-ZTU-Schaubilder*. Düsseldorf.
13. (1991) *Atlas of time-temperature diagrams for irons and steels*. Ed. by G.F. Vander Voort. ASM Publ.
14. Beres, L. (1998) Proposed modification to Schaeffler diagram for chrome equivalents and carbon for more accurate prediction of martensite content. *Welding J.*, **6**, 273 – 276.
15. Makhnenko, V.I. (1976) *Computational methods of investigation of the kinetics of welding stresses and strains*. Kyiv: Naukova Dumka.
16. Makhnenko, V.I., Velikoivanenko, E.A., Pochinok, V.E. *et al.* (1999) Numerical methods of the predictions of welding stresses and distortions. *Welding and Surfacing Rev.*, part 1, 1 – 150.
17. Yuriev, S.F. (1950) *Specific volumes of phases in martensitic transformation of austenite*. Moscow: Metallurgizdat.
18. Benau, F.A., Dogdanov, A.M. (1955) Investigation of residual stresses in surfaced ship shafts. *Rechnoj Transport*, **2**, 3 – 7.
19. (1998) *Welding handbook*. Part 2. Miami: AWS.
20. Medovar, B.I., Shevtsov, V.L., Mariinsky, G.S. *et al.* (1978) *Thermal processes in electroslag remelting*. Kyiv: Naukova Dumka.

ABOUT THE PROBLEM OF CONSTRUCTION OF A DYNAMIC MODEL OF WELD POOL IN ELECTRIC ARC WELDING

G.I. LESKOV and **S.V. PUSTOVOJT**
The E.O. Paton Electric Welding Institute, NASU, Kyiv, Ukraine

ABSTRACT

Theoretical and experimental investigations of weld pool in comparison with an existing quasi-static model are analyzed. Contradictions and drawbacks, typical of this model, are outlined. The more perfect dynamic model was constructed and described on the basis of available data, laws of motion of liquids and gases and equations of electrodynamics.

Key words: *arc welding, weld pool, electromagnetic and aerodynamic forces*

The weld pool is an important intermediate product of the welding process. Its sizes, position in space, time of existence, and also motion as a whole object and liquid inside of it, and processes of crystallization determine the quality of welds, efficiency of welding and energy consumption. Experimental and theoretical investigations of factors characterizing the processes in the pool and their effect on the weld quality dated back to the time of invention of welding and continue to the present day. Over this period hundreds of works devoted to the mentioned investigations were published. They can be divided in two groups as those:

- describing metallurgical processes in the pool and its crystallization, which define mainly the weld metal quality;
- devoting to study of phenomena which influence the geometry, first of all, the pool depth h and, respectively, the welding productivity:

$$S = hv_{\text{w}}, \qquad (1)$$

where S is the area of edges welded per time unity; v_{w} is the rate of pool displacement along the workpiece.

The investigations of the first group have resulted in the development of high-quality welding consumables, such as solid and flux-cored wires, fluxes and electrode coatings, shielding gases and also definition of conditions of their application. In addition, in most cases the welds were produced with properties similar to those of the parent metal. These investigations are summarized in manuscripts [1 – 4].

Among three geometric characteristics of the pool (length, width and depth), the first two characteristics are studied comprehensively [5, 6].

There are not yet convincing ideas about physical phenomena which determine the pool depth h, associated with a depth of crater h_{c} and thickness of a liquid layer δ_{l} under it ($h = h_{\text{c}} + \delta_{\text{l}}$). The accumulated experimental data and hypotheses put forward are generalized in most cases in the form of a quasi-static model of the pool. In case of the flat immersed arc welding this model is illustrated in Figure 1.

This model is based on a conception about the axial symmetry of forces and pressure acting on the pool, when an arc spot is located on the crater bottom [1, 2, 7, 8]. The steady state of this pool is determined by the equality

$$p_{\text{a}} = p_{\text{m}}, \qquad (2)$$

where p_{a} is the arc pressure; $p_{\text{m}} = \rho g(h = h_{\text{p}})$ is the metallostatic pressure of the liquid metal.

Electromagnetic forces which cause the pressure p_{a} at axisymmetric spreading of arc current in the pool are considered in this model most completely [8, 9].

The processes of melting the front wall of the crater and forces which cause the motion of liquid metal along it to the zone of the highest arc pressure p_{a}, have not yet analyzed on the basis of laws of hydrodynamics and distribution of the arc power. It is considered that melting of this wall is occurred by a radiation of the arc column, and the energy of the highest concentration evolving in the arc spot on the crater bottom does not cause the further deepening of the latter. This paradox remains to be explained by the presence of a layer of δ_{l} thick liquid metal with a low heat conductivity. However, it is known that the rate of melting of the wire electrode above its active spot does not depend on the thickness of the

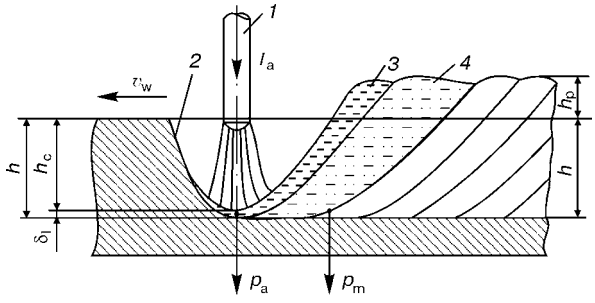

Figure 1. Scheme of a quasi-static model of pool in electric arc welding: *1* — electrode; *2* — front wall of the weld pool; *3* — liquid layer of metal; *4* — crystallizing layer

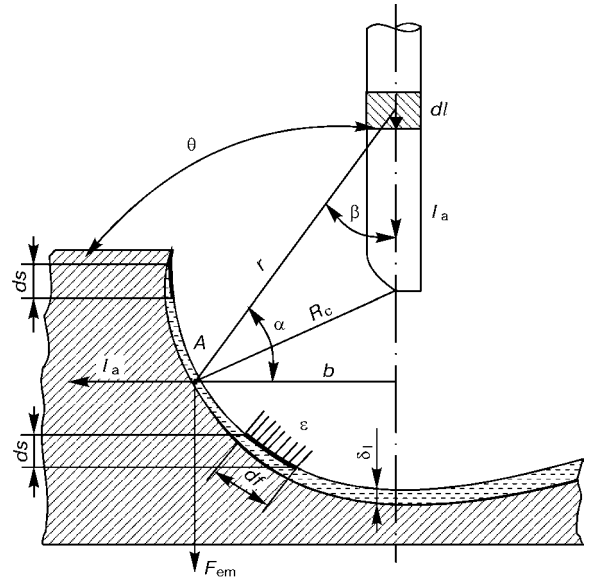

Figure 2. Crossing of the crater front wall with a plane of the pool symmetry (designations are the same as in Figure 1)

liquid layer [10]. The axial symmetry of pressure has to cause the movement of the liquid metal in all directions, including upward the front wall of the crater, that contradicts the experience. The above-mentioned drawbacks and contradictions of a quasi-static axisymmetric model of the weld pool require the more thorough analysis of its stability in the form being considered.

The distribution of arc power in the crater during immersed arc welding can be evaluated from the shape of its front wall. Crossing of the latter by a symmetry plane, being formed by the axis of the moving electrode, represents a curve with approximately similar radius of curvature R_c [11], having a center at the wire electrode edge (Figure 2).

At a steady condition the surface of the front wall is moved, preserving its shape, in the direction of welding with the speed v_w. Consequently, each its element of ds section (Figure 2) in the same direction receives, on average, the same power from the arc $dq = \varepsilon_{av} df = \text{const}$, where ε_{av} is the mean concentration of the latter at the edge of element of df area. As the arc wanders continuously along the surface being melted with an average period τ, staying at each its element during time Δt, then

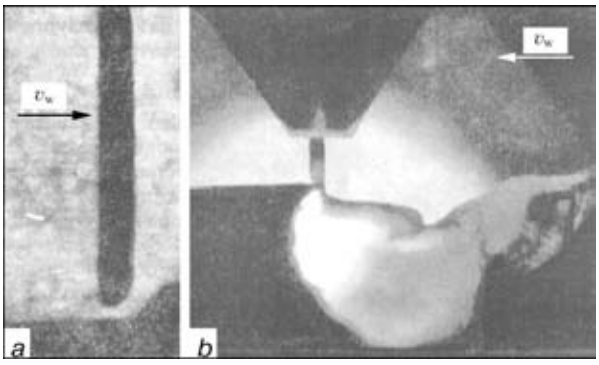

Figure 3. X-ray photograph of arc under flux (*a*) and photograph of open arc (*b*), (×5), time of exposure is 10 μs (reduced by 3/4)

$$\varepsilon_{av} = \varepsilon_s \frac{\Delta t}{\tau}, \tag{3}$$

where ε_s is the mean concentration of power in a heat spot.

Consequently,

$$\varepsilon_s \frac{\Delta t}{\tau} df = dq.$$

As all the elements of ds area are subjected to the action of arc with similar characteristics (dq, τ, ε_s) and $df = ds/\sin\alpha$, we obtain

$$\Delta t = \frac{\tau dq}{\varepsilon_s ds} \sin\alpha = k \sin\alpha. \tag{4}$$

It follows from expression (4) and Figure 2 that the wandering heat spot does not practically enter the lowermost element of the front wall of the crater where α and $\sin\alpha$ are close to zero, and stays for the most time at above-located its elements for which $\sin\alpha > 0$. This conclusion is confirmed by X-ray photographs of the arc under the flux [12] and also by colored photographs [13] of arc between the wire electrode and 5 mm thick plate edge, which is clamped between the quartz glasses (Figure 3). Each of them has a recorded position of the column which is not axial to the electrode but shifted to the side of the crater front wall. The wire electrodes are melted from the side of this wall and the column plasma is also directed to it (Figure 3, *b*). The wavy shape of the liquid metal at the surface of the above-mentioned wall of a maximum thickness (about 1 mm) and a length of wave, equal to 3 mm, is worthy of notice. Experimental data [14] about the current distribution in the pool confirmed the wandering of the arc spot and heat spot, associated with it, at the crater front wall mainly. Using a magnetic belt of Rogovsky, passed through the hole in plates being welded ahead of the arc at the distance of the weld width, it was established that up to 70 % of current is passed in this direction near the crater not depending on the position of the current connector.

The absence of axial symmetry in distribution of arc current in the pool requires the new approach to the evaluating of forces and pressures of an electromagnetic origin which act on its elements depending on the position of the electrode, i.e. vertical, forward or backward.

The simplified electromagnetic scheme of a welding circuit with a vertical electrode corresponds to that shown in Figure 2. In addition, the current circuit in the zone of welding contains two deformable elements: arc column and interlayer of liquid metal of δ_l thickness. The electromagnetic force F_{em}, acting on this element in a steady condition at $I_a = \text{const}$, is determined by expression [15]

$$F_{em} = \frac{I^2}{2} \frac{dL}{d\gamma}. \tag{5}$$

It stipulates the deformation $d\gamma$ of the circuit in the direction of a growth of its inductance L. This is feasible when the circuit sizes are increased, i.e. in shifting of point A (see Figure 2) downwards. Due to a complex calculation of derivative $dL/d\gamma$ it is difficult to determine F_{em} using equation (5). However, it is possible to estimate the order of value F_{em}, acting on interlayer of liquid of thickness δ_l with current I_a in the active spot with a point A center, using the laws of Ampere and Biot–Savart:

$$F_{em} = I_a \delta_l B \sin (I_a, B), \quad (6)$$

$$dH = \frac{I_a}{4\pi r^3}[\vec{dl} \cdot \vec{r}] = \frac{I_a dl}{4\pi r^3} \sin \beta. \quad (7)$$

By integrating expression (7), we obtain the intensity in point A when it is a center of the active spot

$$H = \frac{I_a}{4\pi b} (\sin \frac{\pi}{2} - \sin \alpha).$$

At $b = 3 \cdot 10^{-3}$ m, $\delta_l = 10^{-3}$ m, $I_a = 500$ A, $\sin \alpha = \pi/4$ $F_{em} = 2.5 \cdot 10^{-2}$ N.

In the transverse section of the interlayer of 10^{-5} m^2 area, normal to F_{em}, the pressure on it will be $p_m = 2500$ Pa. It exceeds significantly the metallostatic pressure p_m (Figure 1) in a tail part of the pool, which is equal to 750 Pa at $h + h_p = 10^{-2}$ m. The latter means that force F_{em} acting on the liquid metal interlayer at the crater front wall is sufficient to accelerate this interlayer, to overcome the viscous forces during its downward movement and metallostatic pressure in the pool tail part.

Charges moving in the arc column adjacent to point A are subjected to the action of the Lorentz force

$$F_L = ev_e B, \quad (8)$$

which shifts them from this point to the electrode axis, and also to the electrostatic force

$$F_e = eE, \quad (9)$$

which directs charges along the column axis. The average rate of a directed movement of electrons v_e in the column can be estimated from the current density in it $j = env_e$, at concentration of electrons $n = 7.29 \cdot 10^{22} \gamma \frac{p}{T}$ [16], where $\gamma = 3 \cdot 10^{-2}$ is the degree of gas ionizing in welding arcs.

At $p = 10^5$ Pa, $T = 6 \cdot 10^3$ K and $j = 2 \cdot 10^7$ A/m^2 the rate of movement of electrons is $v_e = 3.5 \cdot 10^3$ m/s, and $F_L = 3.5 \cdot 10^{-17}$ N. At the field intensity in column $E = 3 \cdot 10^3$ V/m, the electrostatic force $F_e = 4.8 \cdot 10^{-16}$ N that is by one order higher than the Lorentz force. Therefore, the column is maintained in the direction of the electrical field, i.e. in the zone of a minimum distance between electrodes. Its pressure p_a against the front wall of the crater meets known laws [8] and causes deformation and movement of elements of the liquid interlayer on it in accordance with a basic law of movement of an ideal liquid [17]

$$\rho \frac{dv}{dt} = -\frac{dp}{dr}. \quad (10)$$

As the pressure is maximum at the column axis and decreases in radius, then the liquid metal is spread to all the sides without acceleration, being directed to the crater bottom and to the pool tail part. The wandering zone of the maximum pressure promotes the formation of waves only in the pool head part, which are spreading with some damping all over its volume.

The electromagnetic force F_{em}, causing the directed movement of liquid in accordance with equations (6) and (7), depends on the position of a wire electrode with current I_a as the field intensity at the crater front wall depends in its turn on the latter. In backward welding at $\theta < 90°$ (see Figure 2) all the elements dl of the electrode approach the wall, thus causing the growth in the field intensity near its surface and, consequently, the electromagnetic force. The highest effect is observed at $\theta = 0°$, i.e. at a fire-cracker welding [18], when the drift of liquid metal ahead of arc under the action of F_{em} and the penetration depth are maximum. In forward welding ($\theta > 90°$) the values H and F_{em} are decreased, thus weakening the liquid metal spreading and the pool depth is decreased. This conclusion is confirmed by numerous experiments in submerged arc welding [1].

Analysis of experimental data about the shape of the weld pool, current distribution in it, effect of inclination of wire electrode for a depth of penetration, as well as drawbacks of a quasi-static model of the pool makes it possible to construct the more perfect its dynamic model, whose general view is presented in Figure 4. The arc heat spot wanders continuously over the front wall of the crater and, in accordance with a «principle of minimum» is arranged in the zones, mostly adjacent to the wire electrode. All the elements of this wall are melted with an average rate equal to the welding speed. The layer of the liquid metal is deformed, i.e short-time small depressions appear in different zones of the front wall. Forces which cause these deformations do not influence the liquid movement on the crater bottom and in the pool tail part. The latter was stipulated by action of the Ampere force occurring in a liquid layer with current I_a located in a current magnetic field of the wire electrode. In accordance with the «left-hand rule» this force is always directed to the crater bottom.

The flow of the conical arc plasma, being deformed in the crater [8], creates a high-speed pressure to all the elements of its surface, including the bottom part.

Flows of liquid and gas, occurring under the action of the above-mentioned forces, flow round the penetrated non-deformed surface and contact it under the action of forces of a molecular interaction and a high-speed pressure.

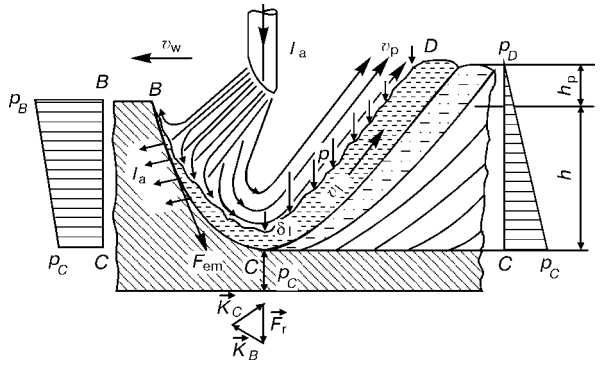

Figure 4. Scheme of a dynamic model of the weld pool

Following the conditions of stability, the welding pool should be analyzed in two its parts: top part — in the section between points B and C (Figure 4) and tail part — between points C and D. The rate of liquid movement v_l in point C is proportional to the welding speed v_w [19], the coefficient of proportionality k is increasing with the current rise. At v_w = = 10 m/h, I_a = 500 and 1000 A and, respectively, k = 1.5 and 2.3, thickness of a layer of the moving liquid is within the narrow ranges — δ_l = 1.25 – 1.50 mm [19] in downward and upward welding. Therefore, the effect of this factor on the change in penetration depth both in the given welding conditions and in change of angle of electrode inclination forwards and backwards [1] does not correspond to the conceptions of a quasi-static model of the pool. Dependence of v_l on v_w and I_a indicates the difference in trajectories of the liquid movement (along the curvilinear surface of the crater) and welding head (along the straight line). The conditions of stability of the pool tail part between the points C and D taking into account value δ_l in the point C can be evaluated using Bernoulli's theorem for the stationary flowing of a perfect incompressible liquid [20]

$$p + \rho g h + \rho \frac{v^2}{2} = \text{const}, \qquad (11)$$

where p is the static pressure, $\rho\frac{v^2}{2}$ is the dynamic pressure, $\rho g h$ is the increment of pressure at change of height h.

When h is calculated from point C with a maximum depth of penetration under the crater bottom for the points of the tail part, located between the points C and D, where $v_C = v_l$, and $v_D = 0$, we shall obtain

$$p_{atm} + p_C + \rho\frac{v_l^2}{2} = p_{atm} + \rho g(h + h_p). \qquad (12)$$

Here, p_{atm} is the pressure of atmosphere, similar to all the pool sections.

For the pool equilibrium in point C the pressure should be

$$p_C = \rho g(h + h_p) - \rho\frac{v_l^2}{2}. \qquad (13)$$

At v_l = 2.5 $v_w\rho\frac{v_l^2}{2} << \rho g(h + h_p)$ and v_w = = 36 m/h = 10^{-2} m/s, and the pressure p_C at the crater bottom should be equal to the metallostatic pressure of the pool. In point D the pressure p_D = 0. The diagram of pressures on the elements of the pool tail part is given in Figure 4 on the right. In addition, vector $-\frac{dp}{dh}$ is directed upwards that satisfies the law of liquid movement in this part.

At the front wall the liquid movement from point B to point C is possible if the derivative $\frac{dp}{dh}$ in this section of its path is also negative. The pressure diagram at this wall is given in Figure 4 on the left. Growth of p on it as compared with p_C is due to the pressure of the arc [8], whose active spot wanders round all the points located between B and C. Pressure p_C to the crater bottom, where the location of the active spot in accordance with equation (4) is low-probable, is reactive, occurring in changing of plasma flow direction, and, respectively, its amount of movement K in this zone. The force, acting to the crater bottom [17] will be

$$\vec{F}_r = \vec{K}_C - \vec{K}_B . \qquad (14)$$

Vectors of these values at $K_B = K_C$ and change in their direction at the crater base for $\pi/2$ are shown in Figure 4. For the plasma jet of S_p section, flowing round the crater bottom with a rate v_p

$$K = \rho_p S_p v_p^2. \qquad (15)$$

The density ρ_p of plasma with μ = 14 [16], average temperature $T = 5\cdot10^3$ K at atmospheric pressure p = = 10^5 Pa is equal to $3.4\cdot10^{-2}$ kg/m^3.

Assuming the shape of the jet section to be round with a 3 mm radius, close to the radius of curvature of weld roots and with a depth of about 1 cm, and its rate v_p = 330 m/s and taking into account the data [21, 22], we shall obtain

$$F_r = \sqrt{2}\ \rho_p S_p v_p^2 = 9.6\cdot10^{-2}\ \text{N}.$$

This force is acting in vertical direction (see Figure 4), thus providing pressure p = 960 Pa to the lower part of the crater of 10^{-4} m^2 area. This pressure is sufficient for equalizing the maximum metallostatic pressure of the liquid steel of density ρ_l = = $7.5\cdot10^3$ kg/m^3 in the pool tail part at the penetration depth h = 1 cm, h_p = 0.2 cm, when $p_l g(h + h_p)$ = = 900 Pa.

As the reactive pressure of the plasma to crater bottom in accordance with equations (14) and (15) depends on the square of its rate, then it is closely connected with the current density in the wire electrode. The higher the latter, the higher the angle at the arc column apex [23], rate of plasma in the cone and generated pressure. The pool equilibrium becomes

feasible at a large depth of penetration that is well correlated with experimental data [1].

CONCLUSIONS

1. The known quasi-static axisymmetric model of the pool is not correlated with the main law of liquid or gas motion, experimental data about the processes of melting, metal transfer in pool and formation of welds. However, the electromagnetic forces, described within the scope of this models and forming the plasma flows in the arc column and liquid metal in the active spot zone are also lawful in its dynamic model, if to consider the zone of their action not to be the crater base but its front wall.

2. It is shown in the model suggested that during immersed arc welding the axis of arc column coincides sometimes with the axis of the wire electrode. The active spot at the workpiece welded together with a surrounding heat spot is wandering along the crater front wall. Here, the rate of melting of all its elements is equal to the welding speed.

3. The mentioned wall can be presented in the form of a part of the sphere with a center at the wire electrode end.

4. The arc column direction is determined by the electrical field between the electrodes, whose action on the motion of electrons is by one order higher than that of the magnetic field.

5. The liquid metal from the front wall of the crater to the zone of a higher pressure at the crater bottom is transferred by the Ampere's force occurring in the magnetic field of the arc current both in the electrode stickout and in the nozzle. This force increases with the increase in the arc current and decrease in the angle of electrode inclination to the workpiece during the backward welding.

6. The crater depth and penetration of the metal welded is determined, first of all, by the reactive pressure to the plasma jet, which is proportional to its density and square of the rate. As it grows with increase in the column conicity, depending on the wire electrode diameter, then the increase in the penetration depth is reached at maximum density of current in it.

REFERENCES

1. (1948) *Submerged arc welding*. Ed. by E.O. Paton. Kyiv-Moscow: Mashgiz.
2. (1974) *Technology of electric welding of metals and alloys by fusion*. Ed. by B.E. Paton. Moscow: Mashgiz.
3. (1978) *Welding in machine-building*. Handbook. Ed. by I.A. Olshansky. Moscow: Mashgiz.
4. (1990) *Metallurgy of arc welding*. Ed. by I.K. Pokhodnya. Kyiv: Naukova Dumka.
5. Rykalin, N.N. (1951) *Calculation of heat processes in welding*. Moscow: Mashgiz.
6. (1960) *Processes of parent metal melting in welding*. Moscow: AN SSSR.
7. (1979) *Metal transfer and mass flow in the weld pool*. IIW Doc. 212-461–79.
8. Lebedev, V.K., Pentegov, I.V. (1981) Force action of the welding arc. *Avtomaticheskaya Svarka*, **1**, 7 – 15.
9. Pentegov, I.V. (1987) Force action of arc (non-channel model). *Ibid.*, **1**, 23 – 27.
10. Pokhodnya, I.K. (1964) Method of investigation of process of melting and transfer of electrode metal in welding. *Ibid.*, **2**, 5 – 7.
11. Razmyshlyaev, A.D., Leshchinsky, L.K., Nesterenko, K.A. (1975) Distribution of thickness of liquid metal layer over the length of weld pool crater. *Ibid.*, **12**, 62 – 63.
12. Ostapenko, N.G., Medovar, B.I. (1947) X-ray examination of arc burning under the flux. *Avtogennoye Delo*, **11**, 9 – 12.
13. Zemlevsky, L.A., Leskov, G.I. (1978) Investigation of process of metal melting in immersed arc welding. *Avtomaticheskaya Svarka*, **3**, 16 – 17.
14. Rajchuk, Yu.I. (1967) Current distribution in plate during arc welding. *Ibid.*, **4**, 19 – 22.
15. Nejman, L.R., Demirchyan, K.S. (1975) *Theoretical bases of electrical engineering*. Leningrad: Energia.
16. Leskov, G.I. (1970) *Electric welding arc*. Moscow: Mashgiz.
17. Strelkov, S.P. (1956) *Mechanics*. Moscow: GITTL.
18. Makara, A.M. (1948) Process of parent metal melting in submerged arc welding. In: *Transact. on Electric Welding*. Kyiv: PWI.
19. Razmyshlyaev, A.D. (1979) Investigation of rate of molten metal motion in weld pool in submerged arc surfacing. *Svarochnoye Proizvodstvo*, **9**, 3 – 5.
20. Lojtsyansky, L.G. (1973) *Mechanics of fluid and gas*. Moscow: Nauka.
21. Kulagin, I.D., Nikolaev, A.V. (1958) Heat balance of DC welding arc in gases in the period of drop formation. *Izv. AN SSSR, Divis. of Eng. Sci.*, **11**, 89 – 91.
22. Finkelburg, V., Mekker, G. (1961) *Electrical arcs and thermal plasma*. Moscow: Izd. Inostr. Literatury.
23. Pustovojt, S.V., Leskov, G.I. (2000) Improvement of arc welding using electromagnetic methods. *Avtomaticheskaya Svarka*, **1**, 39 – 42.

NEW HIGH-RESISTANT DISPERSION-STRENGTHENED COPPER MATERIALS FOR RESISTANCE WELDING ELECTRODES

P.A. VITYAZ[1], **F.G. LOVSHENKO**[1] and **G.F. LOVSHENKO**[2]
[1]Academy of Sciences, Minsk, Belarus
[2]Mechanical Engineering Institute, Mogilyov, Belarus

ABSTRACT

Method of selection of initial elements and prediction of phase composition of the dispersion-strengthened copper is described. Technology of manufacture of the material using the method of a mechanical alloying is optimized. Phase composition, structure and properties of the produced material are examined and optimum conditions of the resistance welding with electrodes made from this material are established. It is shown that the application of the dispersion-strengthened copper provides increase in life of products by 2 – 3 times.

Key words: *mechanical alloying, dispersion-strengthened materials, transformations, composition, structure, properties, resistance welding electrodes, life*

Implementation of high-efficiency robots and automatic machines in the welding industry, and also a competitiveness of products manufactured by the resistance welding is limited mainly by a low life of electrodes. Materials, used for their manufacture, should possess a complex of physical and mechanical properties, mutually excluding each other, coming from the concepts of a classic materials science. Thus, in parallel with a heat resistance, they should have high values of electrical and heat conductivity, the electroerosion and high-temperature corrosion resistance. The use of cast dispersion-hardened bronzes as materials for the resistance welding electrodes exhausted its possibilities by now. This is due to the fact that chromium, zerium, beryllium, included into the composition of bronzes, have a limited solubility in copper.

In addition, in case of a minimum value of a relative electric conductivity, approximately equal to 75 %, which is admissible for materials of this purpose, the attained complex of mechanical properties is typical of the following characteristics: hardness is $\leq HB$ 170, tensile strength at 20 °C is $\sigma_t \leq 600$ MPa, 100-hour strength at 500 °C is $\sigma_{100}^{500} \leq 150$ MPa, temperature of recrystallization is $T_r \leq 500$ °C. The increase in hardness to HB 210 and tensile strength to 750 MPa, typical of complexly-alloyed alloys with a high content of alloying elements, is accompanied by the reduction in relative electric conductivity to 50 % and does not lead to a great increase in mechanical characteristics of heat resistance and temperature of recrystallization. The lack of cast electrode materials with an optimum complex of physical and mechanical properties becomes a brake on the way of implementation of high-efficiency technological processes of the resistance welding and improvement of the quality of products manufactured by welding.

The problem can be solved by the use of new methods of manufacture of materials and methods of their strengthening. In several works [1 – 6] the life of the resistance welding electrodes is increased by deposition of a coating on the electrode working surface, thus excluding its interaction with a material welded. Thus, a resistance welding electrode is offered [1], whose working part is coated with a tungsten disulfide precipitated from a vapour phase. An electrode [2] coated with a layer of nitride of titanium or molybdenum of ≤1 μm thickness, deposited by an ion implantation is also offered.

Several methods of improvement of life of the materials have been suggested [7 – 10] by the reinforcement with high-strength, heat-resistant, inert inclusions. Thus, the electrode was manufactured [7], consisting of a metal casing and a working insert. The latter contains elements of an increased hardness and elements of an increased electric conductivity. The diamond grains can be used as the first elements, which are put into a sheath of silicon carbide using a binder of cobalt or nickel silicides. Technology of producing the electrode material [8] whose life is increased due to use of a powdered chromium bronze, reinforced with a spiral made from a Cu-plated tungsten wire, is presented.

As is seen from the above-given examples, the suggested methods are expensive in many cases, being «exotic» and hardly-realized in the industrial scale. The progress in this field is connected mainly with a powdered metallurgy.

Technology of producing dispersion-strengthened composite materials (DSCM) of copper presents a great interest. Their structure represents a matrix of metal or alloy, in which the dispersed particles of the strengthening phase are distributed uniformly. As a latter, the thermodynamically-stable compounds (oxides, carbides, nitrides, intermetallics) with a high

value of a shear modulus are used. Taking into account the physical and mechanical properties, lower prices and ecological safety, oxides of aluminium and magnesium are most suitable for this purpose.The limiting strengthening can be expected in materials with a maximum developed surface of grains and subgrains, fixed and stabilized by dispersed particles of the strengthening phase. Coming from the analysis of theories of a dispersed strengthening [11 – 13], a structure of a microcrystalline type with < 1 μm size of grains seems to be optimum. Particles of the strengthening phase should have the size of < 0.1 μm, and their total volume of < 10 %. The dispersion strengthening has remarkable advantages as compared to other types within the range of 0.60 – 0.95 T_m of the base. The presence of chemically-stable inclusions of the strengthening phase in the volume share of < 10 % does not greatly influence the electric and thermal conductivity, and also corrosion resistance of the material.

The known methods of producing DSCM, which found the industrial application, are as follows: chemical mixing, decomposition of mixture of salts, hydrogen recovery in solutions, chemical precipitation from solutions, inner oxidizing, mechanical alloying [14 – 16]. Technology of producing materials based on all the listed methods, excluding the last method, is expensive and could not realize all the advantages of the dispersed strengthening. Chemical methods are also not safe ecologically. In this connection, the process based on a reactive mechanical alloying, supposing the interaction between components and formation of strengthening phases at the stage of treatment of a powdered composition in a mechanical reactor and at a subsequent thermal action of the produced granulated composition [17 – 19], whose realization creates premises for the formation of the material with optimum parameters of the structure and properties, presents a great interest.

The present work was aimed at the development of new high-resistant DSCM for the resistance welding electrodes. To achieve the aim, it was necessary to develop the method of selection of initial components and prediction of the phase composition of the materials, to determine the most promising compositions, to study their physical and mechanical properties and to set the optimum parameters of service of the products manufactured from them.

Methodology of research, materials and equipment. Technological process of manufacture of mechanically-alloyed materials includes the following stages: designing of initial composition of the charge, treatment of the charge in a mechanical reactor and producing DSCM, cold pressing of briquettes, their annealing and hot extrusion of semi-finished products.

The procedure suggested for modelling of the phase composition of materials is based on a thermodynamic analysis of equilibrium processes whose proceeding in this system is expected. In addition, it is based on the statement that when the conditions of the mechanical alloying realized in practice and characterized by relatively low energy intensity are used, then only those transformation will have a remarkable progress in diluted heterophase systems which are directed to the decrease in Gibb's energy. In addition, the long high-temperature action to which the mechanically-alloyed compositions are subjected in processing to the semi-finished products, will lead to the formation of the material with a phase composition which is close to equilibrium composition. In this case the components capable to interact in solid state between each other or with a base to form phases possessing high values of a shear modulus and thermodynamic stability, coming from the thermodynamics of equilibrium processes, should be used as alloying elements. To synthesize aluminium , which strengthens copper effectively [19], the initial charge should contain aluminium from the one side and oxygen from the other side, as alloying elements, thus forming a compound with a relatively low thermodynamic stability. To create simple and reproducible technology of a reactive mechanical alloying, the latter should be in liquid or solid state under the normal conditions. Interest is attracted, first of all, by oxides of elements having larger values of Gibb's energy of formation than Al_2O_3. Taking into account that element (E) which is recovered during proceeding of the redox reaction

$$2n\mathrm{Al} + 3\mathrm{E}_m\mathrm{O}_n = n\mathrm{Al}_2\mathrm{O}_3 + 3m\mathrm{E}$$

from the alloyed oxide (E_mO_n), should not influence negatively on the physical and mechanical properties of the material designed, the range of substances used for this purpose is limited. It can include the oxides of elements having a negligible solubility in copper that is an obligatory condition of producing material with electric conductivity close to that of the base. Except the copper oxides, the oxides of the refractory elements (Mo, W, Nb, V, Cr, Zr) and also nitrogen oxides are worthy of attention. During recovery from oxides the refractory metals are capable to play a role of strengthening phases. The aluminium nitride (AlN), whose formation is thermodynamically probable in the composition alloyed with nitrogen oxides, also meets the requirements specified to them.

The aluminium content in base compositions was 0.8 %. Concentration of oxygen introduced with an alloying oxide was 0.71 % (from stoichiometric ratio of aluminium to oxygen). According to the calculations this privides a formation of Al_2O_3 in amount of ≈ 1.5 wt.% or ≈ 4.0 vol.%. As alloying oxides, NO_2, CuO, MoO_3, V_2O_5, NbO, Cr_2O_3, ZrO_2 are used whose Gibb's energy of formation ΔG_T^o is varied within a wide range from +81.6 oxygen atoms in NO_2 to up to –547 kJ/mole of oxygen atoms in ZrO_2 that makes it possible to define the role of a thermodynamic factor in proceeding phase transformations in the systems.

The thermodynamic calculation is reduced to the search of compounds which can be formed from ele-

Table 1. Compound composition, main reaction and strengthening phase

Compound composition	*Main reaction*
Cu – 2/3 Al – N_2O	2/3 Al + N_2O = 1/3 Al_2O_3 + N_2
Cu – 2/3 Al – CuO	2/3 Al + CuO = 1/3 Al_2O_3 + Cu
Cu – 2/3 Al – 1/3 MoO_3	2/3 Al + 1/3 MoO_3 = 1/3 Al_2O_3 + 1/3 Mo
Cu – 2/3 Al – 1/5 V_2O_5	2/3 Al + 1/5 V_2O_5 = 1/3 Al_2O_3 + 2/5 V
Cu – 2/3 Al – NbO	2/3 Al + 1/3 NbO = 1/3 Al_2O_3 + Nb
Cu – 2/3 Al – 1/3 Cr_2O_3	2/3 Al + 1/3 Cr_2O_3 = 1/3 Al_2O_3 + 2/3 Cr
Cu – 2/3 Al – 1/2 ZrO_2	1/3 Cu + 2/3 Al = 1/3 $CuAl_2$

ments included into the composition of initial substances and determination of their quantitative ratio. Elementary state of the system corresponds to the zero value of ΔG_T^o. Change in ΔG_T^o during reactions was calculated using the method of absolute entropies in its most precise third approximation [20].

To produce materials, the powders of copper PMS-1, aluminium PA4 and oxides of grade «Ch» were used. Optimizing of the process of producing materials and conditions of welding with electrodes manufactured from them was made in two stages. At the first stage the method of a single-factor planning was used, while at the second stage — the method of Box–Wilson. Parameters of optimizing were as follows: hardness, tensile strength, electric impedance of materials and life of electrodes.

Conditions of treatment in a mechanical reactor, a vibrating mill of a giratory type, were changed within the following ranges: amplitude of oscillation of a working chamber r = 3 – 7 mm; frequency of oscillations ω = 10 – 35 s^{-1}; normal acceleration of balls a = 50 – 180 $m \cdot s^{-2}$; degree of filling of the working chamber with balls ε = 30 – 90 %; ratio of volumes occupied with balls and charge k = 3 – 10; temperature of the process T = 20 – 140 °C; diameter of balls, d = 11.15 mm; duration of treatment τ = 2 – 12 h. Briquetting to 70 – 75 % was made by a cold pressing. The semi-finished products were produced by hot extrusion. The rate of material flow was 0.12 – 0.17 $m \cdot s^{-1}$. Coefficient of drawing was 5 – 20. Temperature of briquette heating was 650 – 850 °C, temperature of heating of a press tool was varied within 500 – 700 °C. Technological factors in welding, such as compression force of electrodes F, welding current I, time of welding current passing τ_w and welding time n, were varied within the following ranges: F = = 2 – 4 kN, I = 9 – 13 kA, τ_w = 0.1 – 0.3 s, n = 10 – 70 min^{-1}. Structure and properties were studied using standard techniques and equipment.

Results of investigation and discussion. According to the thermodynamic analysis the main reaction in most of investigated systems in the temperature range of 298 – 1356 K is the aluminium interaction with alloying oxide with a formation of Al_2O_3 and the recovered element (Table 1).

As a result of proceeding of the redox reaction with participation of N_2O, CuO, MoO_3, Cr_2O_3, V_2O_5, NbO, ZrO_2 the change in the Gibb's energy under the normal conditions is, respectively, equal to –528, –401, –303, –180, –175, –146, –12 kJ/mole of oxygen atoms. The change in temperature within the men-

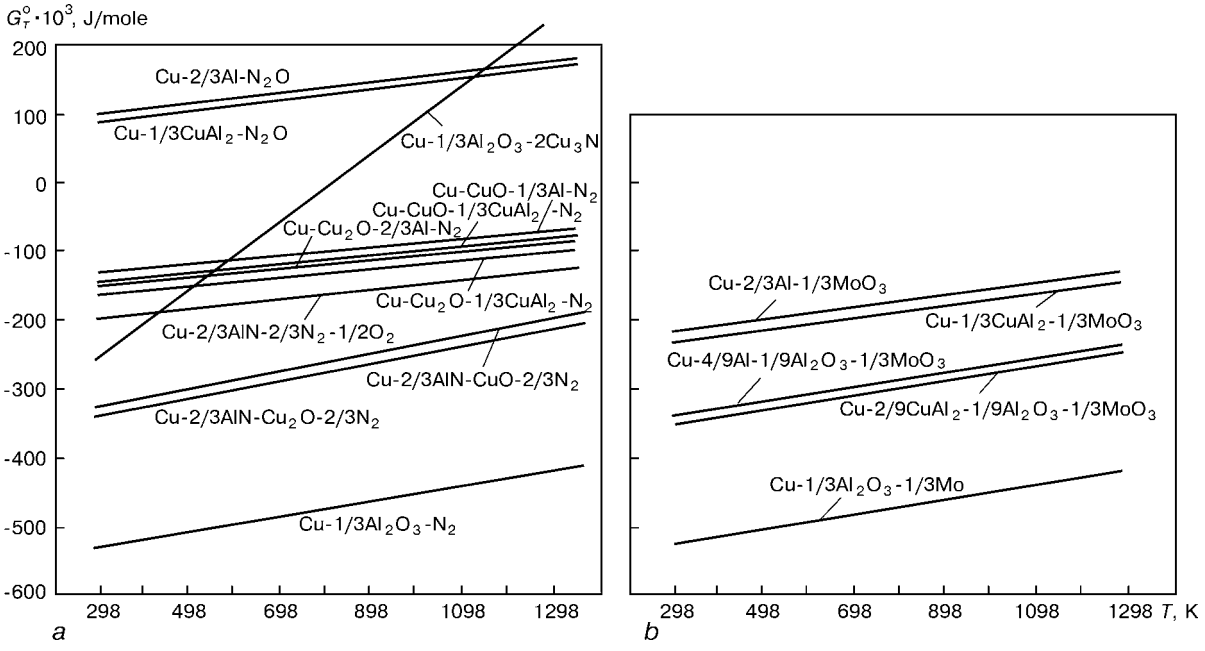

Figure 1. Effect of temperature on value of a thermodynamic potential of reaction in systems Cu–Al–N_2O (*a*) and Cu–Al–MoO_3 (*b*)

Table 2. Physical and mechanical properties of mechanically-alloyed materials

Compound composition (%)	*HB*	σ_t, *MPa*	$\rho \cdot 10^{-8}$, *Ohm·m*	*HV at T = 500 °C*	σ_{100}^{500}, *MPa*	σ_t^{500}, *MPa*	T_r, *°C*
Br.KhTsr	140	500	2.059	40	185	280	500
Redox Cu	140	465	> 2.110	–	< 190	–	700
0.8Al–2.13MoO_3	240	1020	2.216	70	250	400	850
0.8Al–3.53CuO	235	990	2.296	60	240	380	850
0.8Al–1.96N_2O	240	1010	2.203	65	245	390	850
0.8Al–1.62V_2O_5	180	720	3.182	–	–	–	–
0.8Al–2.25Cr_2O_3	175	700	3.194	–	–	–	–
0.8Al–2.73ZrO_2	175	720	3.199	–	–	–	–

tioned interval does not practically influence ΔG_T^o of the system. In compound with ZrO_2 the interaction of aluminium not with alloying oxide but with a copper to form $CuAl_2$ is most probable thermodynamically over the entire temperature interval that makes its application not justified thermodynamically as an O-containing addition.

It can be assumed that the interaction between the initial components occurs through the intermediate stages and the system does not reach equilibrium in some cases. All the thermodynamically possible transformations are established for the compositions investigated in this work. As an example, Figure 1 presents a graphical interpretation of the temperature relationship of value ΔG_T^o of these transformations in compounds with N_2O and MoO_3. The below comparison of results of the thermodynamic analysis and experimental data of the phase composition can judge about the direction of proceeding of transformations in real conditions and degree of the completion.

In this work the optimum conditions of realization of the main stages of the technological process of producing DSCM, based on a reactive mechanical alloying, were established. Depending on the nature of the alloying oxide the conditions of treatment are changed within the following ranges: 1) reactive mechanical alloying: $a = 140 - 150$ m·s^{-2}, $\varepsilon = 75 - 80$ %, $k = 9 - 12$, $T = 30 - 50$ °C, $\tau = 8 - 10$ h; 2) heat treatment of cold-pressed briquettes: $T = 700 - 800$ °C, $\tau = 6 - 8$ h; 3) hot pressing of semi-finished products: temperature of heating of the briquettes $T_{br} = 700 - 800$ °C, temperature of heating of a press tool $T_t = 500 - 600$ °C, coefficient of drawing is 12 – 17. With increase in ΔG_T^o of the redox reaction, the «rigidity» of conditions of a mechanical alloying and heat treatment should increase, while that of a hot pressing should decrease.

The physical and mechanical properties of materials produced using an optimum condition depend on the nature of an alloying oxide (Table 2) which determines the completeness of proceeding the redox transformations typical of the compositions. Comparison of theoretically-calculated and actual phase compositions, given in Table 3, can judge about the degree of their completion. Analysis of results shows that the phase transformation are progressing in systems with $\Delta G_T^o < -200$ kJ/mole of the oxygen atoms. Compositions, alloyed with Na_2O, CuO and MoO_3 belong to them. In systems with V_2O_5, NbO, Cr_2O_3, ZrO_2 the interaction between the alloying additions, aluminium and initial oxide, is proceeding partially, thus leading to the decrease in amount of a mechanically-synthesized strengthening phase (Al_2O_3) and, as a consequence,to the decrease in hardness and strength of the material. Aluminium, not bound into oxide, is dissolved in copper, thus increasing the electric impedance of the material. Non-reactive initial oxide exists in structure in the form of inclusion of ≈ 1 μm size. Coming from the analysis of a system of physical and mechanical properties (Table 2) materials alloyed with oxides N_2O, CuO and MoO_3 can be

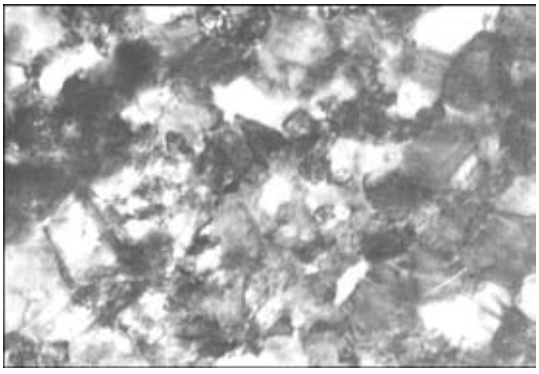

Figure 2. Microstructure of material produced from composition Cu–0.8Al–3.53CuO, TEM (×80000) (reduced by 3/5)

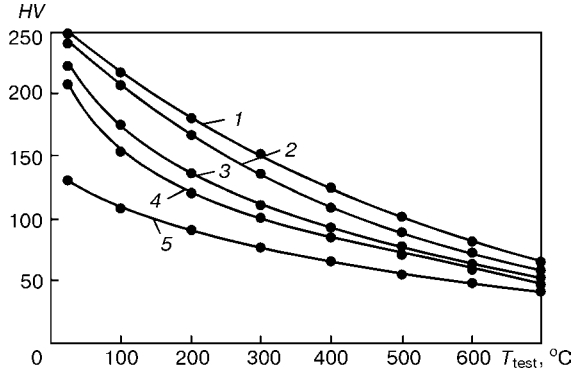

Figure 3. Relationship between the material hardness and test temperature: *1* — Cu–0.8Al–2.13MoO_3; *2* — Cu–0.8Al–3.53CuO; *3* — Cu–2.0Zr–0.3C; *4* — Cu–5.0Zr; *5* — Br.KhTsr

Table 3. Phase composition of materials

Alloying oxide	*Calculated*	*Actual*
N_2O	Cu, Al_2O_3	Cu, $CuAl_2$, Al_2O_3
CuO	Cu, Al_2O_3	Cu, $CuAl_2$, Al_2O_3
MoO_3	Cu, Al_2O_3, Mo	Cu, $CuAl_2$, Al_2O_3, Mo
V_2O_5	Cu, Al_2O_3, V	Cu(Al), $CuAl_2$, Al_2O_3, V, V_2O_3
NbO	Cu, Al_2O_3, Nb	Cu(Al), $CuAl_2$, Al_2O_3, Nb, NbO
Cr_2O_3	Cu, Al_2O_3, Cr	Cu(Al), $CuAl_2$, Al_2O_3, Cr, Cr_2O_3
ZrO_2	Cu, Al_2O_3	Cu(Al), $CuAl_2$, ZrO, ZrO_2

used as electrode materials. High values of hardness, strength and electric conductivity are determined by their phase composition and structure. Structure, presented in Figure 2, is characterized by the following parameters: size of the base grains is ≤ 0.5 μm, size of blocks is ≤ 50 nm. The base represents a low-concentrated solid solution of aluminium in copper with a ≤ 0.1 % content of alloying element. Boundaries of grains and subgrains are stabilized with inclusions Al_2O_3 of ≤ 20 nm size. There are also separate inclusions $CuAl_2$ of ≤ 50 nm size. The microcrystalline type of the structure is characterized by a developed surface of boundaries of grains and subgrains stabilized with dispersed inclusions of mechanically- and thermally-stable phases. Such structure is characterized by a low rate of proceeding of recrystallization processes and defines high values of hardness and strength not only at 20 °C, but also at the temperatures reaching 600 °C (Figures 3 – 5). It follows from data presented in Table 2 and Figures 3 – 5, that the materials developed are superior to the best classical electrode material, such as bronze Br.KhTsr, and also the experimental mechanically-alloyed materials of a carbide strengthening and a strengthening with refractory metals, by a system of physical and mechanical properties. The first material was produced from the composition Cu–2.0Zr–0.3C, the second material — from Cu–5.0Zr.

Optimum conditions of welding with electrodes from the materials developed were as follows: F = = 3 kN, I = 10 kA, τ = 0.15 s, n = 40 min^{-1}. The life of the experimental electrodes is superior to that of standard electrodes by 1.5 – 3.0 times. Effectiveness of their application increases with increase in rigidity of welding conditions, thus making it possible to implement the advanced welding technologies, based on the rigid conditions of the process at $F \approx 4.5$ kN, $I \approx$ ≈ 25 kA, $\tau \approx 0.05$ s, used at the advanced foreign enterprises, in domestic industry.

The materials and technology of their producing have found industrial implementation. Electrodes, made from them, are widely used at such large machine-building enterprises of Republic of Belarus as MAZ, MTZ, BelAZ, MoAZ, Belcard, Belcommunmash.

CONCLUSIONS

1. Technology based on a reactive mechanical alloying, provides the producing of Cu-based DSCM which are promising for manufacture of the resistance welding electrodes.

2. Materials produced at the optimum conditions using aluminium, from the one hand, and the oxides of nitrogen, copper and molybdenum, from the other hand, as alloying components, possess high physical, mechanical and service properties. Technological process of producing materials is accompanied by redox transformations which cause the formation of Al_2O_3 playing effectively the role of the strengthening phase.

3. Structure of the material is optimum if it has the following parameters: size of the base grains is

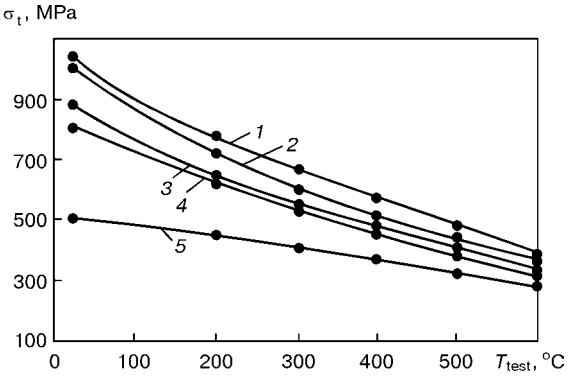

Figure 4. Relationship between the material tensile strength and test temperature: *1* — Cu–0.8Al–2.13MoO_3; *2* — Cu–0.8Al–3.53 CuO; *3* — Cu–2.0Zr–0.3C; *4* — Cu–5.0Zr; *5* — Br.KhTsr

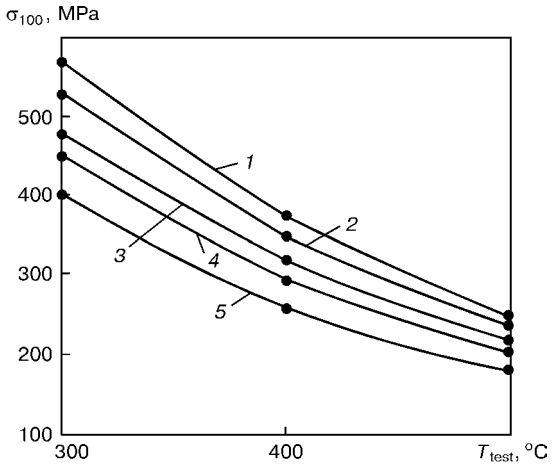

Figure 5. Relationship between the long-time (100-h) strength of material and test temperature: *1* — Cu–0.8Al–2.13MoO_3; *2* — Cu–0.8Al–3.53CuO; *3* — Cu–2.0Zr–0.3C; *4* — Cu–5.0Zr; *5* — Br.KhTsr

≈ 0.5 μm, size of blocks is ≈ 50 nm, size of inclusions of the strengthening phase (Al_2O_3) is ≈ 20 nm.

4. The Cu-based DSCM are superior, by a system of physical, mechanical and service properties, to the classical electrode bronzes, thus providing increase in life of the products made from them by 1.5 – 3.0 times.

REFERENCES

1. Anderson, S.L. *Resistance welding electrode coated with ceramic layer*. Pat. **5066845** USA, Int. Cl. B 23 K 9/24. Publ. 19.11.91.
2. Bollinger, E., Globez, P., Nowak, J.F. *et al*. *Electrode de soudage par points*. Pat. **2670700** France, Int. Cl. B 23 K 11/30. Publ. 26.06.92.
3. Kazutoyo, A., Takeshi, K., Yoshiharu, T. *Composite electrode for resistance welding*. Pat. **4947019** USA, Int. Cl. B 23 K 9/24. Publ. 07.08.90.
4. Hisashi, S., Hirosumi, H., Masaki, K. *Electrode for resistance welding*. Pat. **59-1074** Japan, Int. Cl. B 23 K 11/30. Publ. 06.01.89.
5. Todao, A., Misao, I., Kazuyoshi, F. *Manufacture of tip for resistance welding electrode*. Pat. **63-15394** Japan, Int. Cl. C 25 D 9/08, B 23 K 11/30. Publ. 19.01.89.
6. Gschossmann, N., Erras, M., Schubert, F. *et al*. *Punktschweiβ-Elektrode*. Pat. **4416504** FRG, Int. Cl. B 23 K 11/30. Publ. 16.11.95.
7. Timchuk, A.G., Kolupaeva, Z.I., Kolupaev, I.N. *et al*. *Electrode for resistance spot welding*. USSR author's certificate **1639915**, Int. Cl. B 23 K 11/30. Publ.07.04.91.
8. Grigoriev, M.M., Manujlov, V.F., Petrov, A.P. *et al*. (1997) Electrode material for spot welding of steels. *Svarochnoye Proizvodstvo*, **5**, 29 – 30.
9. Haldenwanger, H.G., Klose, P. *Elektrode zum Widerstandschweiβen*. Pat. **4323149** FRG, Int. Cl. B 23 K 11/30. Publ. 12.01.95.
10. Azuma, K., Inoue, A. *Electrodes for resistance spot welding*. Pat. **62-78683** Japan, Int. Cl. B 23 K 11/30. Publ. 24.03.87.
11. Fisher, J.C., Hart, E.W., Pry, K.M. (1953) Dispersion strengthened metals. *Acta Metallurgica*, **1**, 336 – 343.
12. Ansell, G.S., Lenel, F.V. (1960) Criteria for yielding of dispersion-strengthened alloys. *Ibid*., **9**, 612 – 616.
13. Ashby, M.F., Ansell, G.S., Cooper, T.D. (1966) Theory of critical shear stress and work hardening of dispersion-hardened crystals. In: *Proc. of Metallurgical Society Conf. on Oxide Dispersion Strengthening*. New York: Gorden@Breach.
14. (1985) *Composite materials*. Handbook. Ed. by D.M. Karpinos. Kyiv: Naukova Dumka.
15. Fedorchenko, I.M., Frantsevich, I.N., Ramomyselsky, I.D. *et al*. (1985) *Powdered metallurgy. Materials, technology, properties, field of applicaton*. Handbook. Kyiv: Naukova Dumka.
16. Portnoj, K.I., Babich, B.N. (1974) *Dispersion-strengthened materials*. Moscow: Metallurgia.
17. Avvakumov, E.G. (1986) *Mechanical methods of activation of chemical processes*. Novosibirsk: Nauka.
18. Khajnike, G. (1984) *Tribochemistry*. Moscow: Mir.
19. Vityaz, P.A., Lovshenko, F.G., Lovshenko, G.F. (1998) *Mechanically-alloyed alloys on aluminium and copper base*. Minsk: Belarus. Navuka.
20. Kireev, V.A. (1975) *Course of physical chemistry*. Moscow: Khimiya.

DETONATION COATINGS OF Ni-BASED COMPOSITE MATERIALS Information 3. TRIBOTECHNICAL PROPERTIES

V.E. MARCHUK[1], **V.F. LABUNETS**[2] and **I.B. DEREK**[2]
[1]Kyiv Air Force Institute, Kyiv, Ukraine
[2]Kyiv International Institute of Civil Aviation, Kyiv, Ukraine

ABSTRACT

Influence of a flux additive (sodium tetraboride) on the composition, structure and tribotechnical properties of a detonation coating of Ni–Cr–Fe–Si–B–Al–WC system was studied. At its optimal volume fraction of 50 %, a favourable structure of the coating, lower friction coefficient and increase of the relative wear resistance are achieved.

Key words: *detonation coating, spraying, composite powder, sodium tetraboride, structure, properties, surface layer, friction coefficient, wear resistance, adhesion*

Improvement of reliability and fatigue life of machines and mechanisms is one of the main problems in mechanical engineering. In the majority of cases it is solved by application of different kinds of protective coatings.

The most promising materials for coating application by detonation, are composite powder materials, in particular, those based on nickel and their modifications (at the expense of addition of different fluxes for brazing), which have high physical-mechanical properties [1 – 4]. Although the structure of these coatings, strength of adhesion with the base and other properties and parameters have been studied to a certain extent [5, 6], their tribotechnical properties under different conditions of contact interaction have not been thoroughly investigated so far.

In order to study the influence of a flux additive in the form of sodium tetraboride, $Na_2B_4O_7$, on the tribotechnical properties of a detonation coating of Ni–Cr–Fe–Si–B–Al–WC system, samples with the above coatings were tested in UMT-1 friction machine, using an end face pair of ring–ring type. The coefficient of overlapping in air was equal to 1.0, which corresponds to the most heavy-duty operational conditions of the friction surfaces. The wear resistance properties, as well as the influence of defects in the surface layer of the materials, are revealed to the greatest extent [7]. Quenched steel 45 (C — 0.45 wt.%; Fe — balance) was used as the mating body material.

Influence of volume fraction of sodium tetraboride in the powder composition on the tribotechnical characteristics of the studied coating

Volume fraction, %	ε	*f*
0	1.00	0.42
10	1.00	0.39
20	1.11	0.36
30	1.11	0.35
40	1.14	0.32
50	1.25	0.31
60	1.07	0.32
70	0.50	0.34

Fractographic studies were conducted by the method of scanning electron microscopy in Camscan-4 DV microscope-microanalyser with application of energy-dispersive X-ray analysis with Link-860 system. The friction surfaces of samples were studied by the methods of quantitative analysis (determination of chemical element content by ZAR-4/FLS program) and qualitative analysis (determination of the composition, which allowed finding the difference in the content of individual elements).

X-ray analysis of the coatings was performed in an X-ray diffractometer DRON-2.0. Filming was conducted in a broad angular range in monochromatic Cu_{K_α}-radiation.

The studied coatings were applied in detonation-gas unit Perun-S at a speed of 0.1 m/s and specific pressure of 1.0 MPa. Oxygen and propane-butane mixtures were used as the components of the detonating gas mixture. The duration of the coating cycles was 6.66 s. Testing results (Table 1) showed that addition of sodium tetraboride to the initial composite powder (not containing any flux additive), leads to a considerable lowering of the friction coefficient *f* and increase of the relative wear resistance ε of the detonation coating. The maximal value of the latter and the minimal value of the friction coefficient correspond to a modified coating, the powder composition for which has the volume fraction of sodium tetraboride of about 50 %.

Fractographic studies of friction surfaces of the tested samples revealed that they develop three characteristic zones Z_1 — Z_3 (Figure 1, *a*). Their 200-fold magnification (Figure 1, *b* – *d*) and determination of the quantity of alloying elements on the friction surface (Figure 2, *a*), demonstrated that heterogeneous

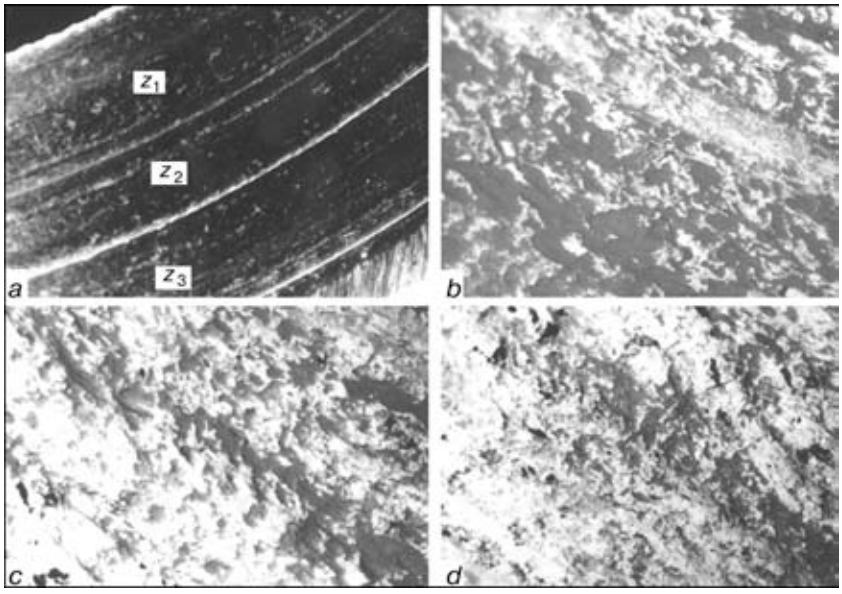

Figure 1. Microstructure of the friction surface of the initial coating: general view (*a*) (×20); zones Z_1 (*b*), Z_2 (*c*) and Z_3 (*d*) (×200) (reduced by 1/2)

thermal activation processes are observed in each zone of the initial coating. This is due to different contact temperature $T_1 < T_2 < T_3$ of $Z_1 - Z_3$ zones, the rise of which is promoted by the increase of the appropriate angular velocity $\omega_1 < \omega_2 < \omega_3$. On the other hand, no such zones are found on the friction surface of modified coatings which have sodium tetraboride added to their composition (Figure 3, *a*).

The friction surfaces of samples with initial coatings in zone Z_1 (Figure 1, *b*) were found to have a large number of dark regions which are the destroyed structures formed at the as a result of undesirable processes of adhesion and transfer of the mating body material to the coating surface. Increase of angular velocity $\omega_1 < \omega_2 < \omega_3$ results in reduction of the dark areas on the friction surface (Figure 1, *b* – *d*). The coating with sodium tetraboride in the powder composition, differs by a much smaller number of dark areas, compared to the initial coating, which is practically the same in all the zones (Figure 3, *b* – *d*).

Based on the results of X-ray analysis performed in Camscan-4 DV microscope-microanalyser, it was established that the dark regions observed on the friction surface of the studied coatings, contain 3 – 4 times more oxygen, than the light regions (Figure 4). For convenience of observation, the energy spectrum was expanded using LZ-5 detector.

Presence of a large amount of oxygen in the dark regions is due to formation on the secondary structure fragments, of protective films resulting from oxidation. This process is accompanied by their embrittlement, softening and subsequent fracture.

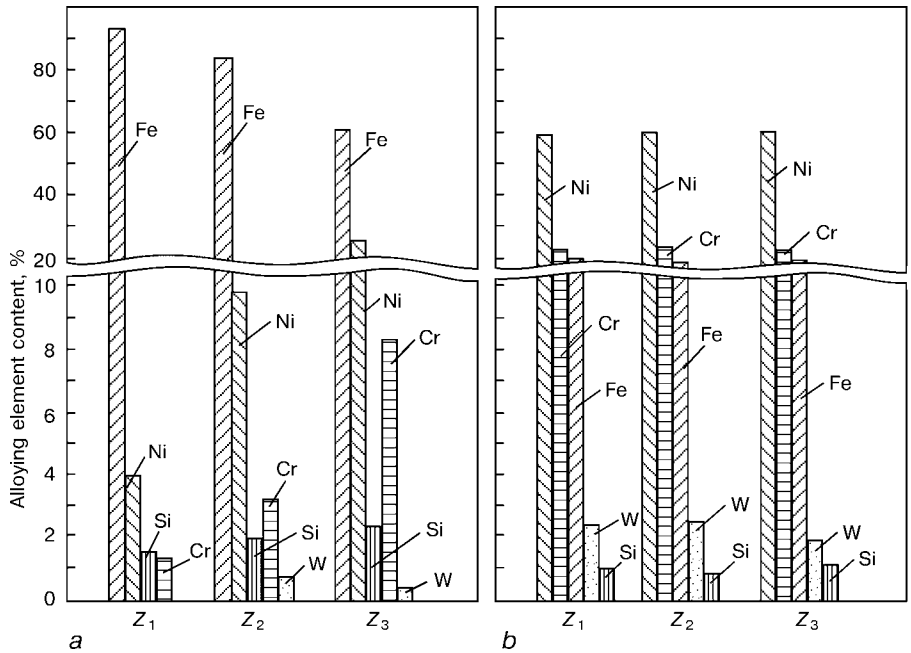

Figure 2. Quantitative composition of alloying elements on the friction surface of the initial coating (*a*) and modified coating (*b*) with 50 % volume fraction of sodium tetraboride in the powder mixture

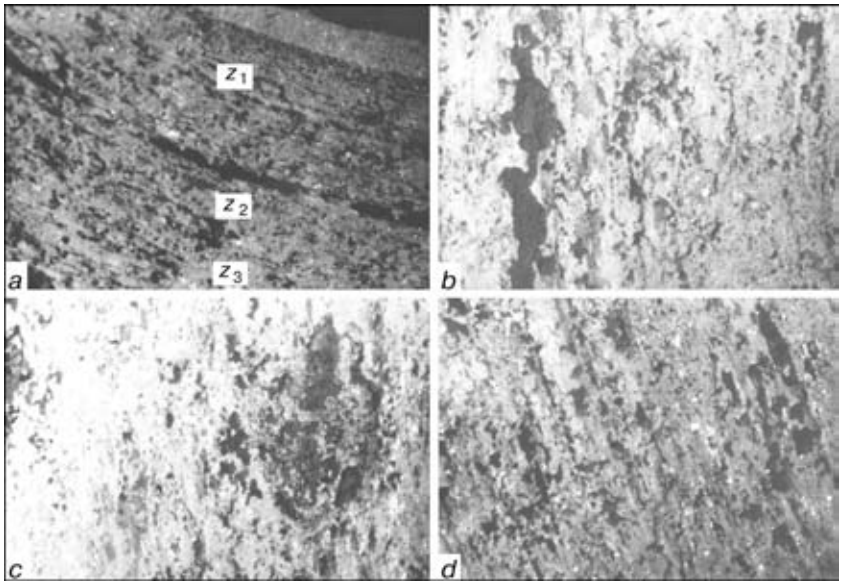

Figure 3. Microstructure of the friction surface of a modified coating, containing 50 % sodium tetraboride in the powder composition: general view (*a*) (×20); zones Z_1 (*b*), Z_2 (*c*) and Z_3 (*d*) (×200) (reduced by 1/2)

By the data of X-ray analysis, the light sections on the friction surface, are a complex of structures in the form of binary compounds of spinel type based on nickel, chromium, tungsten, aluminium oxides and boron anhydride.

Quantitative analysis of alloying elements in the coating surface layers, demonstrated the non-uniformity of the former in the studied zones. So, the initial coating zone Z_1 (Figure 1, *b*) is characterized by the highest content of iron on the friction surface (93.2 % of the overall content of alloying elements on the surface), which drops to 84 and 61 %, respectively, when going over to zone Z_2 and further on to Z_3 with a minor increase of the amount of chromium and nickel (Figure 2, *a*).

The process of wear of the initial coating is characterized by the prevailing oxidizing process, accompanied by inadmissible wear, namely adhesion of the 1st kind. Formation of centers results in transfer of wear products from the mating body surface onto the specimen friction surface in the form of earlier described dark regions, which from the results of X-ray phase analysis are a mixture of Fe_3O_4 and γ-Fe_2O_3. The films formed on the friction surface are brittle, and have a low adhesion strength. A considerable area occupied by them on the friction surface, promotes intensification of the adhesion processes, which leads to a greater friction coefficient and lowering of the relative wear resistance of the initial coating (see Table).

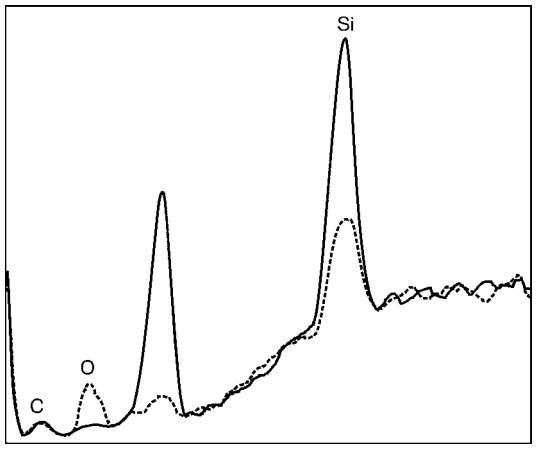

Figure 4. Energy spectra of element distribution over the friction surface of the studied detonation coating (dashed curve — dark regions, solid curve — light regions)

Based on the results of chemical analysis of the friction surface of samples with the initial coating (Figure 2, *a*), it can be anticipated that the wear is non-uniform in each of the three zones. It is the strongest in zone Z_1 as the intensity of the processes of fracture (adhesion) and area occupied by iron oxides, are the greatest, compared to other zones. The wear is the smallest in zone Z_2.

According to the results of quantitative analysis of the friction surface of samples with the studied modified detonation coating (Figure 2, *b*) the composition of alloying elements is constant in each of the three zones. Nickel prevails in them (59 %), followed (in the order of decreasing) by chromium (21 – 22 %), tungsten (2 %). Therefore, the thermal activation processes in each zone proceed in a practically uniform fashion. Iron content was markedly reduced (down to 15 %) on the surface of all the three zones, with iron occupying small regions in the form of dark spots (Figure 3, *b* – *d*). This leads to high values of relative wear resistance and low friction coefficients (see Table), as well as the absence of any noticeable traces of adhesion on the friction surface of samples with a modified coating, compared to the initial coating in which the adhesion processes are intensive.

Increase of the volume fraction of sodium tetraboride (above 55 %) in the initial powder composition, leads to a decrease of relative wear resistance and increase of the coefficient of friction of the studied coating. This is related to increase of the coating ductility at the expense of microhardness drop [4], which

leads to deformation (crushing) of subsurface layers. Positive influence of the latter is manifested only in the initial process of running-in, when it somewhat compensates the existing deviation from the specified macro- and microgeometry of the surfaces and allows improving the contact between the mating parts of the friction unit. Under the conditions of stable friction, subsurface deformation has a markedly adverse effect, as it becomes the source of inadmissible processes of the part surface damaging [8]. The surface layer also develops inadmissible values of plastic flow.

CONCLUSIONS

1. Addition of sodium tetraboride to the applied Ni-base powder composition, essentially changes the tribotechnical characteristics of detonation coatings.

2. The intensity of wear and coefficient of friction of coatings depend on the structure of their surface layers, determined by the nature of the alloying elements distribution.

REFERENCES

1. Borisov, Yu.S., Kulik, A.Ya., Mnukhin, A.S. *et al.* (1985) *Thermal spraying of composite powders*. Leningrad: Mashinostroyeniye.
2. Borisov, Yu.S., Kharlamov, Yu.A., Sidorenko, S.L. *et al.* (1987) *Thermally-sprayed coatings of powdered materials*. Refer. Book. Kyiv: Naukova Dumka.
3. Labunets, V.F., Marchuk, V.E., Shchepetov, V.V. (1996) Detonation coatings of Ni-based composite materials. Information 1. Influence of flux additive on the composition, structure and properties of coatings. *Avtomaticheskaya Svarka*, **10**, 19 – 23.
4. Marchuk, V.E., Labunets, V.F. (1997) Detonation coatings of Ni-base composite materials. Information 2. Physico-mechanical properties. *Ibid.*, **7**, 23 – 25.
5. Nosovsky, I.G., Shchepetov, V.V., Marchuk, V.E. (1994) Detonation coatings for protection of the friction units from wear. *Nauka i Oborona*, **2**, 126 – 135.
6. Venediktov, V.A., Sharypov, A.Z., Khoshenin, A.I. *et al.* (1980) Improvement of the service life of compressor blades by application of wear-resistant detonation coatings. *Treniye i Iznos*, **6**, 1093 – 1096.
7. Kostetsky, B.I., Nosovsky, I.G., Bershadsky, L.I. *et al.* (1975) *Reliability and fatigue life of machines*. Kyiv: Tekhnika.
8. Kostetsky, B.I., Nosovsky, I.G., Bershadsky, L.I. *et al.* (1978) *Surface strength of materials in friction*. Kyiv: Tekhnika.

PROSPECTS FOR ELECTRON BEAM WELDING OF BIMETAL BAND SAWS AND SAW BLADES IN UKRAINE

O.K. NAZARENKO, Yu.V. ORSA and **G.Ya. STOLIKO**
The E.O. Paton Electric Welding Institute, NASU, Kyiv, Ukraine

ABSTRACT

Analysed is the ability of Ukrainian organisations to set up production of band saws and hack-saws in the bimetal variant, when the cutting part of the tool is made of high-speed steel, and the base — of carbon or low-alloyed steel. Given are the results of studying the technology of electron beam welding (EBW) and heat treatment of various combinations of steel, as well as industrial application of the locally-made equipment.

Key words: *saw blades, hack-saws, bimetal blank, cutting edge, high-speed steel, drawing, base, cutting force, heat treatment, EBW, pilot production trials, introduction*

The problem of development of highly-efficient and also inexpensive cutting tools is still urgent now. A very clear tendency over the last years has been to manufacture mostly bimetal variants of the tools, when their cutting part is made of high-speed steel, and the base — of carbon or low-alloyed steel. A welded bimetal band blank is widely used in manufacture of saw blades, especially of continuous circular saws for band cut-off machines (Figure 1), thus allowing 80 to 90 % reduction of high-speed steels consumption. These so-called band saws have such advantages as high efficiency (1.5 – 2.0 times higher than that of milling/cutting-off machines and 2 – 3 times higher than that of the sawing machines); a narrow cut with its high precision and finish of the surface.

Despite the possibility of applying a number of processes for welding the cutting edge to the band base (microplasma, with resistance heating of the edges by sliding electrodes, diffusion, high-frequency currents, EBW is the most widely accepted method [1 – 4]. It provides a high quality of the welded joint with maximal efficiency, and allows complete automation of the entire technological cycle. A number of companies in the USA, FRG, Great Britain and France, developed the technology and specialised equipment for commercial production of a bimetal band blank by EBW process [5 – 7].

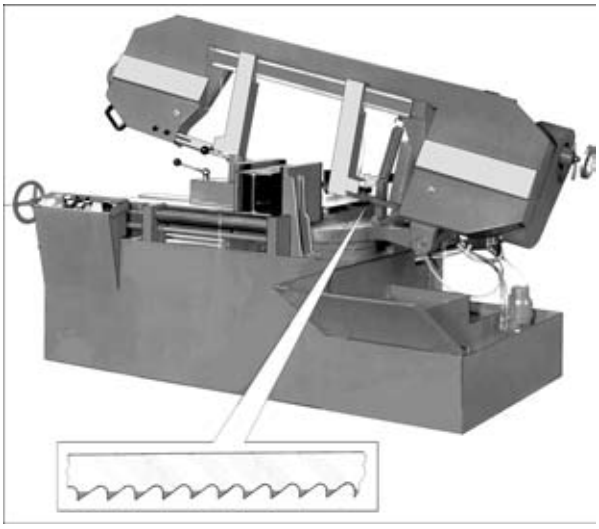

Figure 1. Horizontal band cut-off machine with bimetal circular saw, produced by EBW process

In the information booklets of the companies manufacturing bimetal band saws and saw blades it is emphasised that in addition to lowering the cost of the cutting tool, improvement of its quality, reliability and performance is also provided. So, for instance, Doall Company (USA) was one of the first to use the electron beam for joining classical high-speed steels to the tough material of the base for manufacturing high-quality cut-off bimetal saws. Its «Imperial Bimetal Blades» are designed for cutting special alloys and dispersion-hardening materials. The ends of their teeth are treated up to the hardness of *HRC* 64 – 65, with the cutting part having the resistance to vibration and shock loads 10 times higher than that of the standard monolithic saws. Hawker Company (Great Britain) applies EBW of the cutting part of M3 high-speed steel to the base of a ductile chromium-vanadium En-47 steel in manufacture of band saws and hack-saws. By the data of this company, such bimetal saws and hack-saws accommodate much higher speeds and forces of cutting than the regular saws [8].

Foreign manufacturers use low-alloyed steels SAE-6150 and D6A (USA), Sk-60 (FRG), En-19 and En-47 (Great Britain) as the material for the back (carrying) part of bimetal band and hack-saws. For the cutting part, a narrow band blank 0.9 – 1.5 mm wide of high-speed 651 and 652 steels (AISI-M series) is used in the USA, and of S6-5-2 steel in FRG and M2 and M3 steels in Great Britain. Chemical composition of these steels is given in Table 1.

A feature of the first designs of specialised units of Sciaky and Steigerwald Strahltechnik Companies for EBW of band blanks was placing the blank coils and the welded bimetal band in pumped-down load

Table 1. Composition of steels used by foreign companies for fabrication of the bimetal blank

Part of blank	Steel grade	Content of elements, wt.%									Country
		C	Si	Mn	S	P	Cr	Mo	W	V	
Base	SAE-6150	0.33 – 0.48	0.20 – 0.35	0.70 – 0.90	0.040	0.040	–	–	–	0.15	USA
	Sk-60	0.70 – 0.80	0.30	0.50	–	–	–	–	–	–	FRG
	En-19	0.35 – 0.45	0.10 – 0.35	0.50 – 0.80	0.050	0.050	0.90 – 1.50	0.20 – 0.40	–	–	GB
	En-47	0.45 – 0.55	0.50	0.50 – 0.80	0.050	0.050	0.80 – 1.20	–	–	0.15	GB
	Sk-70-2	0.50 – 0.62	0.20 – 0.37	0.50 – 0.80	0.050	0.050	–	–	–	–	FRG
Cutting	M2	0.80 – 0.85	0.20 – 0.40	0.20 – 0.40	0.025	0.025	4.00 – 4.25	5.00 – 5.25	6.00 – 6.50	1.90 – 2.00	GB
	S6-5-2	0.78 – 0.86	0.40	0.40	0.025	0.025	4.25	5.20	6.70	2.00	FRG
	652, (M3)	1.10 – 1.20	0.10 – 0.40	0.10 – 0.40	0.025	0.025	4.00 – 4.25	5.00 – 6.25	5.60 – 6.25	3.00 – 3.30	USA, (GB)
	651, (M3A)	1.00 – 1.10	0.10 – 0.40	0.10 – 0.40	0.025	0.025	4.00 – 4.25	5.70 – 6.25	6.00 – 6.25	2.40 – 3.25	USA, (GB)

chambers to the left and right of the working chamber (Figure 2). 300 m long blank is welded in such a unit at 5 – 6 m/min speed in one cycle. After welding is over, the coils are replaced, and the cycle is repeated.

Steigerwald Strahltechnik Company, now part of IGM Robotersysteme AG (FRG), developed and produces in quantity an automatic welding unit for making a bimetal blank for band saws and saw blades. The schematic of this unit, namely air–vacuum–air, which has already become classical, is given in Figure 3. The continuity of EBW process is achieved by application of input and output load locks, which are exposed to vacuum of different degrees of rarefaction, as well as a system of differential pumping down of the gun. Maximal efficiency of the unit in production of the blanks is up to 900 m/h, and the power of the applied electron beam equipment is 8.5 kW at the accelerating voltage of 135 kV [10]. The appearance of the welding unit of Steigerwald Strahltechnik Company is shown in Figure 4. The unit for EBW of band blanks, manufactured by Techmeta Company (France) is designed along similar lines.

Analysis of the status of manufacturing and consumption of tool products in Ukraine demonstrated that so far in the local factories the bars and structural shapes are cut by imported from Russia band saws of V2F (C — 1.0; W — 2.0; V — 0.25 wt.%) tool steel and high-speed R6M3 (C — 0.9; Cr — 4.0; W — 6.0; Mn — 3.0 wt.%) steels. Expensive Kh6VF (C — ≤ 0.15; Cr — 6.0; W — 1.0; V — 1.0 wt.%) steel, also produced in Russia, is used to manufacture hacksaw blades. On the other hand, mastering the production of bimetal band saws and saw blades in Ukraine certainly appears both possible and rational, considering the high demand for these products in the world.

Over the last five to six years, PWI, in co-operation with a number of Ukrainian enterprises and organisations has performed preparatory work for mastering the production of bimetal strip blanks in Ukraine. In this case, the main attention was given to the following issues.

Selection of materials for the bimetal blank. The composition of the selected materials should correspond to the following requirements:

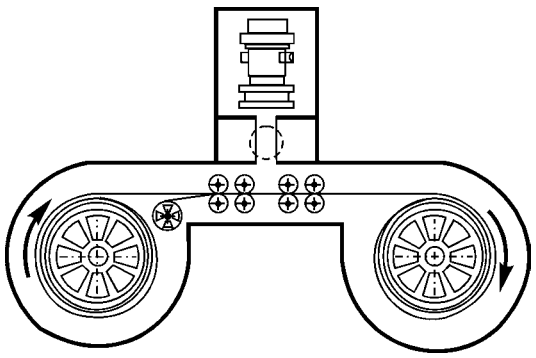

Figure 2. Diagram of a cyclic-operation unit for EBW of strip blanks with the coils located in pumped-downs chambers

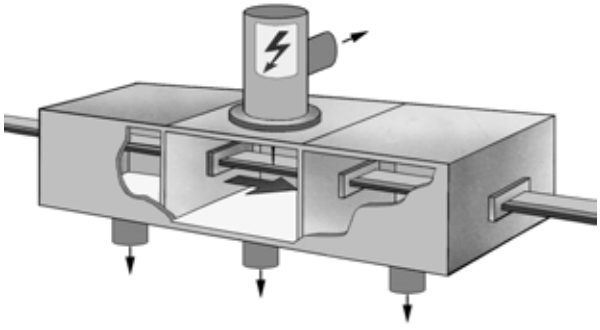

Figure 3. Diagram of Steigerwald Strahltechnik unit of air–vacuum–air type

Table 2. Composition of local steel grades suitable for fabrication of welded bimetal strip

Blank part	*Steel grade*	*Content of elements, wt.%*									
		C	*Si*	*Mn*	*Cr*	*Mo*	*W*	*V*	*Co*	*S*	*P*
Base	50KhFA for strip	0.46 – 0.54	0.17 – 0.37	0.50 – 0.80	0.80 – 1.10	–	–	0.10 – 0.20	–	0.025	0.025
Cutting	R6M5 for wire of 1.20 – 2.20 mm dia., no specifications available*	0.82 – 0.90	0.50	0.50	3.80 – 4.40	4.80 – 5.30	5.50 – 6.50	1.70 – 2.10	0.50	0.025	0.030

*Test batch produced by OAO «Dneprospetsstal» was used.

• satisfactory weldability of the selected metal pair by the EBW process;

• possibility of their simultaneous heat treatment by a mode, providing the optimal properties in the cutting part of the strip and high performance of the base part;

• machining (stamping, straightening, saw-toothing, saw-setting) of the bimetal strip in the equipment available in the local tool making factories should correspond, as to labour consumption, to machining the traditionally used monolithic strip blank of Kh6VF, U-10A, V2F and R6M3 steels [11];

• already mastered metallurgical production of the selected steels.

Proceeding from these requirements, we have selected spring steel of 50KhFA grade (GOST 14959–79) for the base part of the saws and blades. Presence of chromium and vanadium in its composition promotes less intensive grain growth in heating above 1100 °C. For the cutting part of the bimetal strip, preference is given to electroslag remelted high-speed steel R6M5. It has better ductility (at the temperatures of 900 – 1150 °C) and much lower carbide inhomogeneity, compared to R9 (C — 0.9; Cr — 4.1; W — 9.0; V — 2.5 wt.%) and R18 (C — 0.75; Cr — 4.1; W — 18.0; V — 1.2 wt.%) steels, but is close to them in its cutting properties. The composition of steels, selected for the bimetal blank of the band and hack-saws and saw blades is given in Table 2.

Development of the technology of fabrication of the strip blank for the cutting edge of R6M5 steel. In the best foreign band saws and saw blades the width of the cutting edge does not exceed 1.6 mm.

Figure 4. Batch-produced Steigerwald Strahltechnik unit of air–vacuum–air type for EBW of bimetal blanks

The minimal width of the produced in Ukraine strip blank of tool and high-speed steels is 10 mm at the required thickness of 0.6 – 2.0 mm (GOST 2283–79). On the other hand, the local factories have mastered the production of high-speed ball bearing steel R6M5sh in the form of wire of extremely small cross-section (smaller than 3 mm^2). This necessitated development of the technology of production from this wire of rectangular shapes of the cutting edge of the following dimensions: 1.60×0.63 mm (for saw blades) and 0.95×0.95, 1.50×1.15 and $1.60 \times$ $\times$ 1.35 mm (for band saws).

When preparing the specification for the cutting edge blank we used as the prototype, similar products of Sandvik Company (Sweden) — world leader in the field of bimetal tools and equipment for its production. In this case the main parameters of the cutting edge blank, welded to the strip base by EBW, should be as follows:

limit deviation, mm
- by width ..... ±0.025
- by thickness ..... ±0.025

admissible radius of angles rounding-off, mm, not more than 0.08

non-perpendicularity of the vertical and horizontal surfaces of the strip, degr., not more than ..... ±0.5

side surface roughness, R_a, μm, not more than 3.2

depth of decarburized layer of the strip, mm, not more than 0.01

No films, rolled-in scale or tears are allowed on the strip surface. The size of isolated scratches, marks, imprints and pitted surface should not be more than half of limit deviations of thickness.

The developed technology of making the strip blanks was based on the process of continuous drawing through 4 roll drawing dies, used in rolling production (Figure 5). Intermediate flattening of the sections was performed in drive rolls with strands of a certain section. Strip winding at the end of a pass was performed with a double capstan followed by turn-by-turn winding on the take-up spool. The drawing process was conducted in two passes (6 process stages). The height of building-up the hard-alloy roll drawing dies and replaceable roll strands to produce the main type sizes of the cutting edge from R6M5sh steel wire is given in Table 3. The lubricant used was an emulsion based on the local «Leol-M» preparation, which easily washes off with hot water.

Table 3. Dimensions of rectangular sections of the cutting edge of R6M5sh wire during its rolling-drawing

Initial wire diameter, mm	*Pass No.*	*After drawing die No.1*		*After roll stand*		*After drawing die No.2*	
		Width, mm	*Thickness, mm*	*Width, mm*	*Thickness, mm*	*Width, mm*	*Thickness, mm*
1.8	1	1.30	1.20	1.40	1.10	1.20	1.05
	2	1.10	1.05	1.20	1.00	0.95	0.95
2.0	1	1.90	1.70	2.00	1.50	1.70	1.40
	2	1.50	1.40	1.70	1.20	1.50	1.15
2.2	1	2.00	1.80	2.20	1.63	1.80	1.50
	2	1.70	1.50	1.80	1.40	1.60	1.35

Note: Limit deviation of the above dimensions of the section in width and thickness is ±0.025 mm.

As high-speed R6M5 steel belongs to the group of difficult-to-deform steels and the hardness of the surface layer of the strip is HV 320 – 340 after the first pass, the initial strip bundle was subjected to recrystallization annealing, in order to relieve the work hardening. The blank annealed to the hardness of HV 230 – 260 was drawn to the final (finish) size in the second pass.

Carbide tempering is recognised to be a more advanced technique to remove the work hardening in rolling of difficult-to-deform steels, which consists in heating the cold-rolled high-speed steel to the temperature of 720 – 760 °C with subsequent rapid cooling in water or oil. In this case, the latter operation fixes the observed partial dissolution of finely dispersed carbides [12]. Such a tempering results in lowering of the steel yield point by 15 to 20 %, which raises its deformability in the cold state to a sufficient degree, and eliminates the probability of surface cracking. The lack of the appropriate local equipment (continuous-operation multistrand furnace with a shielding atmosphere) prevented us from applying this method in practice.

Development of the technology of production of a welded bimetal strip for fabrication of blade saws and saw blades. A unit of ELS-101 type was used for development of the technology of continuous welding of two- or three-strip blanks (Figure 6). It incorporates double uncoilers for strip blanks and take-up units for the welded strip, respectively, as well as a loop accumulator. This allows avoiding interruption of EBW process when the coils are replaced. Two electron beam guns can also be used simultaneously, thus permitting welding of the base strip of a double width to two cutting edge blanks simultaneously. The thus produced welded blank is cut in half after heat treatment.

The technique of welding with the backward-inclined beam was used, in order to protect the cathode surface from the detrimental effect of the vapours of the metals being welded under the conditions of its long-term and continuous operation. The beam axis was deflected from the vertical through an angle of 5°. Fixation of the strips to be welded and their relative positioning in the welding zone, were provided by an aligning device, set up for a certain size of the blanks. The aligning device was mounted on the mobile wall of the vacuum chamber. For setting it up, or its readjustment when switching to another type size of the strips, it is enough to move out the wall chamber along the strip axis in the direction of welding.

The strips were prepared for welding by degreasing them with subsequent washing in the continuous baths and hot drying. Directly before welding, the blanks were demagnetised by the method of periodical reversal of the magnetisation by alternating current of a decreasing amplitude and commercial frequency. The working distance from the lower edge of the welding gun to the strip surface in the aligning device was 80 mm, at 0.3 Pa residual pressure in the welding chamber.

The requirements to the quality of the weld, joining the back-base to the cutting edge, are quite high, as in the saw operation, tearing away of just one tooth

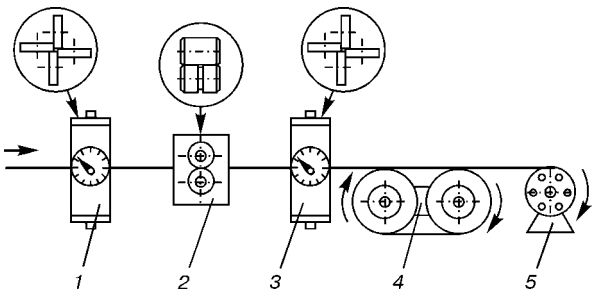

Figure 5. Flow chart of drawing rectangular section of the cutting edge of bimetal saws of R6M5sh wire: *1, 3* — 4 roll drawing dies; *2* — drive roll stand; *4* — double capstan; *5* — take-up spool with laying device

Figure 6. ELS-101 unit for welding of bi-, trimetal strip blank (developed by PWI)

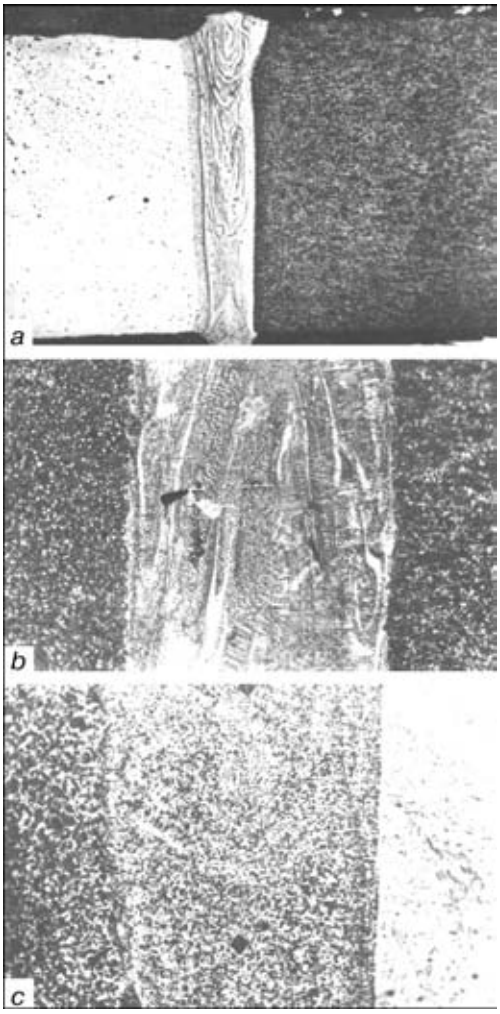

Figure 7. Macro- (*a*) (×50) and microstructure of welded joints of R6M5–50KhFA steels after welding (*b*) and after heat treatment in the mode standard for R6M5 steel (*c*) (×400) (reduced by 2/3)

invariably leads to chipping of the others. Having analysed foreign publications [3, 4] and information provided by the local band saw producers, we have defined the following requirements to the geometry and quality of welded joints: guaranteed penetration of the butt; presence of weld reinforcement both from the face and the root side of the weld; inadmissibility of cracks and burns-through; level of porosity of not more than three pores, having the diameter less than half of the weld width per 200 mm of its length; weld width of not more than 0.4 mm from the face side and 0.25 mm from the root side; angle of inclination of the fusion boundary (non-parallelism of the edges) of not more than 6°.

In this case, EBW of the strips should be performed at a speed of not less than 400 m/h for the band saw blanks 0.95 – 1.35 mm thick and 600 m/h, respectively, for saw blade blanks 0.63 mm thick.

The performed experiments revealed that when electron beam equipment with 60 kV accelerating voltage is used, the above requirements can only be satisfied in welding strips up to 0.8 mm thick (type size of the saw blade blank). ELA-120/6 power unit of 6 kW power with accelerating voltage of 120 kV, was developed for EBW of blanks of blade saws up to 1.95 mm thick. Figure 7, *a* gives the transverse macrosection of a bimetal welded blank for a band saw 1.35 mm thick (welding speed of 7.8 mm/min, beam current of 12.5 mA).

Metallographic investigations, including evaluation of the microstructure (after etching in 4 % solution of HNO_3) and hardness determination in different zones of the weld, were performed in order to evaluate the quality of welds and analyse the structural changes in bimetal joints. Microhardness of individual structural components was measured in M400 hardness meter of LECO Company at the load of 0.98 N for 10 s. Photos were taken in metallographic microscope Polyvar-Met with ×400 magnification.

Investigations were conducted on samples of strip blanks after welding, as well as complete heat treatment, which was performed by a standard mode, used for tools of steel R6M5 (quenching and triple tempering). In addition, immediately following EBW, the bimetal strip was subjected to isothermal annealing, which was done in nitrogen atmosphere in order to prevent decarburizing of the cutting edge surface. The possibility of replacing long-term annealing (18 h) of the strip by a shorter (about 12 h) high-temperature tempering at the temperature of 750 °C, was later confirmed by practical work. This allowed the hardness in the vicinity of the welded joint to be lowered to the level of *HV* 240 – 280, required for straightening the welded strip, rolling flat the weld reinforcements, milling out the teeth and their setting.

Quenching was performed by the following mode: heating in the salt bath, namely preliminary heating up to 900 – 950 °C (soaking for 50 s) and final heating up to 1210 °C (soaking for 50 s); cooling in a saltpeter bath at the temperature of 250 °C (soaking for 3 min) and further cooling in air.

Triple tempering was performed at 540 °C, with soaking for 60 min and cooling in air.

Heat-treated samples were used for hardness measurements, structural studies, detection of defects in welded joints and determination of the susceptibility of the latter to cold cracking.

The results of metallographic investigations of samples of strip blanks revealed the following. After welding the weld metal hardness in the fusion zone, both from the side of R6M5, and from the side of 50KhFA, is equal to *HV* 750 – 850. In the HAZ region from the side of the base part, it smoothly decreases to *HV* 280 – 320, and from the cutting edge side, it is on the level of *HV* 530 – 550 (troostite-martensite structure) with a subsequent decrease to *HV* 270 – 290 at the edge (sorbite-like pearlite). Such a hardness gradient in the vicinity of the weld, is indicative of a rather high level of internal stresses.

The microstructure of the welded joint in as-welded condition is given in Figure 7, *b*. When a series of microsections were studied, the welds and the HAZ did not reveal any defects (individual pores of an admissible size, namely of the diameter smaller

than half of the blank thickness, were found). In order to avoid the possible brittle fracture of the bimetal joint of R6M5–50KhFA in rewinding and transportation of the welded strip, the latter is to be subjected to high-temperature tempering right after welding.

After complete heat treatment the hardness of the cutting edge was *HV* 860 – 900, that of the base part *HV* 410 – 425. The weld metal hardness is highly non-uniform — this value varies from *HV* 650 to 820. No regions of ledeburite eutectic lowering the weld strength, were found. Figure 7, *c* gives the microstructure of the R6M6–50KhFA welded joint after complete heat treatment.

Samples of bimetal welded joints were also tested to evaluate their cold cracking resistance. At loading up to stresses equal to $54 \cdot 10^5$ Pa (50 % of σ_y value for 50KhFA steel), and soaking for 5 days, the tested joints did not have any cracks. This is indicative of their rather high resistance to cold cracking.

After milling and heat treatment the hardness of band saw teeth was *HRC* 62 – 64. The weld in them is located above the recess line, the height of the high-speed steel part of the tooth being 0.5 – 0.7 of its total height. Milling of the saw band teeth was performed within the cutting edge of R6M5 (without cutting into the weld).

Testing of pilot samples of band saws, made of a bimetal welded blank of 40.00 × 1.35 mm size, was conducted in Romny «Poligrafmash» factory by the factory procedure. In this case, the resistance of bimetal saws (life to failure) was 0.2 – 0.6 m^2 per 1 m linear length of the saw, depending on the processing mode and material being cut, this being not less than 40 % higher than the resistance of band saws of steel of one grade.

A test batch of bimetal saw blades was made of a welded blank of 13.80 × 0.63 mm size and tested to GOST 6645–86 in the Lugansk Machine-tool Factory. It turned out that the resistance of the bimetal saw bands exceeded that of the standard bands of Kh6VF die steel at least by 2.5 – 3.0 times, with incomparably higher service reliability (the bimetal band does not break when rolled up into a ring, and there are no traces of plastic deformation).

Introduction of the developed technology into industry. The experience gained by us in development of ELS-101 unit and optimisation of the technology of continuous high-speed EBW of bimetal strip blanks, was used during fulfilment of a contract between PWI and PATON-GLESI Joint Venture (Guiling, China) and one of the tool-making factories in Shanghai.

The developed welding unit (Figure 8) of air–vacuum–air design, is fitted with double uncoilers for the strip blanks and take-up units for the welded strip. The electron beam gun was specially designed for continuous long-term operation (not less than 18 h/day). The high-voltage power source is fitted with a quick-response electronic system of protection

Figure 8. General view of the unit for EBW of a bimetal strip put into operation in Shanghai (China)

from possible breakdowns in the welding gun [13]. Alignment of the electron beam with the butt of the strips to be welded, is performed by transverse displacement of the welding gun relative to the axis of the strips using a scanning TV system with 10-fold magnification of the image. The maximal output power of the source is 6.0 kW at the accelerating voltage of 120 kV.

This unit, which was put into commercial operation at the end of 1998, produced more than 90 tons of welded bimetal blanks of different type sizes from 14.00 × 0.63 mm (for hack-saw blades) up to 38.00 × × 1.95 mm (for machine saws) in 1999. The main type sizes of the produced welded blanks for band saws are as follows: 25.40 × 0.95, 31.80 × 1.15 and 40.00 × × 1.35 mm. The welding speed is 12 m/h, and the time required for readjustment of the unit from one type size of the bimetal strip to another one, is not more than one hour.

Thus, the positive results of technological and pilot-design development performed in the PWI, in principle, confirm the possibility of fabrication of tools of this class in Ukraine with participation of the following enterprises and organisations:

- OAO «Dneprospetsstal» having the production capability for annual supply of up to 100 tons of bundles of R6M5sh or R6M5sp wire;
- A.A. Galkin Donetsk Physico-Technical Institute of the NAS of Ukraine, which developed the technology of production of the cutting edge blanks of the required profile and size and which has the appropriate production facilities;
- «Zaporozhstal» Metallurgical Works, which has the technology, including the equipment required for production of cut cold-rolled strip of 50KhFA steel (GOST 14959–79), and is ready to master its commercial scale production (until recently this strip has

been produced in quantity by Russian «Izhstal» Works);

• E.O. Paton Electric Welding Institute of the NAS of Ukraine, which has the technology, including specialised electron beam welding equipment for production of welded bimetal blanks for band saws and saw blades;

• Romny «Poligrafmash», Zhitomir «Avtozapchasti», Lugansk Machine-tool Factory, Vinnitsa and other tool-making factories, where the production of bimetal tools can be deployed mostly using the equipment available in these factories.

REFERENCES

1. Lin, Y.C., Sun, C.Y., Chen, X. (1987) Investigation of the equipment and technology of partial vacuum electron beam welding in the continuous manufacture of bimetallic saw blades. *Transact. of China Welding Inst.*, **1**, 31 – 37.
2. Sommeria, J. (1978) Continuous electron beam welding of bimetallic strip. In: *Proc. of 2nd Int. Colloq. on Electron Beam Welding and Melting*, Avignon, France, Sept. 5 – 8.
3. Wilcox, R.G., Yerger, W.R. (1978) Factors affecting the quality of electron beam (EB) welding. *Metal Progress*, **4**, 28 – 35.
4. Burns, T.E. (1975) Applications of electron beam welding. *Metal Construction*, **6**, 333 – 337.
5. Laflamme, G., Kuoefel, J. (1987) Application of electron beam welding. In: *Proc. of the Int. Conf. on Applications of Electron and Laser Beam Welding*, Hartford, Sept. 16 – 17. Miami: AWS.
6. Elliot, S., Dunkerton, S.B. (1983) Welding techniques simplify joining of dissimilar metals. *Fabricator*, **3**, 1, 18 – 19.
7. Price, I.G. (1981) Electron beam welding — industrial applications. *Metal Construction*, **10**, 612 – 618.
8. Perdue, R.J., Birne, J.V. (1975) The use of high-voltage electron beam welding machines for production applications in the UK. In: *Proc. of the Int. Conf. on Exploiting Welding in Production Technology*, Cambridge, Apr. 22 – 24. Abington: TWI.
9. Dowse, M. (1970) Latest development in EBW. *Welding and Metal Fabrication*, **3**, 96 – 104.
10. Anderl, P., Koy, J., Scheffels, W. (1987) Outstanding features and controls for industrial electron beam welding applications. In: *Proc. of the Conf. on The Laser vs. the Electron Beam*, USA. Bakish Materials Corp. Englewood: NJ07631.
11. Vovk, V.N., Surin, F.E. (1973) Technology of manufacturing band saws of high-speed steel. *Mashinostroitel*, **3**, 31 – 34.
12. Geller, Yu.A. (1983) *Tool steels*. Moscow: Metallurgia.
13. Nazarenko, O.K., Kajdalov, A.A., Kovbasenko, S.N. *et al.* (1987) *Electron beam welding*. Ed. by B.E. Paton. Kyiv: Naukova Dumka.

PRESSURE WELDING OF INTERMETALLIC ALLOY γ-TiAl

A.N. YUSHTIN, V.N. ZAMKOV, V.K. SABOKAR, P.N. CHVERTKO and **I.K. PETRICHENKO**
The E.O. Paton Electric Welding Institute, NASU, Kyiv, Ukraine

ABSTRACT

Pressure welding of intermetallic alloy γ-TiAl with and without interlayers was studied. It is shown that interlayers of aluminium and titanium fail to provide joints with properties close to those of the base metal. The technology is suggested for welding without an interlayer by heating generated by the electric current flow and plastic deformation at a rate of up to 2 mm/s. Metal of the welded joints made by this technology has strength equal to that of the base metal.

Key words: *pressure welding, intermetallic alloy, interlayer, lamellar structure, γ-phase, α_2-phase*

Investigation of weldability and development of technological processes of welding of heat-resistant alloys on an intermetallic base, such as γ-TiAl, are the topical problem. These alloys are characterized by superior high-temperature strength (at 700 – 750 °C), high heat resistance and relatively low density (3.8 g/cm^3) [1, 2]. These properties make the above alloys promising for commercial application in the engine construction industry. Main causes of a limited application of γ-TiAl alloys in aircraft and car engines are their extremely low ductility at room temperature and difficulties associated with technological processing. Authors of [3] think that fusion welding of titanium aluminide can be done only by using preheating to a temperature of 300 – 470 °C. Otherwise the welded joints will have cracks. γ-TiAl alloys can also be joined by diffusion bonding [4]. Subjecting the samples for a long tome (3 h) to pressure within a temperature range of 1000 – 1100 °C and subsequent heat treatment at 1430 °C (0.5 h) resulted in defect-free welded joints in titanium aluminide [4]. However, strength characteristics of these welded joints were substantially inferior to those of the base metal.

Investigations of pressure welding of γ-TiAl, the results of which are given in this article, were aimed at simplification and acceleration of the process, as well as at improvement of quality of the welded joints.

The possibility of welding titanium aluminide with and without a «soft» interlayer (aluminium, titanium) was investigated. It was assumed that subjecting the workpieces with an interlayer to annealing after welding would lead to its dissolution in the base metal and to diffusion homogenizing of chemical composition in the joining zone. Therefore, aluminium and titanium, i.e. the main alloying elements of titanium aluminide alloy, were selected as the interlayer materials. Samples of titanium aluminide (diameter and height — 20 mm) cut out from the ingot subjected to isostatic treatment at a temperature of 1260 °C and pressure of 170 MPa for 4 h with subsequent stabilization annealing at 1000 °C for 50 h were used for the experiments. The content of alloying elements and impurities in the alloy was as follows, wt.% (at.%): Ti — 60.947 (49.24); Al — 31.152 (44.7); Nb — 4.65; Mn — 2.73; B — 0.31; Fe — 0.015; C — 0.026; O — 0.08; N — 0.02; H — 0.05. Welding of the samples was performed using the P-115 machine providing their radiation heating to a temperature of 900 °C and application of a compression load of up to 500 kN. The machine was additionally equipped with a device for heating the samples by the electric current flow.

After the manufacture (machining), the samples to be welded were subjected to X-ray and fluorescent inspection to reveal internal and external cracks. Prior to welding the mating surfaces were polished and etched in a concentrated hydrofluoric acid. Parameters used for welding the samples are given in Table 1.

Microstructure of welded joints made using an aluminium foil as the interlayer (sample 1) is shown in Figure 1. In the as-welded condition the joining zone consists of three layers with clearly defined interfaces between them (Figure 1, *a*). Two layers are located along the line of contact with the base metal and the third layer is a central part of the joint. The latter contains a large number of defects in the form of microdiscontinuities and transverse cracks. It should be noted that the length of a crack is limited by the width of this region. Results of investigations of chemical composition of the joining zone using X-ray microanalysis showed that in the regions adjoining the base metal the concentration of aluminium

Table 1. Parameters of welding the samples

Sample No.	*Interlayer material*	*Temperature, °C*	*Pressure, MPa*	*Holding time, min*
1	Aluminium (foil, 0.15 mm)	750	0 100	10 15
2	Titanium (foil, 0.2 mm)	830	0 300	15 15
3	Without interlayer	850	0 300	15 20

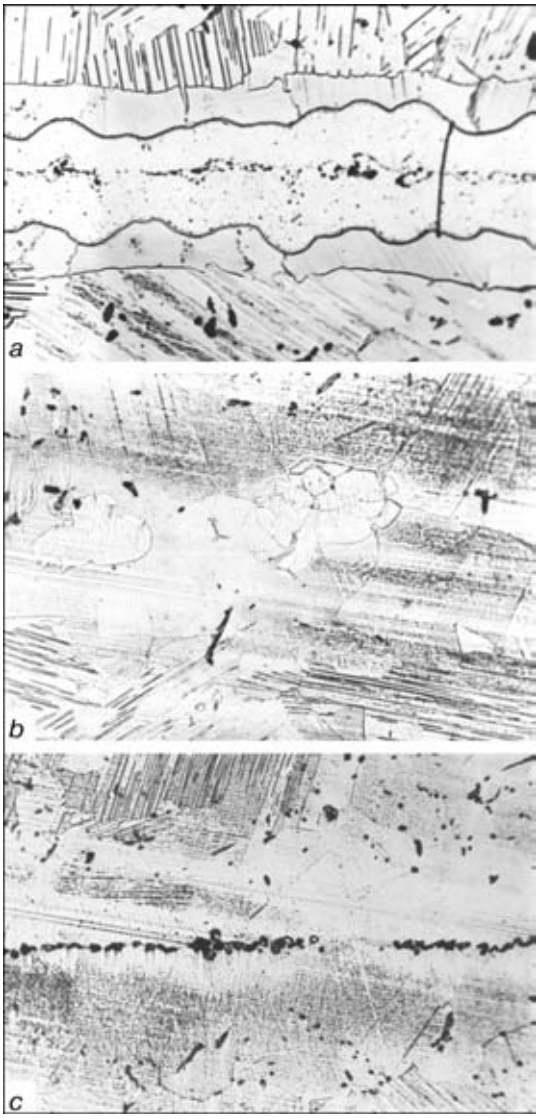

Figure 1. Microstructure of a welded joint in alloy γ-TiAl with an aluminium interlayer in as-welded condition (*a*) (×400), after welding and annealing (*b*) (×200) and microporosity along the line of contact in the sample after annealing (*c*) (×200) (reduced by 4/5)

decreased (as compared with the alloy) to 40.5 at.% (27.05 wt.%) and that of titanium increased to 57.26 at.% (67.89 wt.%). At the same time, the concentration of niobium decreased very insignificantly (4.2 wt.%). The data obtained suggested the following:

- phase composition of metal in these regions of the joining zone is similar (according to the constitutional diagram of Ti–Al [5]) to phase composition of the $(\gamma + \alpha_2)$ alloy, but the content of the γ-phase in it is much lower;
- it is likely that metal in these regions of the joining zone remained in a solid state during the entire welding process. Otherwise a considerable heterogeneity in distribution of niobium would be fixed.

The content of aluminium is 74 at.% (62 wt.%) and that of titanium is 25 at.% (37. 3 wt.%) in the central part of the joint. This ratio of the above elements is very close to stoichiometric composition of the $TiAl_3$ intermetallic alloy [6]. It should be noted that here the niobium content is almost twice as low as that of the alloy.

The difference in thermal expansion coefficients of metal in regions with the $(\gamma + \alpha_2)$ and TiAl crystalline structures causes development of tensile stresses (during cooling) in the central zone of the joint, which probably leads to formation of transverse cracks in this zone.

As it can be seen from Table 1, welding in this case was performed at a temperature in excess of the melting point of the aluminium interlayer. Therefore, the detected «laminar» structure of the joining zone, in which the layers differ from each other in the content of alloying elements and phase composition, is a result of interaction of molten aluminium with the solid base metal. An important role in formation of this structure in particular is played by pressure that compresses the samples during welding. Drips of aluminium were fixed on the side surfaces of the samples welded. Therefore, after wetting the samples with molten aluminium the melt seemed to be pressed out from the gap, and only a characteristic layer of liquid was left on the mating surfaces.

As the alloy welded is the two-phase one and has a laminar structure, both $\alpha_2(Ti_3Al)$- and γ(TiAl)-phases are in contact with liquid aluminium. According to the constitutional diagram of the Ti–Al system the diffusion enrichment of the γ(TiAl)-phase with aluminium (from the melt) should lead to its pereutectic decomposition following such a reaction:

$$TiAl_s + 2Al_l = TiAl_{3s} \qquad (1)$$

with subsequent transition of $TiAl_3$ into the melt. Diffusion of aluminium into $\alpha_2(Ti_3Al)$-phase can cause only the pereutectoid reaction

$$Ti_3Al_s + 2Al_l = 3TiAl_s. \qquad (2)$$

And only the formation of TiAl allows it to further interact with aluminium by reaction (1) and transfer (in the form of $TiAl_3$) into the melt.

Therefore, it can be suggested that the above reactions should result in a decrease in the γ-phase in regions of the base metal in contact with molten aluminium of the interlayer and, thus, a decrease in the aluminium content. In turn, formation of the $TiAl_3$-phase and its transition into the melt favour the formation of a single-phase ($TiAl_3$) region at the centre of the welded joint.

The samples were subjected to vacuum annealing at a temperature of 1260 °C for 10 h to decrease heterogeneity formed during welding and homogenize chemical and phase composition in the joining zone. This treatment resulted in a drastic change in microstructure of the joining zone. It became more homogeneous, interfaces between regions vanished and recrystallization processes took place in it (Figure 1, *b*). Only the character of defects did not change (Figure 1, *c*). X-ray microanalysis showed that annealing did cause a substantial decrease in chemical heterogeneity across the section of the welded joint.

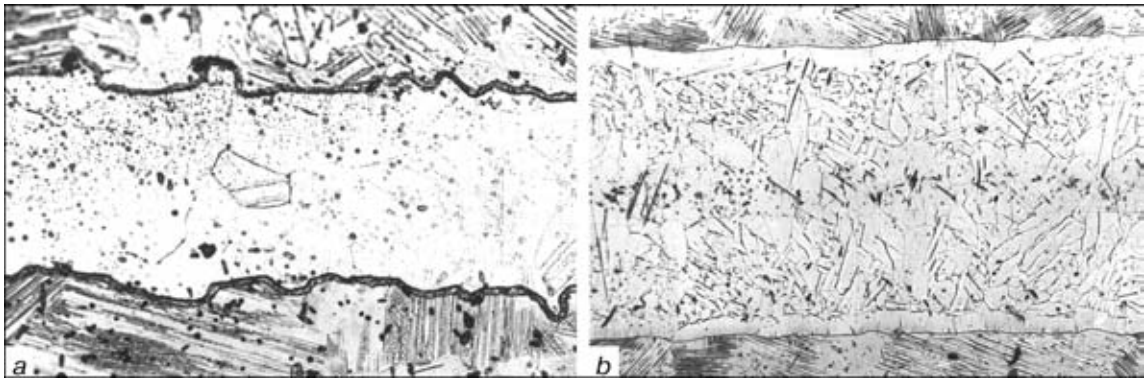

Figure 2. Microstructure of a γ-TiAl welded joint with a titanium interlayer in as-welded condition (*a*) (×250) (reduced by 4/5) and after welding and annealing (*b*) (×100) (reduced by 3/4)

It was established that in the joining zone (region 100 μm wide was investigated) the content of aluminium was 49.93 at.% (34.5 wt.%), the content of titanium was 47.108 at.% (58.3 wt.%) and that of niobium was 2.08 at.% (4.91 wt.%). It is likely that complete homogenizing of the concentration of alloying elements can be achieved by selecting the optimal technology parameters, such as thickness of the aluminium interlayer, time of annealing, etc. As to the phase composition, the results obtained suggest that the entire joining zone consists of the $(\gamma + \alpha_2)$-phases. The amount of the γ-phase here is somewhat higher than its content in the base metal. However, because of high density of defects in the joining zone, despite similarity of chemical and phase compositions as a result of annealing, the samples still fractured during machining. This prevented not only mechanical properties of the joints to be evaluated, but also the tensile test specimens to be made.

Microstructure of welded joints made with the titanium foil used as the interlayer is shown in Figure 2. In the as-welded condition (Figure 2, *a*) the relatively wide and clearly defined interfaces without visible defects were detected between the base metal and interlayer. X-ray microanalysis showed that at the interface between the base metal and the interlayer there occurred a dramatic decrease in the concentration of aluminium (from 32 – 33 wt.% in the alloy to zero in the interlayer) and a corresponding increase in the titanium content — up to 100 wt.%. Therefore, under the selected welding conditions (sample 2) the diffusion processes did not receive any significant development. Chemical composition of the interlayer and the adjoining regions of the base metal underwent no marked changes. It can be supposed (and this is proved by the character of the concentration curves) that the thickened interfaces between the base metal and interlayer are the $\alpha_2(Ti_3Al)$-phase.

Vacuum annealing at 1260 °C for 5 h resulted in an increase in width of the joining zone almost to 500 μm (Figure 2, *b*). Percentage of titanium and aluminium in it corresponds to their content in the α_2-phase. An insignificant decrease in the concentration of niobium and manganese detected in this zone

Table 2. Mechanical properties of welded joints (at 20 °C)

Sample No.	*Interlayer material*	*Annealing conditions*	*Tensile strength, MPa**	*Fracture location*
1	Aluminium (foil, 0.2 mm)	As-welded	0	Samples fractured in turning
		1260 °C, 10 h		
2	Titanium (foil, 0.2 mm)	As-welded	283	In welded joint
			500	In base metal
			450	Same
		1260 °C, 5 h	129	In welded joint
			188	
			305	
3	Without interlayer	As-welded	0	Samples fractured in turning
		1260 °C, 5 h	128	In welded joint
			147	
			130	
4	Same	As welded	541 (470)**	In base metal
			518 (436)	
			523 (452)	
		1260 °C, 5 h	514 (393)	Same
			507 (382)	
			510 (380)	

*Diameter of gauge length of the sample — 3 mm. **Numbers in brackets are the yield strength values.

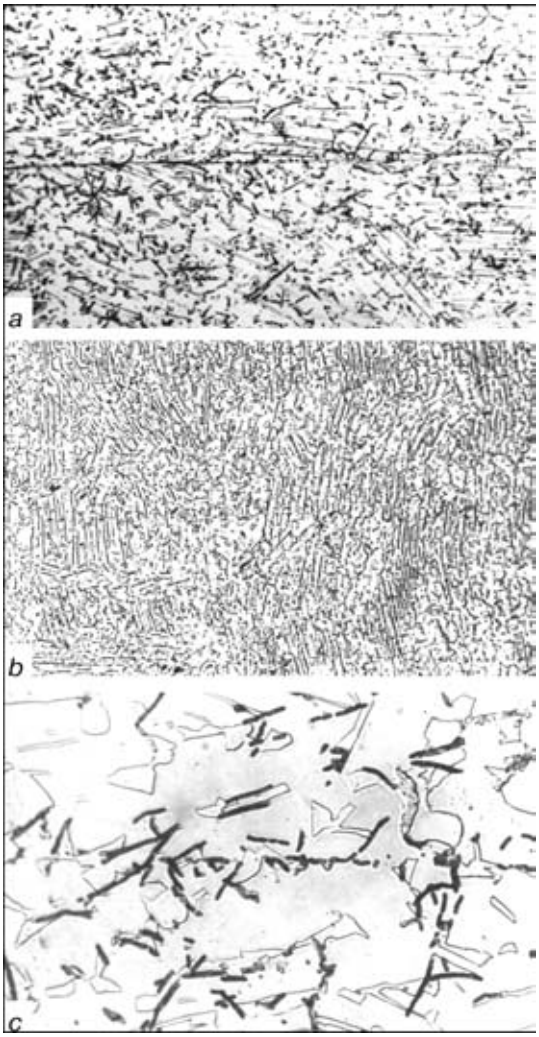

Figure 3. Microstructure of a γ-TiAl welded joint (sample 3) in as-welded condition (*a*) (×200), after welding and annealing (*b*) (×100) and the same (*c*) (×1000) (reduced by 4/5)

is indicative of the fact that its formation results from diffusion of titanium from the interlayer into the base metal. This allows a conclusion that it is unreasonable to increase the time of annealing, as diffusion of aluminium is required for transformation of part of the γ-phase in the joining zone into the α_2-phase and formation of the two-phase ($\gamma + \alpha_2$)-structure, identical to that of the base metal. However, despite structural and chemical heterogeneity of the welded joint made using the titanium interlayer, the absence of defects in the joining zone allowed the specimens for evaluation of static strength to be made.

The test results showed that in the as-welded condition the joint had a sufficiently high value of tensile strength, while some of the specimens had strength equal to that of the base metal (Table 2). In this case this seems to be caused by contact strengthening [7] of the titanium interlayer, since after annealing all the specimens fractured in the joint. Their strength is close to that of the α-phase based alloys [8, 9].

Therefore, it was established that welding of the γ-TiAl based alloys using aluminium and titanium foils as the interlayers failed to ensure the required quality of the joints. In the case of the aluminium interlayer the joints (after welding and annealing) have chemical and phase composition close to that of the base metal. But performance of these joints is inadequate because of defects (cracks and microporosity) formed during welding. In the case of the titanium foil the welded joints both in the as-welded condition and after welding and annealing have a certain level of strength at normal temperature. However, it turned out impossible to provide heat resistance of such joints close to that of the γ-TiAl alloy, because the joining zone had a single-phase structure — $\alpha_2(Ti_3Al)$. Therefore, further investigations were aimed at development of the technology for direct welding of the γ-TiAl alloy.

As it is given in Table 1 (sample 3) welding of γ-TiAl was performed at 850 °C. The samples were heated to this temperature, held for 15 min and then pressure was applied to them. Investigation of microstructure of the joints in the as-welded condition (Figure 3, *a*) showed a clearly defined interface in contact of the surfaces joined. No formation of common grains (at the given welding parameters) was detected. In some samples both individual micropores and their chains were revealed along the line of contact. The presence of such defects, in addition to the characteristic interface between the surfaces joined, is caused

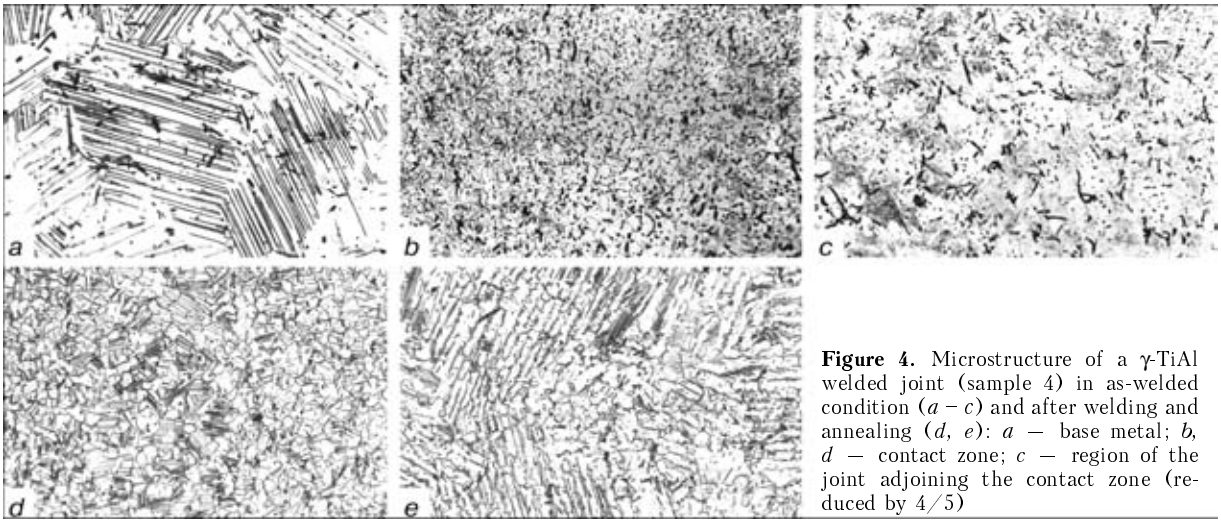

Figure 4. Microstructure of a γ-TiAl welded joint (sample 4) in as-welded condition (*a* – *c*) and after welding and annealing (*d*, *e*): *a* — base metal; *b*, *d* — contact zone; *c* — region of the joint adjoining the contact zone (reduced by 4/5)

probably by an extremely low strength of the joints in the as-welded condition (Table 2).

Vacuum annealing of the samples welded favoured a substantial change in structure of the metal within the contact zone (Figure 3, *b*). Recrystallization processes and formation of common grains along the line of contact resulted in disappearance of the interface between the surfaces joined. Individual lineage precipitates (Figure 3, *c*) can be revealed along the line of contact only at large magnification. At the same time, these structural transformations in the joining zone had an insignificant effect on mechanical properties of the joints (see Table 2). The results obtained and data of [4] proved the known assumption [10] that the clearly defined interface, its presence or absence depend upon the degree of local plastic deformation in the contact zone during the welding process. In this connection, further experiments on direct welding of the γ-TiAl alloy were conducted using the same machine, but heating of the samples was done by the electric current flow (j = 20 A/mm^2). In this case a constant compression load of 3 kN was applied to the samples before heating. This method of welding made it possible to localize plastic deformation within the contact zone and ensure (at the preset parameters) the deformation rate of about 2 mm/s.

Microstructure of the welded joints made by the above method is shown in Figure 4. In the as-welded condition a complete transformation of the lamellar ($\gamma + \alpha_2$)-structure of the base metal into the fibrous-type one (Figure 4, *b*), against the background of which the individual fine recrystallized grains are seen, was fixed within the contact zone and the adjoining regions. With distance from the plane of contact the character of the microstructure persists, but its elements are increased in size (Figure 4, *c*). It should be noted that metal in this region has a higher microhardness than the base metal (Figure 5).

Short-time annealing of the samples welded (1.5 h) at a temperature of 1260 °C favoured recrystallization of the fibrous structure to form fine equiaxed recrystallized grains. Besides, directly in the contact zone they are larger in size than in the zone adjoining it (Figure 4, *d*). The recrystallized grains have a lamellar ($\gamma + \alpha_2$)-structure. The lamellar microstructure with a substantially changed shape of the lamellae was detected between the recrystallized region adjoining the contact zone and the base metal (Figure 4, *e*).

Investigations showed that welded joints with such a structure had strength equal to that of the base metal both in the as-welded condition and after welding and annealing. Moreover, during the process of static tensile tests the yield strength was registered in the diagrams (see Table 2).

It was of interest to determine strength of metal directly in the joining zone. For this an annular notch 0.2 mm deep was made in the contact zone in the gauge length of some of the test specimens (cut out from welded joints in the as-welded condition). These

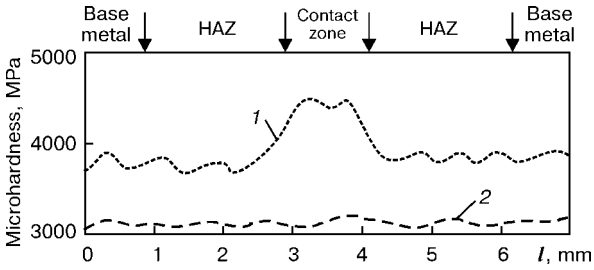

Figure 5. Variation in microstructure across the section of the welded joint (sample 4): *1* — in as-welded condition; *2* — after welding and heat treatment; *l* — distance

specimens, like specimens with a smooth gauge length, fractured in the base metal (at a distance from the notch). Tensile strength was (average over three specimens) 514 MPa. Stresses in the joining zone of specimens during testing were 684 MPa, i.e. they were in excess of tensile strength of the base metal.

CONCLUSIONS

1. The process of welding of γ-TiAl using an aluminium interlayer results in the formation of defects in the form of microporosity and cracks in the contact zone, and despite similar chemical and phase composition of the joining zone and base metal (after welding and annealing) such joints have an extremely low strength.

2. The use of a titanium interlayer for welding makes it possible to produce the defect-free joints characterized by a high strength (in the as-welded condition). Annealing after welding does not help eliminate chemical and phase heterogeneity in the welding zone and makes such joints unsuitable for operation under high-temperature conditions.

3. The method and parameters for direct (without interlayers) pressure welding are suggested. They provide the defect-free welded joints in the γ-TiAl alloy, having strength equal to that of the base metal both in the as-welded condition and after welding and annealing.

REFERENCES

1. Altunin, Yu.F., Glazunov, S.G. (1961) *Binary titanium and aluminium alloys*. Moscow: Oborongiz.
2. Dimiduk, D.M. (1995) Gamma titanium aluminides — an emerging materials technology. In: *Proc. of Annual Meeting TMS'95 on Gamma Titanium Aluminides*, Las Vegas.
3. Patterson, E.A. *et al*. (1990) Titanium aluminide: electron beam weldability. *Welding J*., **1**, 39 – 44.
4. Cam, G., Bohm, K.-H., Kocak, M. (1999) Diffusionschweißen feingegoßener Titanaluminid. *Schweißen und Schneiden*, **8**, 470 – 475.
5. (1992) *Ordered intermetallics — physical metallurgy and mechanical behaviour*. Kluwer: Academic Publ.
6. Hong, T., Watson-Young, T.J., Guo, X.Q. *et al*. (1991) Crystal structure, phase stability and electronic structure of Ti_3Al intermetallics: Ti_3Al. *Phys. Rev. B*., **3**, 1940 – 1947.
7. Karakozov, E.S. (1986) *Pressure welding of metals*. Moscow: Mashinostroyeniye.
8. Kornilov, I.I., Nartova, T.T., Andreev, O.N. (1974) Structure and properties of Ti_3Al titanium aluminide and some alloys on its base. In: *Structure, properties and application of intermetallics*. Moscow: Nauka.
9. Imaev, R.M., Gabidulin, N.G., Salishchev, G.A. (1992) Effect of deformation temperature on mechanical properties and microstructure of intermetallic Ti_3Al. *Metally*, **6**, 73 – 79.
10. Gelman, A.S. (1970) *Principles of pressure welding*. Moscow: Mashinostroyeniye.

PULSE-PLASMA HARDENING OF TOOLS

Yu.N. TYURIN[1], **O.V. KOLISNICHENKO**[1] and **N.G. TSYGANKOV**[2]
[1]The E.O. Paton Electric Welding Institute, NASU, Kyiv, Ukraine
[2]Open Stock-Holding Company «Cherepovets Steel-Rolling Plant», Cherepovets, Russia

ABSTRACT

The resource-saving technology has been developed for pulse-plasma hardening of tools. The technology is characterized by low consumption of alloying elements and electric power and high productivity (up to 0.5 m^2/h). It allows hardening (heating) of only the working (cutting) surfaces, which leads to an increase in wear resistance without any change in structural state of a workpiece as a whole. Power consumption of the machine is 10 kW.

Key words: *surface hardening, alloying, pulse plasma, technology, equipment, metal cutting tools, dies, blanking dies, calculation, efficiency, experimental studies*

Treatment of surfaces by concentrated energy sources (laser, electron beam, plasma, etc.) is extensively used in machine building for hardening of tools [1 – 6]. It provides unique mechanical and physical properties of surfaces of parts (high hardness, wear resistance, fatigue strength, corrosion resistance, etc.)

Concentrated energy sources cause rapid heating (time of heating — $1 \cdot 10^{-3} - 1 \cdot 10^{-6}$ s) of the surface layer of metal followed by its intensive cooling through removal of heat both into the bulk of metal and into the environment. High rates of heating and cooling of the surface layer of metal ($1 \cdot 10^4 - 1 \cdot 10^8$ K/s) lead to formation of a dispersed crystalline structure, high density of dislocations and variations in the carbon and nitrogen concentrations [7, 8].

Thermal effect exerted by the concentrated energy sources is combined with alloying processes. Surfaces of parts are alloyed by melting of the preliminarily heated coatings [9, 10] or by adding gaseous alloying elements, such as nitrogen, hydrocarbon gases, cyanides, into the working medium (plasma) [11 – 13]. As shown by investigations [4 – 13], the pulsed action on the workpiece surface is most efficient. This is attributable to increased heating and cooling rates, elasto-plastic deformation of the surface and, thus, intensification of the diffusion mechanisms [7].

An increase in the diffusion coefficients at a high-rate elasto-plastic deformation, $\varepsilon = \frac{\Delta h/h}{\tau} \geq 20$ s^{-1} (where $\Delta h/h$ is the degree of deformation and τ is the time of deformation) is caused by an increase in the mean concentration of vacancies, which is in excess of the equilibrium one [14]. Investigation results given in [15] show that at a high-rate plastic deformation of crystalline bodies the rate of migration of atoms in them is higher than the rate of a diffusion transfer of elements into liquid metal. In the hard pin impact affected zone on the sample surface (time of deformation $\tau = 4 \cdot 10^{-3}$ s, degree of deformation — 10 % and temperature in the contact zone — 800 °C) the diffusion coefficient ($D = 8.3 \cdot 10^{-3}$ cm^2/s) is higher by two orders of magnitude than in liquid metal [15]. High-rate deformation in the pulsed magnetic field also causes an increase in mass transfer [16, 17].

As shown by the data given in [14, 18], at any pulsed treatment of the workpiece surface the mass transfer coefficient increases and hardly depends upon the grain size. The mass transfer coefficient monotonously decreases with an increase in the number of pulses. The most interesting fact is that the simultaneous effect on the surface by different methods of pulse treatment leads to a substantial increase in mass transfer, which is of a synergic character.

The E.O. Paton Electric Welding Institute developed the technology for pulse-plasma treatment of materials, which allows different methods of affecting the workpiece surface, such as elasto-plastic deformation, effect by sound and pulsed magnetic field, heat and electric-pulse treatment and deformation of metals and alloys during the process of reversible ($\alpha \leftrightarrow \leftrightarrow \gamma$) transformations, to be simultaneously implemented.

Formation of pulse-plasma jets. Non-stationary detonation conditions of combustion of fuel gas mixtures were used for formation of the high-power plasma jets.

Energy parameters of the non-stationary detonation combustion products (pulse-plasma jet) can be determined by solving the known two-dimensional non-stationary problem of propagation of the detonation wave in the electric field between two co-axial electrodes. To derive a numerical solution, the problem was simplified, and the mean values of temperature, velocity, pressure and density of the combustion products along the axis of the electrodes were determined without allowance for their variations across the section [19, 20].

The result of the solution is a program for calculation of the combustion chamber for a pulse plasmatron (Figure 1). The plasmatron consists of detonation chamber *1*, where the fuel gas mixture is formed and its detonation combustion is initiated, central electrode-anode *2*, conical electrode-cathode *3*, inter-elec-

trode gap *4*, consumable electrode *5* and power supply *6*.

At initiation of the detonation the ionized combustion products are fed from detonation chamber *1* to inter-electrode gap *4*, thus completing the electric circuit. This leads to formation of conducting layer *7* of the combustion products, which is accelerated under the effect of gas-dynamic and electromagnetic forces. Consumable metal rod *5* is fixed in a position along the axis of central electrode *2*. The end of the rod is evaporated during heating and thus provides introduction of alloying elements into the plasma jet.

Being ejected from the plasmatron, plasma jet *8* completes the circuit between the anode electrode and the workpiece surface (cathode *9*). As a result of the current flowing through the jet the plasma is heated due to Joulean heat ($Q = \sigma E^2$, W/m^3).

Energy characteristics of the plasma jets at the exit from the plasmatron, calculated from theoretical formulae [19, 20], have a linear dependence upon the electric field intensity E and inter-electrode length l (Figure 2). At l = 200 mm and E = 400 kV/m the plasma jet can have temperature of 15,000 K and velocity of 5 km/s.

Experimental evaluation of characteristics of the plasma jet was carried out using an industrial plasmatron with an inter-electrode gap 200 mm long. The time-averaged temperature of the plasma jet was determined by the results of spectral analysis of the jet. The temperature of the plasma was determined by a relative intensity of iron lines. Plasma radiation spectra integrated by time showed that temperature of the plasma at the plasmatron exit was 15,000 – 20,000 K.

Investigations of scans of the plasma jets make it possible to reveal in them abrupt changes or jumps in density and periodical structure (Figure 3). Measurements of the initial diameter of the jet (diameter of the generator nozzle) and distance to the first density jump allow the velocity of the jet to be calculated. It can be seen from the Figure that in fact the first jump consists of two jumps, which is attributable to non-uniformity of the plasma jet consisting of jets with different velocities. Velocity of the jet, v, is estimated from the following formula [21]:

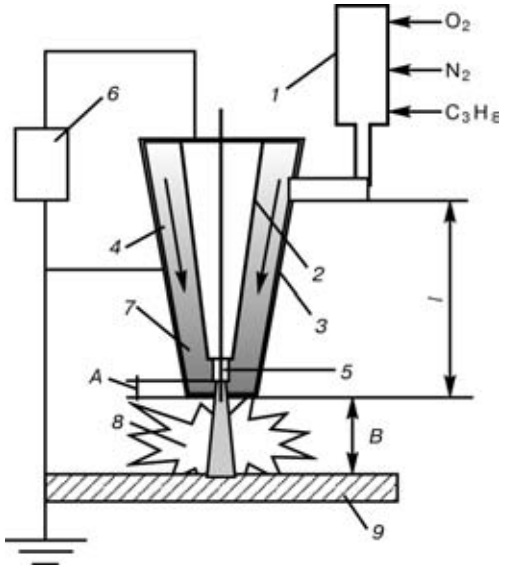

Figure 1. Schematic of plasmatron for pulse-plasma treatment (designations *1 – 9* are given in the text); A — distance from the exit section of the nozzle to the evaporated electrode tip, B — distance to workpiece

$$L_w = 1.3 d_a \sqrt{M^2 - 1}. \quad (1)$$

Re-write formula (1) as follows:

$$v = \sqrt{\left(1 + \frac{L_w}{1.3 d_a}\right)^2} a_0, \quad (2)$$

where d_a = 0.027 m is the plasmatron nozzle diameter; $M = v/a_0$ is the Mach number; L_w = 70 and 90 mm is the wave length of the periodical structure, the photo of which was made by high-speed filming (Figure 3). Sound velocity a_0 is determined from the formula:

$$a_0 = \sqrt{\gamma RT}, \quad (3)$$

where γ = 1.3 is the adiabatic constant; R = = 300 J/(kg·K) is the gas constant; T = 15,000 K is the jet temperature.

Substituting expression (3) into formula (2) yields v_1 = 5.4 km/s and v_2 = 6.7 km/s, which is in agreement with theoretical data.

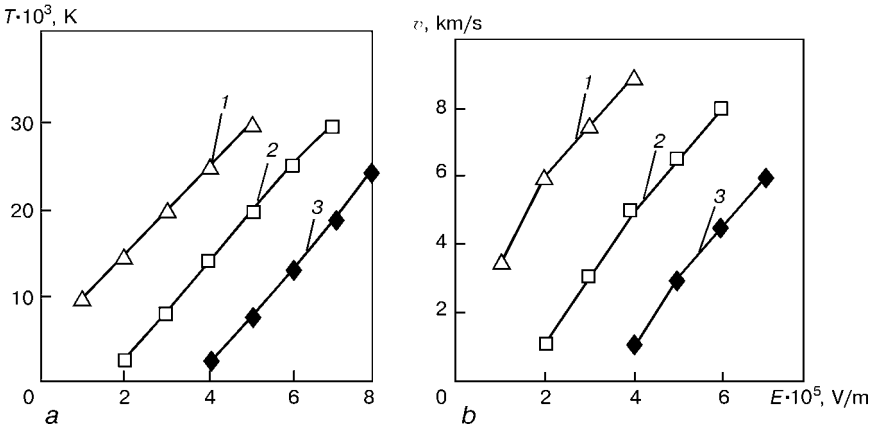

Figure 2. Temperature T (*a*) and velocity v (*b*) of the pulse plasma depending upon the electric field intensity E in the inter-electrode gap and its length l: *1* — 300; *2* — 200; *3* — 100 mm

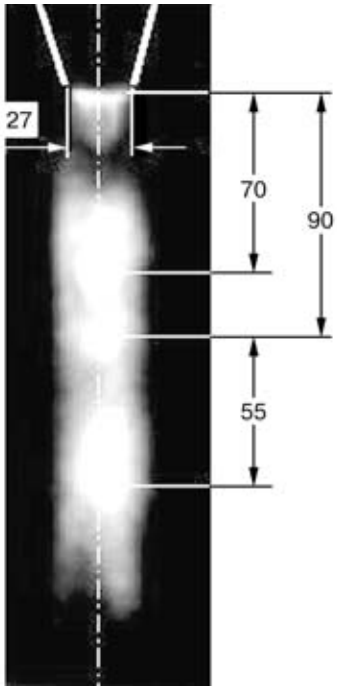

Figure 3. Free-flowing plasma jet emitted from the plasmatron nozzle

Structure of the plasma jet shown in Figure 3 is characteristic of a supersonic mode with the under-expanded flow of the jet and corresponds to the detonation character of operation of the plasmatron, at which pressure in the chamber can be much in excess of the atmospheric one. The pattern of interaction of the plasma jet with a barrier is characterized by the presence of jet *1* and region *2* of the shock-compressed layer (SCL), which is a rather typical case (Figure 4) [22].

After break-down of SCL the electric current will flow along the plasma jet from the central electrode in the plasmatron to the workpiece surface (Figure 4). Density of the electric current in the plasma jet, j, is $(1 - 7)\cdot 10^3$ A/cm^2 and temperature T is 15,000 – 30,000 K. The heat flow into a workpiece depends upon the current density and varies within a range of $q = (0.1 - 5.0)\cdot 10^6$ W/cm^2. Evaluation of heat flows was done on the basis of theoretical analysis of the non-stationary equation of thermal conductivity

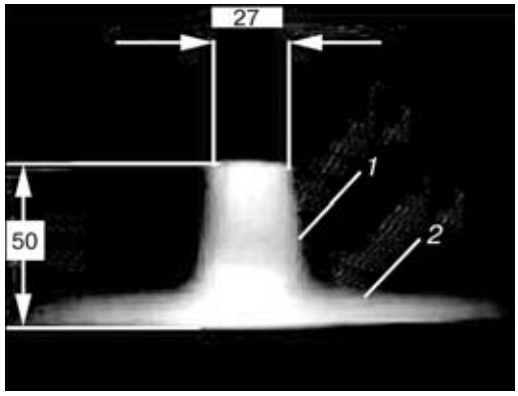

Figure 4. Plasma jet running on a flat barrier (designations *1* and *2* are given in the text)

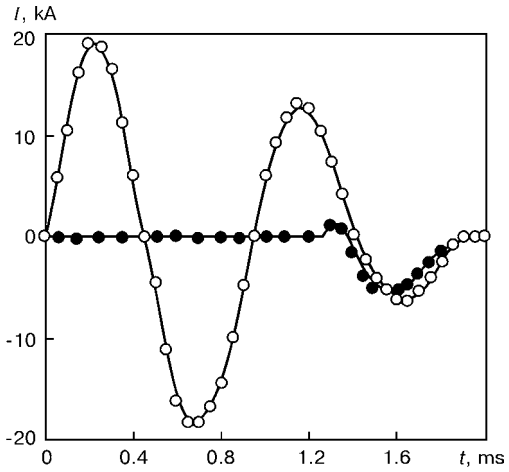

Figure 5. Variations in the electric current depending upon the time of its flowing in the inter-electrode gap (○) and between the central electrode and a workpiece (●)

through thickness of the hardened layers of steels of the martensitic grade [23].

The time of interaction of the plasma pulse and its energy parameters were controlled by varying capacitance C of the capacitors, voltage U_{ch} at plates of the capacitor bank, inductance L in the discharge circuit, distance B to the workpiece surface and variation in size of the active spot of interaction of the plasma jet with the workpiece surface.

Experiments were conducted to measure the time variations of the electric current in the inter-electrode gap, and current between the central electrode and workpiece surface using the Rogovsky belt by the method described in [24].

Figure 5 shows variations in the current in formation of the plasma pulse and its interaction with the workpiece surface. The experiment was performed under the following conditions: C = 1000 μF, U_{ch} = = 3500 V, B = 70 mm and $L = 3\cdot 10^{-5}$ H. Analysis of the time distribution of the currents shows that SCL formed at the plasma jet flowing onto the workpiece surface has a much higher electrical resistance than resistance of the discharge gap between the co-axial electrodes. As shown by measurements, break-down of SCL occurs only after 1.2 ms. This time is enough for re-charging of the capacitors, and consumable electrode *5* (Figure 1) will be a cathode for 0.2 ms and then again will become the anode for 0.4 – 0.6 ms.

The experiments indicated that at the initial moment the workpiece surface is in elasto-plastic interaction with a shock wave and the pulsed plasma jet. Then, at break-down of SCL the surface is affected by the electric current (amplitude value of the current is 5 kA). This results in a formation of the pulsed magnetic field with an intensity of up to $1.6\cdot 10^5$ A/m. Further on (within 3 – 5 ms) the surface will be affected by the flows of the combustion and electrode erosion products.

Results of plasma–workpiece surface interaction. As indicated by the experiments and shown by the calculation data, treatment of the workpiece surface by the pulsed plasma containing alloying ele-

ments is accompanied by a complex (thermal, electromagnetic and deformation) pulsed effect. This provides alloying of the workpiece surface with components of the plasma and hardening of this surface. Alloying elements are added into the plasma in the form of metal electrode (rod) erosion products and gas (propane, nitrogen).

Pulse-plasma treatment of a workpiece of Fe-based alloy results in the formation of a microcrystalline alloyed layer (Figure 6). Structure of the layer depends upon the plasma composition and quantity of the treatment pulses. Composition of the plasma is determined by a oxidizer to fuel ratio. In a general case of combustion of hydrocarbons C_nH_m in nitrogen-oxygen mixtures the left part of the reaction equation has the following form [25]:

$$C_nH_m + \alpha\left(n + \frac{m}{4}\right)O_2 + \left(n + \frac{m}{4}\right)\left(\frac{100}{X} - 1\right)N_2,$$

where X is the oxygen content of the nitrogen-oxygen mixture and α is the excess oxidizer coefficient.

Oxide inclusions (Figure 6, *b*) were fixed in the layer after treatment by the plasma with an increased oxygen content ($\alpha > 1$), while at $\alpha < 0.8$ no such inclusions were detected (Figure 6, *a*). The hardened layer is thicker and more uniform after multiple (5 pulses) pulse-plasma treatment (Figure 6, *c*).

The highest value of microharness of the hardened layer on samples of steel U-8 (C — 0.74 – 0.85; Mn — 0.2 – 0.4; Si — 0.15 – 0.35; Cr — up to 0.2 wt.%), which were preliminarily subjected to quenching and high tempering, was achieved in the case of using tungsten and molybdenum electrodes (Figure 7). Treatment was performed without surface melting, specific power of the jet was $1 \cdot 10^6$ W/cm^2. Microhardness was measured on transverse sections using the PMT-3 hardness meter. The Knoop diamond pyramid was used for the measurements. The load on the pyramid was 1 N.

X-ray phase analysis of the pulse-plasma hardened layers on samples of carbon steels detects widening of the α-Fe lines and emergence of the residual austenite lines. An increase in the number of pulses favours further widening of the α-Fe lines with a decrease in their intensity, as well as an increase in the relative intensity of the γ-Fe lines. Comparison of the intensities of the residual austenite and ferrite lines shows that the amount of austenite under the same treatment conditions is maximum in the case of using a tungsten electrode. X-ray spectrometry indicated that the consumable electrode material penetrated into the hardened layer on a workpiece. For example, in the case of using a titanium consumable electrode titanium was detected at a depth of down to 20 μm in the hardened layer [26].

Determination of mass transfer of light elements was done by the Auger-spectroscopy methods. Samples were made from tool steel 9KhS (C — 0.93; Si — 1.4; Cr — 1.1; Ni — 0.35; Mn — 0.4; S — 0.03; P — 0.03 wt.%). Distribution of the concentration of nitrogen through thickness of the layer (Figure 8) was investigated using the LAS-2000 unit on oblique sections at an angle of 8° to the surface*. Results of measurements were averaged by polynomial in the 5th power by finding on a computer a minimum of the efficiency function (standard deviation) in the Mathcad 7 Professional environment.

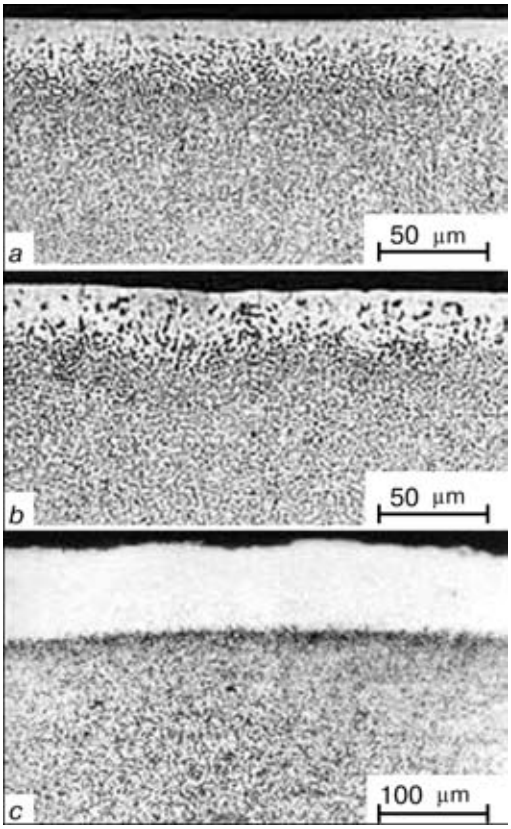

Figure 6. Hardened layer on the surface of a sample of iron alloy (0.8 % C): *a*, *b* — 1 treatment pulse; *c* — 5 treatment pulses; *b* — plasma with excessive amount of oxygen

The experiments showed that after affecting the surface with 30 plasma pulses (τ = 0.6 ms) the con-

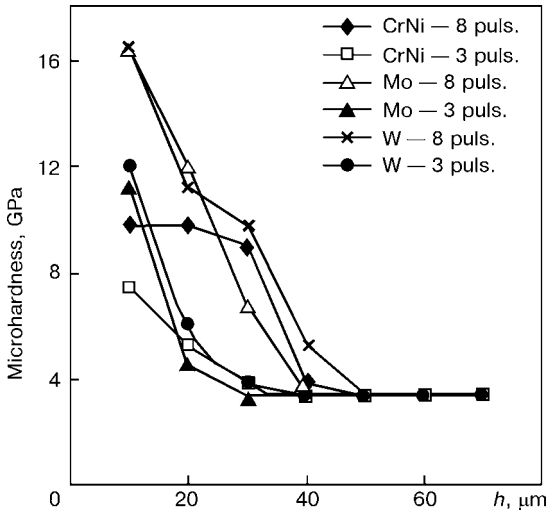

Figure 7. Distribution of microhardness in the hardened layer of a sample of iron alloy (0.8 % C) after pulse-plasma treatment using different electrodes; h — layer thickness

* Investigations were carried out by O.D. Smiyan.

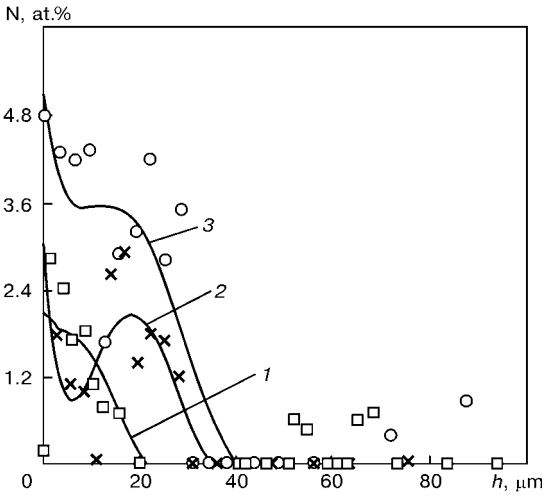

Figure 8. Distribution of nitrogen through thickness of the layer depending upon the number of plasma pulses: *1* — 10; *2* — 20; *3* — 30 pulses

centration of nitrogen at a depth of 20 μm was up to 3.2 at.% (Figure 8). Similar distribution of the concentrations of elements can be achieved in the case of thermal diffusion if the mass transfer coefficient is $1 \cdot 10^{-4} - 1 \cdot 10^{-5}$ cm^2/s.

Experience of application of the technology. Maximum microhardness of the surface layer was obtained in treatment by the plasma containing tungsten or molybdenum vapours and at excessive nitrogen and carbon content of the plasma. In addition to the above process parameters, the level of microhardness is affected also by the quantity of the plasma pulses. An increase in their number leads to an increase in thickness of the hardened layer and its uniformity.

High values of service properties of alloys used for the manufacture of tools are provided by alloying them with tungsten, molybdenum and vanadium. The chromium content of alloys is 3.0 – 4.5 %.

Dies for hot deformation of machine parts are made from alloys 4KhV2S (C — 0.35 – 0.44; Mn — 0.2 – 0.4; Si — 0.6 – 0.9; Cr — 1.0 – 1.3; W — 2.0 – 2.5 wt.%), 3Kh2V8F (C — 0.3 – 0.4; Mn — 0.2 – 0.4; Si — ≤ 0.35; Cr — 2.2 – 2.7; W — 7.5 – 9.0 wt.%) and alloys with 12 – 18 % W. Molybdenum is the element that provides an efficient improvement in properties of alloys. It increases toughness causing no decrease in heat resistance and increases erosion resistance. Molybdenum alloys (5 – 6 % Mo) are very sensitive to decarburization. Therefore, for their surface alloying it is necessary to use, in addition to the consumable molybdenum electrode, also the plasma gas in the form of a mixture with an excess oxidizer coefficient ($\alpha < 0.7$).

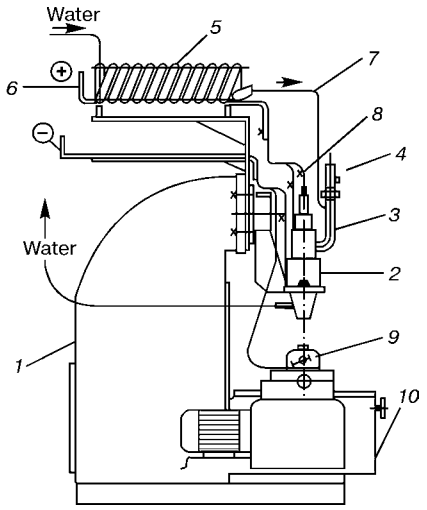

Figure 9. Schematic of the pulse-plasma unit (designations *1 – 10* are given in the text)

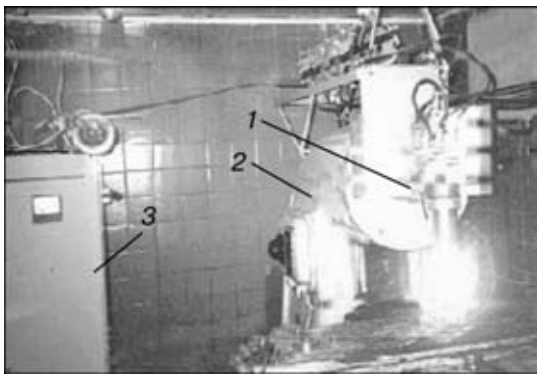

Figure 10. Unit for pulse-plasma treatment of tools (designations *1 – 3* are given in the text)

Pulse-plasma treatment of parts of high-speed alloys of the R6M5 (C — 0.82 – 0.88; Cr — 3.8 – 4.4; W — 5.5 – 6.5; Mo — 5.0 – 5.5; V — 1.7 – 2.1 wt.%) and R12F4K5 (C — 1.25 – 1.35; Cr — 3.5 – 4.0; W — 12.5 – 14.0; Mo — ≤ 1.0; V — 3.2 – 3.8; Co — 5.0 – 6.0 wt.%) grades should be performed without surface melting. Under such treatment conditions the performance of tools increases 3 – 5 times [6, 8, 9, 27]. Thus, in pulse-laser treatment [9] an increase in hardness of the surface and wear resistance of the tool of high-speed steel is achieved only in the case where specific power of pulses is $1 \cdot 10^5 < W_p < 5 \cdot 10^5$ W/cm^2 and the time of treatment is $\tau = 5 \cdot 10^{-3}$ s. These treatment conditions provide the ultimate surface temperature which is close to the melting point.

Pulse-plasma hardening of the tools at the Open Stock-Holding Company «Cherepovets Steel-Rolling Plant» is done using an upgraded milling machine tool (Figure 9). Pulse plasmatron *2* is used instead of vertical spindle *1* of the machine tool. The plasmatron has a built-in detonation gun *3* with chamber *4* for gas mixing and initiation of detonation. The electric current is fed to the plasmatron through inductor *5* via copper busbar *6*. The plasmatron and inductor are cooled by water which is fed to the plasmatron through the inductor via duct *7*. Alloying elements are added along the axis of the plasmatron in the form of rod *8* and through chamber *4* in the form of gas. The tool is fixes in device *9* and its movement is provided from machine tool drive *10*.

Equipment for pulse-plasma hardening (Figure 10) is installed in a special room which has double noise-proof doors and a watch hole. The equipment comprises plasmatron *1*, standard workpiece manipulator *2* and power supply *3*. The room is equipped

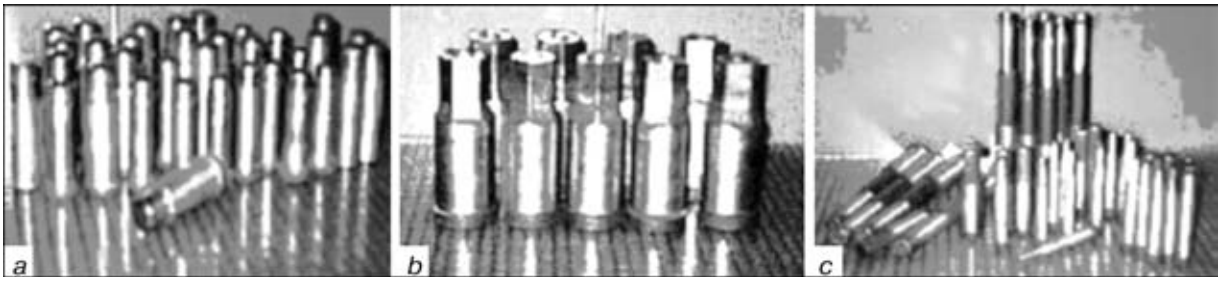

Figure 11. Punches hardened by pulse-plasma treatment: *a* — pushing punches; *b* — punches for hot deformation of nuts; *c* — hole punches

with electromagnetic radiation and noise protection systems. As a rule, these are the known typical designs. Electromagnetic stop valves are installed in gas ducts and a flow relay is mounted on the water duct. The unit is remotedly controlled from the panel which is located outside the room.

Metal cutting tools, dies and punches for hot and cold deformation of metal were subjected to hardening. Prior to hardening, the parts were subjected to standard heat treatment and machining. Pulse-plasma treatment was used as a final operation. Hardening was done only to surfaces of cutting edges of the tools (Figure 11). Productivity of hardening was up to 0.5 m^2/h, which in re-calculation to actual tools amounts up to 100 punches per hour. The tool surface requires no cleaning or any other preparatory operation for hardening.

Unlike metal cutting tools of high-speed steels, die tools permit surface melting [27, 28]. The process parameters for different types of punches, dies and moulds were selected so that they have a minimum power density, sufficient for surface heating to melting. Such conditions provided alloying of the molten surface of a part with elements contained in the plasma jet. The consumable tungsten electrode was used for hardening, the plasma gas contained excess propane ($\alpha = 0.7$). Treatment was performed with a three-fold effect by the pulsed plasma on the surface being hardened. For hardening of metal cutting tools (taps, threading dies, broaches) the power density was selected so that it was insufficient for melting and blunting of cutting edges. The consumable molybdenum electrodes were used and the plasma gas contained excess propane and nitrogen ($\alpha = 0.6$). Mills, drills, cutters, etc. were treated using a titanium electrode by a 5 – 10-fold effect by the plasma on the surface being hardened.

The technology and technological equipment for pulse-plasma hardening of tools are employed under conditions of metalware production and mass metallurgical production at the Cherepovets Steel-Rolling Plant. The experience of commercial application showed that performance of the tools increased 2 – 6 times.

CONCLUSIONS

1. The offered pulse-plasma technology is a resource-saving one, which is provided by a low consumption of alloying elements and electric power in combination with high productivity (up to 0.5 m^2/h).

2. The technology makes it possible to treat (heat) only working (cutting) surfaces, which solves the problem of increasing wear resistance without any change in structural state of the entire workpiece.

3. Treatment of surfaces of tools by the pulsed plasma containing alloying elements is accompanied by electromagnetic (up to $N = 1.6 \cdot 10^5$ A/m) and thermal (up to $q = 5 \cdot 10^6$ W/cm^2) effects. This accelerates mass transfer of elements from the plasma deep into the surface being hardened.

4. Commercial application of the pulse-plasma technology proves its efficiency.

REFERENCES

1. Guriev, V.A., Tesker, V.I. (1996) Application of laser treatment for formation of a surface layer on normalized steel with high tribological and tough properties. *Fizika i Khimiya Obrab. Materialov*, **1**, 14 – 19.
2. Safonov, A.N. (1997) Basic areas of efficient application of laser technology for heat treatment of alloys. *Materialovedeniye i Term. Obrab. Metallov*, **7**, 2 – 6.
3. Leshchinsky, L.K., Samotugin, S.S., Pirch, I.I. (1990) *Plasma surface hardening*. Kyiv: Tekhnika.
4. Gusev, O.A., Lazarenko, A.V., Ivanov, B.A. *et al*. (1984) Application of pulsed electron beam for heat treatment of metals. *Materialovedeniye i Term. Obrab. Metallov*, **9**, 13 – 16.
5. Lebedev, V.K., Kaleko, D.M. (1998) Pulse-arc heat treatment of metal surfaces. *Ibid*., **6**, 8 – 12.
6. Bojko, V.I., Valyaev, A.N., Pogrebnyak, A.D. (1999) Modification of metal materials by pulsed high-power particles beams. *Uspekhi Fiz. Nauk*, **11**, 1 – 29.
7. Anastasiadi, G.P. (1992) *Formation of chemical microheterogeneity in casting alloys*. S.-Peterburg: Politekhnika.
8. Grigoryants, A.G., Safonov, A.N. (1987) *Methods for surface laser treatment*. Moscow: Vysshaya Shkola.
9. Kovalenko, V.S., Golovko, L.F., Chernenko, V.S. (1990) *Hardening and alloying of machine parts by laser beam*. Kyiv: Tekhnika.
10. Cordier, R.C., Crampon, J., Foct, J. (1998) Surface alloying of iron by laser melting: microstructure and mechanical properties. *Surface Eng*., **5**, 381 – 385.
11. Eskin, S., Zahavi, J. (1993) *Lazers Eng*., **2**, 181 – 190.
12. Rykalin, N.N., Uglov, A.A., Kokora, A.N. (1975) *Laser treatment of materials*. Moscow: Mashinostroyeniye.
13. Voloshin, M.N., Gasin, D.A., Korableva, I.R. *et al*. (1993) Variation in structure of armco-iron in pulse nitrogen-plasma treatment. *Fizika i Khimiya Obrab. Materialov*, **1**, 67 – 70.
14. Larikov, L.N., Falchenko, V.M., Mazanko, V.F. (1975) Abnormal acceleration of diffusion in pulse loading. *Doklady AN SSSR*, **5**, 1073.
15. Larikov, L.N., Mazanko, V.F., Nemoshkalenko, V.V. *et al*. (1981) Investigation of abnormal mass transfer under conditions of impact loading of dissimilar metals. *Fizika i Khimiya Obrab. Materialov*, **4**, 20 – 26.
16. Gertsriken, D.S., Skripnichenko, A.L., Tishkevich, V.M. *et al*. (1987) Effect of pulse magnetic field and tensile stresses on mobility of nickel and copper atoms. *Vestsi AN BSSR*, **4**, 31 – 34.

17. Gertsriken, D.S., Kostyuchenko, V.G., Tishkevich, V.M. *et al*. (1997) Effect of plastic deformation in pulsed magnetic field on migration of atoms in metals. *Doklady NAN Ukrainy*, **3**, 47 – 50.
18. Gertsriken, D.S., Mazanko, V.F., Falchenko, V.M. (1991) *Pulse treatment and mass transfer in metals at low temperatures*. Kyiv: Naukova Dumka.
19. Tyurin, Yu.N. (1999) Improvement of equipment and technologies for detonation coating. *Avtomaticheskaya Svarka*, **5**, 13 – 18.
20. Yushchenko, K.A., Borisov, Yu.S., Tyurin, Yu.N. (1994) Theory and practice of plasma-detonation modification of surfaces of machine parts and tools. *Svarochnoye Proizvodstvo*, **5**, 23 – 25.
21. Bai Shi-i. (1960) *Theory of jets*. Moscow: Fizmatgiz.
22. Sultanov, M.A. (1981) *Shock-compressed plasma in high-power pulse discharges*. Dushanbe: Donish.
23. Lykov, A.M., Pochepaev, V.G., Redkin, Yu.G. *et al*. (1997) Plasma heat treatment of steels. *Fizika i Khimiya Obrab. Materialov*, **3**, 27 – 32.
24. Lebedev, A.D., Uryukov, B.A. (1990) *Pulse accelerators of high-pressure plasma*. Novosibirsk: Institute of Thermal Physics of the USSR Academy of Sciences.
25. Petrov, S.V., Karp, I.N. (1993) *Plasma air-gas spraying*. Kyiv: Naukova Dumka.
26. Mordovets, N.M., Borisov, Yu.S., Rachek, A.P. *et al*. (1994) *Structure, crystalline texture and microhardness in the subsurface layer of carbon steel modified by the plasma-detonation method*. Kyiv: Naukova Dumka.
27. Grigoryants, A.G., Safonov, A.N., Ivashov, G.P. *et al*. (1987) Investigation of pulse laser quenching of die fixture. *Kuznechno-shtamp. Proizvodstvo*, **12**, 22 – 23.
28. Burakov, V.V., Fedoseenko, S.S. (1983) Formation of structure of increased wear resistance in laser quenching of metal working tools. *Materialovedeniye i Term. Obrab. Metallov*, **5**, 36 – 40.

TECHNOLOGIES FOR PRODUCTION AND PROPERTIES OF POWDERS OF THE Al–Cu–Fe SYSTEM FOR THERMAL SPRAYING OF COATINGS WITH QUASICRYSTALLINE STRUCTURE

Yu.S. BORISOV, M.T. PANKO, L.I. ADEEVA, V.L. RUPCHEV and **V.G. BOBRIK**
The E.O. Paton Electric Welding Institute, NASU, Kyiv, Ukraine

ABSTRACT

Effect of the technology for production of powders of the Al–Cu–Fe system on their structure, phase composition, physical and technological properties was investigated. The effect of annealing of the spray powders on their content of the quasicrystalline ψ-phase was established.

Key words: *powders, quasicrystalline phase, structure, properties of powders, thermal spraying*

The first paper [1] dedicated to discovery of quasicrystals characterized by the symmetry axis of the fifth order (before that it was considered prohibited for crystals according to the classical crystallography laws) was published in 1984.

There are more than a hundred of alloys in which the presence of the quasicrystalline phase was detected, the majority of them are Al-base alloys [2 – 4]. This class of materials, taking a position between amorphous and crystalline alloys, has a very interesting combination of physical properties. For example, quasicrystalline ψ-phases in alloys of the Al–Cu–Fe system are characterized by high values of microhardness (HV 6 – 10 GPa), ability of elastic restoration ($H/E > 0.08$) [5], specific electrical resistance (78 – 105 μOhm·m [6]), corrosion [7] and wear resistance. In addition, they feature low thermal conductivity of 1 – 2 W/(m·K) [8] and friction coefficient [9].

Formation of quasicrystals and quasicrystalline phases in solidification of alloys occurs under conditions of super rapid cooling at rates of $10^4 – 10^6$ °C/s. This level of the cooling rates is observed during thermal spraying (TS), which makes it possible to produce coatings containing quasicrystalline phases in their structure.

Based on peculiarities of the technology of TS of such coatings, the Al–Cu–Fe alloys, having the following composition, at.%: Fe — 8 – 13; Cu — 17 – 25; Al — 65 – 70, hold the highest promise.

Quality, structure and properties of thermal spray coatings greatly depend upon such characteristics of the spray powders as phase and chemical composition, and shape and size of particles [10]. In addition, the last two characteristics should provide the stable and controlable feed of the particles to a high-temperature gas jet, which determines the productivity of the spraying process.

Characteristics of powders depend upon the technology used for their production. With rare exceptions [11], almost no information on investigation into the effect of characteristics of the initial powders produced by different technologies on structure and properties of thermal spray coatings is available in the literature. This paper describes the work done to fill out this gap.

Three types of powders (Table 1) were made to investigate the effect of the technology for producing powders from alloy of the Al–Cu–Fe system on their structure, physical and technological properties. The first two were produced by high-pressure water (type *A*) and compressed air (type *B*) atomization of the melt. Powder of type *C* was produced by the method of spontaneous decomposition of the jet and water cooling of droplets, followed by drying and crushing of the granules. Calculation of composition of the charge in all cases was made on the basis of composition of the $Al_{63}Cu_{25}Fe_{12}$ alloy, in which the quasicrystalline phase had the highest thermodynamic stability [12]. Allowing for the probability of partial evaporation of aluminium during TS and in the process of manufacture of the powders, the actual content of

Table 1. Parameters of different technologies for manufacture of powders of $Al_{63}Cu_{25}Fe_{12}$ alloy

Powder type	*Production method*	*Cooling rate of droplets, °C/s*	*Energy supply*	*Atomization pressure, MPa*
A	High-pressure water atomization	$0.5 – 5 \cdot 10^4$	Water	9
B	Compressed air atomization	$0.5 – 5 \cdot 10^3$	Air	5
C	Spontaneous decomposition of the jet, mechanical crushing	< 100		

Table 2. Granulometic composition of powders

Particle size, μm	*Content, wt.%*		
	Type A	*Type B*	*Type C*
> 315	–	3	2
315 – 200	6	15	5
200 – 160	5	18	10
160 – 100	21	17	8
100 – 80	23	18	10
80 – 50	20	17	13
< 50	23	12	52

aluminium in the alloy was increased by 2 wt.%, as compared with the calculated one.

Aluminium (99.95 %), copper (99.90 %) and iron (99.70 %) were used as the raw materials.

The melt was produced by induction melting of the charge in a graphite crucible in the air atmosphere with a homogenizing holding at a temperature of 1100 ± 30 °C for 15 min. In this case the melt was considerably overheated (by 180 – 240 °C higher than the melting point), which, according to [13], stabilized the ψ-phase and led to its predominance in structure of the cooled powder particles. Isothermal holding promotes averaging of chemical composition and enhances stabilization. After removal of slag from the surface and mechanical mixing, the melt was fed to the metal collector and then, through a discharge opening with a diameter of 9 mm, to the crushing zone of the atomization chamber.

Different atomizers, calculated and designed according to the recommendations [14], were used for atomization of the Al–Cu–Fe system melt by high-pressure water and compressed air. In the first case the crushing diagram used was that done by individual water jets arranged along the ring around a free flow of the melt. The powder thus produced (type *A*) was subjected to drying at a temperature of 200 °C for 4 h followed by classification into fractions.

In the second case an atomizer with an annular gas nozzle was used. The melt was fed to the gas flow through a discharge opening which, at the same time, served as the «central body» of the annular gas nozzle. The powder produced (type *B*) was classified into fractions without preliminary drying.

Powder of type *C* was produced by feeding of the melt through a circular opening. In this case, according to the Rayleigh law [15], under the effect of small disturbances the cylindrical flow decomposed into individual fragments which were then formed into droplets under the effect of surface tension. Cooled in water, they had an irregular shape and size of about 10 – 15 mm. After drying at a temperature of 200 °C for 4 h the particles thus produced were subjected to mechanical crushing to a size of less than 3 mm and grinding in a ball mill for 30 min to a size of less than 350 μm.

Powders of type C_1 were produced from the melt at a temperature of 1100 ± 30 °C without isothermal holding to investigate the effect of homogenizing holding on phase composition.

Granulometric composition of the powders of alloy of the Al–Cu–Fe system is given in Table 2.

Phase and structure of the powders were investigated by metallography, microdurometry, chemical and X-ray phase analysis and X-ray microanalysis.

Metallography of polished samples after electrochemical etching in a reagent (1 l of 20 % aqueous solution of chromic acid, 20 ml of hydrofluoric acid and 15 ml of sulphuric acid) was done using optical microscope NEOPHOT-32.

Microhardness of structural components of the powders was determined using the LECO instrument M-400 under a load of 0.245 and 0.490 N for 10 s.

X-ray phase analysis was conducted using the DRON-UM1 diffractometer in a monochromatized copper radiation Cu_{K_α} within a range of angles from 15 to 163°. The amount of the ψ-phase was determined by the procedure described in [16].

Chemical composition of the powders was determined by standard methods and that of structural components — using the JSM-840 scanning microscope with an X-ray attachment. This device was also used for photography of the appearance of the powders.

The oxygen content of the alloy was estimated using the RO-316 gas analyser by the method of reduction melting in a nitrogen flow.

The unit the principle of operation of which is based on the use of the thermal balance equation was employed to determine heat content. The test samples were made by two methods: pressing of the high-pressure water atomized powder with particles 80 – 50 μm in size under a pressure of $1.47 \cdot 10^5$ N and sintering of the charge materials in an inert gas at a temperature of 680 °C for 3 h.

Investigation of appearance of the powders showed that types *A* and *B* had certain similarity in structure of their particles. Particles with a size of over 100 μm had a very comlex structure and irregular shape, and were characterized by a substantial porosity (Figure 1, *a, d*). With a decrease in particle size, the powders became of a simpler shape and contained less pores (Figure 1, *b, e*). Particles of the smallest size (less than 50 μm) were characterized by a spherical or spindle-like shape and the lowest porosity (Figure 1, *c, f*).

Metallography of structure of the atomized particles in an unetched state (Figure 2, *a*) showed the presence of open and closed pores from 1 to 10 μm in size. Etching revealed the two-phase structure of the particles, consisting of finely dispersed precipitates against the background of the light matrix (Figure 2, *b*).

According to the data of X-ray phase analysis, the atomized powders have a two-phase (ψ + β)-structure, where the quasicrystalline ψ($Al_{63}Cu_{25}Fe_{12}$)-phase is

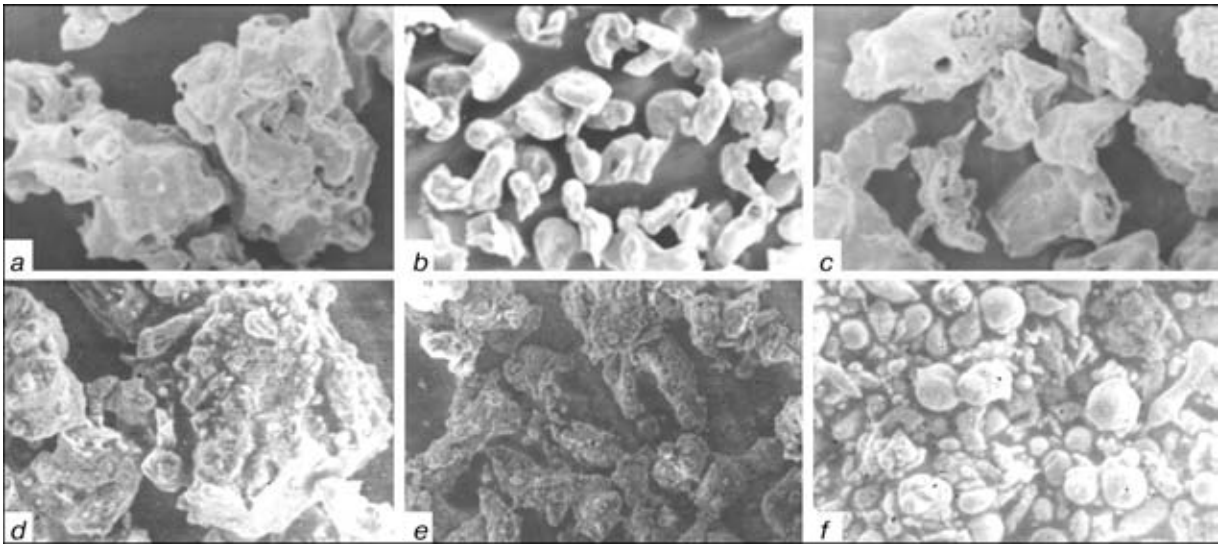

Figure 1. Appearance of powders of types *A* (*a* – *c*) and *B* (*d* – *f*) with particle sizes of 160 – 100 (*a, d*), 100 – 80 (*b, e*) and less than 50 μm (*c, f*) (×200) (reduced by 1/2)

dominant (Table 3). It is contained in the crystalline β($Al_{55}Cu_{40}Fe_5$)-matrix in the form of finely dispersed precipitates. High cooling rates during the atomization process lead to chemical heterogeneity of the atomized particles. Both phases, cubic β and icosahedral ψ, are close to each other in chemical composition, but substantially different in crystalline structure. Mass fraction of the quasicrystalline phase in powders of types *A* and *B* is 69 – 74 and 50 – 54 wt.%, respectively.

Microhardness of the powders is in direct dependence upon the amount of the ψ-phase. For powders of types *A* and *B* it equals 5.3 – 7.4 and 4.5 – 6.7 GPa, respectively. Content of oxygen in powders of type *A* is 1.35 – 1.95 and in powders of type *B* — 0.38 – 1.50 wt.%, respectively.

Particles of the crushed powders (type *C* and C_1) have an irregular fragmentation shape and faces with typical brittle fracture fragments (cleavages) (Figure 3, *a*). A dendritic structure of cast granules of the alloy can be seen on surfaces of some of them (Figure 3, *b*).

Microstructure of powder of type C_1 was studied on granules of the alloy before crushing. They had a cast dendritic multi-phase structure consisting of particles of acicular and regular geometrical shapes (position *1* in Figure 3, *c*), i.e. crystalline λ($Al_{72}Cu_5Fe_{23}$)-phase with microhardness of 6.3 – 8.4 GPa. Light spherical grains and rosettes with flinely dispersed precipitates (position *2* in Figure 3, *c*) are the two-phase (ψ + β) structural component with microhardness of 5.9 – 7.0 GPa. Fine grains and interlayers of the θ(Al_2Cu)-phase (position *3* in Figure 3, *c*) with microhardness of 2.5 – 2.8 GPa are seen along the boundaries of the spherical grains.

Powders of type C_1, according to the data of X-ray phase analysis, contain β-, ψ-, λ- and θ-phases, powders of type *C* contain no θ-phase. These powders differ from types *A* and B not only in their multi-phase nature, but also in the presence of the crystalline β-phase dominating in their structure. In powders of type *C* the content of the quasicrystalline ψ-phase is much higher (43 %, as compared with 22 – 30 wt.% in powders of type C_1). In addition, these powders are more homogeneous. Therefore, it can be concluded that homogenizing holding at a temperature of 1100 ± 30 °C yields positive results.

Content of oxygen in the crushed powders (types *C* and C_1) is not in excess of 0.91 wt.%.

Technological properties of the powders (flowability, apparent density) determined according to GOST 20899–75 and 19440–74 are given in Table 3. Apparent density of powders of type *A* and *B* increases with a decrease in size of the particles and depends upon their shape and internal porosity. For powders of types *A* and *B* with particles not less than 50 μm

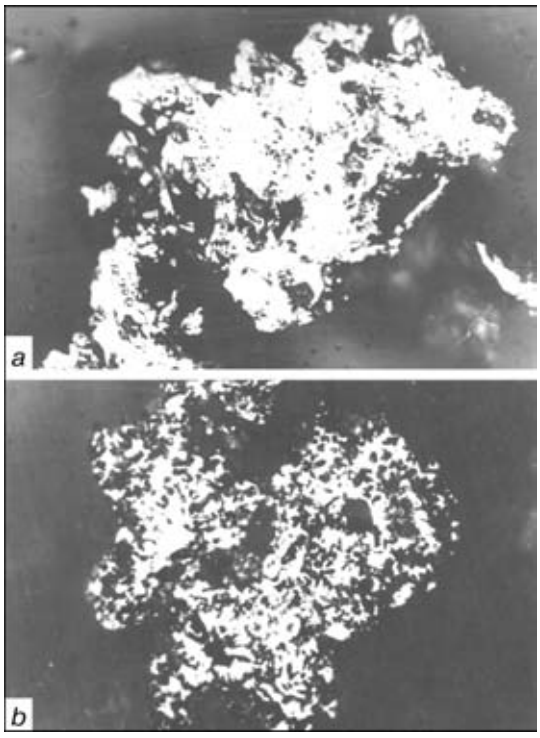

Figure 2. Microstructure of particles of powders of type *A* without etching (*a*) and type *B* after etching (*b*) (×500) (reduced by 2/3)

Table 3. Characteristics of the investigated powders

Particle size, μm	*Content of elements, wt.%*				*Phase composition*	*Content of ψ-phase, wt.%*	*Flowability, s/50 g*	*Apparent density, g/cm³*
	Al	*Cu*	*Fe*	[O]				
				Type A				
125 – 100	42.12	38.50	18.70	1.60	ψ, β	74	*	*
100 – 80	41.20	39.40	17.87	1.35		73	80	1.20
80 – 50	41.62	39.50	18.98	1.75		69	81	1.40
< 50	41.50	39.10	18.98	1.95		69	78	1.72
				Type B				
160 – 100	40.50	37.90	19.50	0.63	ψ, β	*	*	*
100 – 80	39.20	37.90	19.00	0.38		50	65	1.50
80 – 50	*	*	*	*		52	58	1.65
< 50	*	*	*	1.50		54	80	1.88
				Type C				
160 – 20	39.70	37.60	18.60	0.65	β, ψ, λ	43	No	1.60
				Type C_1				
160 – 100	48.00	34.50	17.50	0.91	β, ψ, λ, θ	22	No	*
100 – 80	*	*	*	0.73		30		*
80 – 50	*	*	*	*		22		*
< 50	*	*	*	0.77		29		1.50

Note: * – not studied

in size it is 1.72 and 1.88 g/cm³, respectively. Powders of types *C* and C_1 have apparent density of 1.5 – 1.6 g/cm³, and, unlike powders of types *A* and *B*, they feature no flowability.

Additive specific heat of the $Al_{63}Cu_{25}Fe_{12}$ alloy is 624 J/(kg·K). Experimental values of specific heat of the pressed samples are 508 J/(kg·K) and those of the sintered samples – 585 J/(kg·K).

Comparison of the atomized and crushed powders proves the former to be advantageous. The atomized powders contain a larger amount of the quasicrystalline phase (up to 74 wt.%) and are characterized by a higher phase and chemical homogeneity, as compared with the crushed powders. This is caused by different rates of cooling of the powder particles from the melt.

The content of the quasicrystalline phase is in direct dependence upon the cooling rate. It is maximum in powders of type *A* cooled at the highest rates $(0.5 – 5.0)\cdot10^4$ °C/s.

As it is known from [11, 16], the content of the quasicrystalline phase in powders can be increased also by homogenizing annealing at a temperature of 700 °C for several hours. Powders of all types with particles 100 – 80 μm in size were annealed in vacuum at a temperature of 700 °C for 2 h. As a result of annealing the ψ-phase content of powders of types *A* and *B* increased from 70 and 50, respectively, to 100 wt.%. Structure of the powders became single-phase (quasicrystalline).

Annealing of powders of type *C* leads to an increase in the mass fraction of the ψ-phase from 43 to 62 wt.%, and annealing of powders of type C_1 causes an increase in the mass fraction of the phase from 22 to 53 wt.%. In this case their structure is tranformed from multiphase to the two-phase one, consisting of the ψ- and β-phases. Attempts to achieve complete homogenization failed. Nevertheless, annealing is an efficient method which allows the quasicrystalline phase content of the TS powders to be substantially increased.

Initial powders determine to a substantial degree the quality, structure and properties of the sprayed coatings [11, 16]. Thus, there is a direct relationship between the amount of the quasicrystalline phase in powders and coatings. Powders of a spherical shape, which are more homogeneous in chemical composition, promote formation of more homogeneous low-porosity coatings. Powders produced by water and gas atomization differ substabtially from those produced by crushing of ingots not only in the shape of the particles but also in that the latter inherit a large-scale chemical heterogeneity. It causes acceleration of the oxidation and corrosion processes, especially in regions of formation of a galvanic couple.

On the other hand, the unfavourable morphology of a powder leads to an increase in porosity of coatings, which causes decrease in their resistance to wear and thermal cyclic fatigue.

In thermal spraying of powders of the Al–Cu–Fe system the basic cause of a decrease in the quasicrystalline phase content can be the loss of a low-melting point component, i.e. aluminium, as a result of its selective evaporation or oxidation in a high-temperature jet. Thus, as it is known from [17], the crystalline

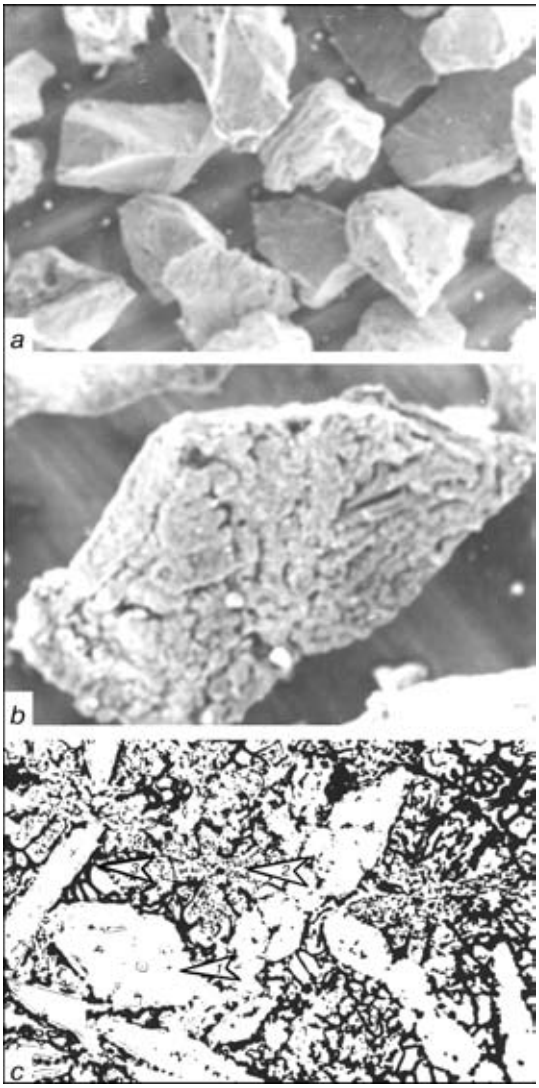

Figure 3. Appearance (*a*, *b*) (×200 and ×350, respectively) and microstructure after etching of powders of type C_1 (*c*) (×400) (reduced by 2/3); see designations in the text

β-phase is dominating in structure of the coatings, in which the mass content of aluminium was decreased by 8 wt.%. Therefore, for the formation of thermal spray quasicrystalline coatings it is necessary to try to decrease the thermal factor, e.g. by increasing the input of the kinetic energy of the spray particles through using the high-velocity TS methods (supersonic plasma, detonation).

Behaviour of the powders was investigated under the effect of the plasma jet during air-gas plasma spraying (AGPS) and supersonic air-gas plasma spraying (SAGPS). Particles of powder of type *B* not more than 50 μm in size and with the ψ-phase content of 54 wt.% (Table 3) were trapped by water in AGPS and SAGPS. Size of the initial powder particles (more than 25 μm) was selected according to the recommendations [16] because of selective evaporation of aluminium. It was found that particles trapped by water had a melted surface (Figure 4), but in their shape they were similar to the initial powder particles (see Figure 1, *b*). The amount of the quasicrystalline phase decreased insignificantly and was 49 and 50 wt.% in

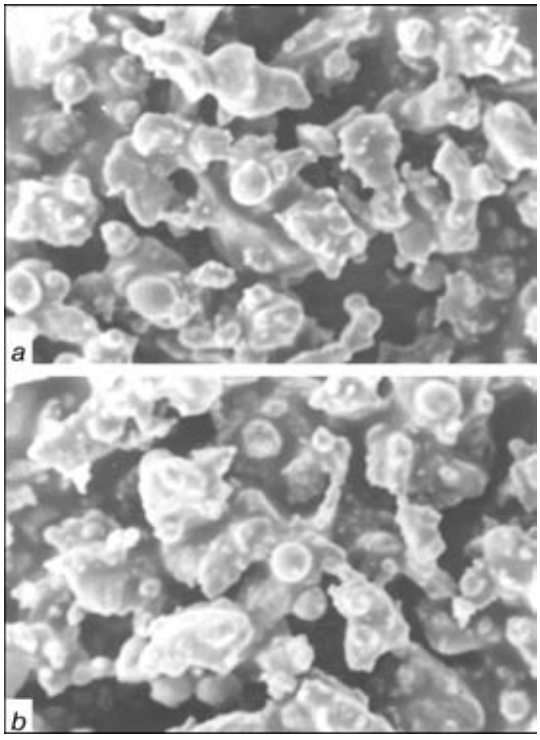

Figure 4. Appearance of the atomized powders with particles ≤ 50 μm in size, melted during AGPS (*a*) and SAGPS (*b*) (×500) (reduced by 2/3)

AGPS and SAGPS, respectively. This is indicative of the correctly selected spraying conditition and the optimal size of the particles.

CONCLUSIONS

1. Phase composition of powders, in particular, the quasicrystalline phase content of the $Al_{63}Cu_{25}Fe_{12}$ alloy, is determined by the rate of cooling of their particles.

2. Powders produced by atomization have a two-phase (ψ + β) composition with a predominant quasicrystalline phase. The water atomized powders have the highest content (up to 74 %) of this phase.

3. Powders produced by crushing of ingots have a considerable phase (β-, ψ-, λ- and θ-phases) and structural heterogeneity. Their ψ-phase content is not more than 43 %.

4. The efficient method for increasing the quasicrystalline phase content of the powders is their annealing at a temperature of 700 °C for 2 h. This results in the formation of the atomized powders with a structure which almost completely consists of the ψ-phase.

REFERENCES

1. Shechman, D., Blech, J., Gratiss, D. *et al.* (1984) Metallic phase with long-range orientation order and translational symmetry. *Phys. Rev. Let.*, **20**, 1951 – 1953.
2. Bancel, P.A., Heincy, P.A. (1986) Icosahedral aluminium-transition-metal alloys. *Phys. Rev.*, **12**, 7917 – 7922.
3. Li, X.Z., Kuo, K.H. (1988) Decagonal quasicrystals with different periodicities along the tenfold axis in rapidly solidified Al–Ni alloy. *Phil. Mag. Let.*, **3**, 167 – 171.
4. Kuo, K.H. (1990) An overview of quasicrystals in aluminium-transition metal alloys. *J. Less. Common Metals*, **1**, 9 – 49.

5. Koster, U., Liu, W., Liebertz, H. *et al*. (1993) Mechanical properties of quasicrystalline and crystalline phases in Al–Cu–Fe alloys. *J. Non-crystalline Solids*, **153/154**, 446 – 452.
6. Klein, T., Berger, C., Magon, D. *et al*. (1988) Proximity of a metal-insulator transition in icosahedral phases of high structural quality. *Phys. Rev. Let*., **22**, 2907 – 2910.
7. Dubois, J.M., Kang, S.S., Massini, Y. (1993) Appheation of quasicrystalline alloys to surface coatings of soft metals. *J. Non-crystalline Solids*, **153/154**, 443 – 445.
8. Dubois, J.M., Kang, S.S., Archambautt, P. *et al*. (1993) *J. Mater. Res*., **8**, 38.
9. Palo, S., Usmani, S., Sampath, S. (1997) Friction and wear behaviour of thermally sprayed Al–Cu–Fe quasicrystal coatings. In: *Proc. of Un. Forum for Scientific and Technological Advances on Thermal Spray.* Ohio: Mater. Park.
10. Borisov, Yu.S., Kharlamov, Yu.A., Sidorenko, S.L. *et al*. (1987) *Thermal spray coatings of powder materials*. Handbook. Kyiv: Naukova Dumka.
11. Sordelet, D.J., Kramer, M.J., Unal, O. (1995) Effect of starting powders on the control of microstructural development of Al–Cu–Fe quasicrystalline plasma-sprayed coatings. *J. Thermal Spray Technology*, **3**, 235 – 244.
12. Gayle, F.W., Shapiro, B.J., Biancaniello, F.B. *et al*. (1992) The Al–Cu–Fe phase diagram: 0 to 25 at.% Fe and 50 to 75 at.% Al — equilibria involving the icosahedral phase. *Metallurgical Transact.*, **23**, 2409 – 2417.
13. Gratias, D., Calvayrac, Y., Devand-Rzensky, J. *et al*. (1993) The phase diagram and structures of the ternary Al–Cu–Fe system in the vicinity of the icosahedral region. *J. Non-crystalline Solids*, **153/154**, 482 – 488.
14. Nechiporenko, O.S., Najda, Yu.I., Medvedovsky, A.B. (1980) *Atomized metal powders*. Kyiv: Naukova Dumka.
15. Rayleigh, D.J. (1944) *Theory of Sound*. Moscow: OGIZ.
16. Sordelet, D.J., Besser, M.F., Anderson, J.E. (1996) Particle size effects on chemistry and structure of Al–Cu–Fe quasicrystalline coatings. *J. Thermal Spray Technology*, **2**, 161 –174.
17. Sordelet, D.J., Besser, M.F. (1996) Particle size effects on chemistry and structure of Al–Cu–Fe quasicrystalline plasma sprayed coatings. In: *Proc. of Practice Solutions for Engineering Problems on Thermal Spray*. Ohio: Mater. Park.

MECHANISM OF RELAXATION OF RESIDUAL STRESSES IN EXPLOSION LOADING OF WELDED JOINTS

V.G. PETUSHKOV, A.G. BRYZGALIN and **V.A. TITOV**
The E.O. Paton Electric Welding Institute, NASU, Kyiv, Ukraine

ABSTRACT

Procedure of approximate calculation of stresses and strains in the trace formed in a relaxing material by a single shock-wave compression is described. The results obtained can be used in determination of parameters of explosion loading to relieve the residual stresses in welded joints of metal structures.

Key words: *residual stresses, explosion treatment, relaxation of stresses, stress-strain trace, shock wave*

To explain the effect of reducing residual stresses using the explosion treatment, the phenomenon of occurrence of a stressed trace in the metal during a shock-wave loading was used in [1]. The appearance of this trace was caused by a relaxation of shear stresses. The further investigations [2] made it possible to establish that a conception about stress-strain trace (SST) interacting with a field of residual stresses and strains in a far zone of explosion and leading to their decrease in a weldment as a whole, is most comprehensive.

Let us make the quantitative assessment of a value of stresses and strains in SST, and also pressures of a shock compression, required for the creation of SST of a preset intensity using the simplest case, i.e. loading of a metal half-space of perfect elasto-plastic properties with a plane wave. However, the results obtained have a more general nature and, to a certain extent, correspond to situations which occur at not-single schemes of loading of relaxing materials [1, 3] realized in practice [4 – 6].

The process of SST formation will be considered using a Hugoniot's curve in coordinates σ_1, ε_y [7], where σ_1 is the stress, and ε_y is the strain in the direction of normal to the shock wave front. In Figure 1 the line $0hH_1$ corresponds to the metal state under loading, $0S$ is the straight line of the hydrostatic compression, $m_1^* r_1$ and $R_1 r_1$ are the lines of elastic and plastic unloading.

If the conditions of a uniaxial deformation are fulfilled at the stage of loading and unloading, then after unloading σ_1^0 the stress-strain state of metal due to relaxation of shear stresses in the shock wave will differ greatly from the initial state. At σ_1^0 the metal will preserve the residual pressure p^0, stipulated by a residual shrinkage deformation ε_1^0 (at pressure σ_1^0 in a shock wave). Moreover, due to σ_1^0, $\sigma_2^0 = \sigma_3^0$ the value

$$p^0 = \frac{\sigma_1^0 + \sigma_2^0 + \sigma_3^0}{3} = \frac{2}{3}\sigma_2^0. \qquad (1)$$

As $p^0 = K\varepsilon_1^0$, then

$$\varepsilon_1^0 = \frac{2}{3}\frac{\sigma_2^0}{K}, \qquad (2)$$

where K is the modulus of a volume compression; σ_2^0 is the residual stress in the shock wave plane.

The value of the residual deformation ε_1^0 can also be obtained from the equation of a direct unloading $m_1^* r_1$ [7]. Here,

$$\sigma_2^0 = \sigma_3^0 = \sigma_d, \qquad (3)$$

where σ_d is the dynamic yield strength, corresponding to a characteristic rate of deformation at the stage of loading and unloading.

Thus, the passing of a single compression wave along the metal and subsequent single loading are accompanied by inducing orthogonal (relative to the wave front plane) areas of residual compression stresses comparable with a dynamic yield strength.

The rate of deformation $\dot{\varepsilon}$ at the shock wave front and the wave of unloading reaches high values [8] when the manifestation of material tough properties

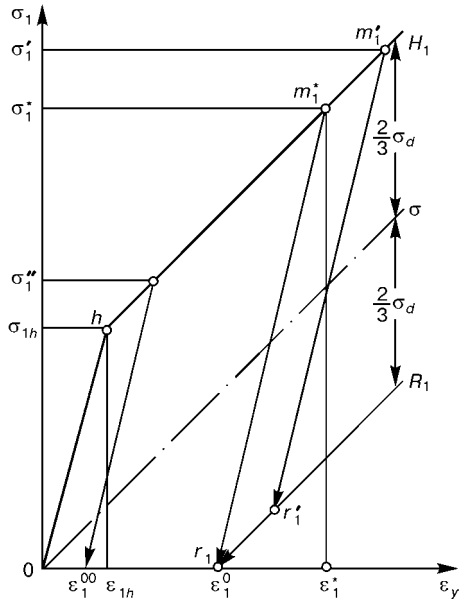

Figure 1. Path of material unloading in the Hugoniot's adiabatic curve in the direction of normal to the front of a plane shock wave

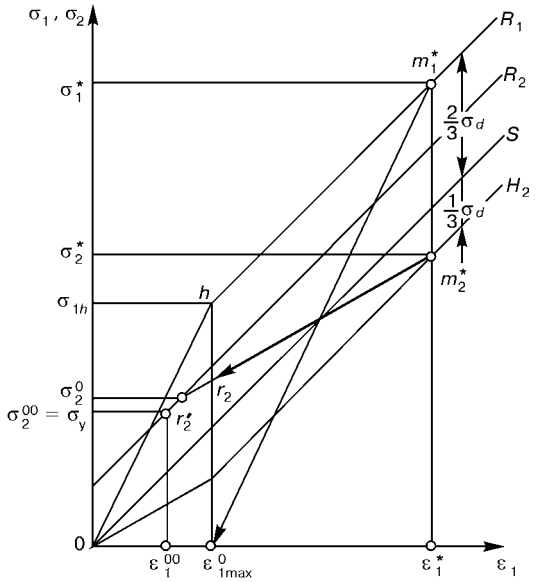

Figure 2. Path of material unloading in the Hugoniot's adiabatic curve in the plane of the shock wave front

becomes evident [9]. However, after unloading completion $\dot{\varepsilon} \approx 0$, and, consequently, the state (3) is unstable, and material becomes overstressed. Due to this, a slow process of the subsequent relaxation of shear stresses should proceed, at which

$$\sigma_2^0 \rightarrow \sigma_2^{00} = \sigma_y \tag{4}$$

(path r_2r_2' in Figure 2). This leads to an additional plastic yielding of the metal in the direction of a free surface of the half-space; metal is expanded that is expressed in «drift» of point r_1' (Figure 1) to the axis of abscissa (points r_2 to point r_2', respectively), until the residual deformation becomes equal to

$$\varepsilon_1^{00} = \frac{2}{3}\frac{\sigma_y}{K}. \tag{5}$$

Thus, the process of formation of SST in the half-space consists of two stages: creation of instantaneous stress-strain state and followed relaxation, leading to an equilibrium (static) state of the metal. There is also a third stage for a body of finite sizes, including its local explosion loading. This stage consists in interaction of an equilibrium SST either with the body boundaries, accompanied by decrease in σ_2^{00} and formation of transverse relative deformation, or (if the unloading is limited) with residual stresses in the near zone of the explosion which leads to the levelling of stresses in the body as a whole.

Let us return to Figure 2. Expression (2) was obtained in assumption that the pressure in the shock wave $\sigma_1 = \sigma_1^*$, where σ_1^* is the pressure at which the unloading is elastic and has a maximum amplitude $\Delta\sigma_{1\max}$ [7]. It is evident, that at $\sigma_1 = \sigma_1' > \sigma_1^*$ the unloading will be two-stage, including a plastic branch r_1r_1', and the instantaneous finite state will be described by the same expression (2). At $\sigma_1 < \sigma_1^*$ the instantaneous residual strain in SST is proportional to the pressure in the shock wave that is followed from the equation of the direct elastic unloading [7]

$$\sigma_1^* = \sigma_1 = (\lambda + 2\mu)(\varepsilon_1' - \varepsilon_1), \tag{6}$$

where λ, μ are the Lame's constants. At $\sigma_1 = 0$

$$\varepsilon_1^0 = \varepsilon_1'' - \frac{\sigma_1''}{\lambda + 2\mu}. \tag{7}$$

Using an evident ratio (Figure 1)

$$\varepsilon_1'' = \varepsilon_{1h} - \frac{\sigma_1'' - \sigma_{1h}}{K}, \tag{8}$$

the expression (7) can be written in the more convenient form (hatching is omitted)

$$\varepsilon_1^0 = \frac{4\mu}{3K(\lambda + 2\mu)}(\sigma_1 - \sigma_{1h}). \tag{9}$$

The value of the instantaneous residual deformation in SST is determined by a value of Hugoniot's yield strength σ_{1h} which in its turn depends greatly on the deformation rate at the shock front [7].

Let us consider further the process of unloading at the areas being orthogonal relative to the plane of the shock wave front (Figure 1, 2). Lines R_1, R_2, $0S$, H_2, $m_2^*r_2$ denote, respectively, a plastic area of adiabatic curve $\sigma_1 - \varepsilon_1$, plastic branch of unloading of stress $\sigma_2 = \sigma_3$, hydrostatic axis, plastic area of adiabatic curve $\sigma_2 - \varepsilon_1$ and elastic branch of unloading of stress $\sigma_2 = \sigma_3$. Line $m_1^*r_1$, corresponds, as before, to the elastic unloading of stress σ_1 which is taken equal to σ_1^* for the simplicity.

The equation of the elastic branch of unloading of stress σ_2 has a form [7]

$$\sigma_2^* - \sigma_2 = \frac{\nu}{1 - \nu}(\sigma_1^* - \sigma_1), \tag{10}$$

where ν is the Poisson's ratio. At the moment of completion of unloading $\sigma_1 = 0$, and the unloading of stress σ_2 is completed in the point r_2 with coordinates $\sigma_2^0\,\varepsilon_1^0$.

It follows from the Mises's yielding conditions

$$\sigma_1^* - \sigma_2^* = \sigma_d. \tag{11}$$

From combination of last expressions and taking into account that

$$\frac{1 - 2\nu}{1 - \nu} = \frac{\sigma_d}{\sigma_{1h}}, \tag{12}$$

we shall obtain

$$\frac{\sigma_2^0}{\sigma_d} = \frac{\sigma_1^*}{\sigma_{1h}} - 1. \tag{13}$$

From (13) the condition of formation of SST is followed:

$$\sigma_1 > \sigma_{1h} = \frac{1 - 2\nu}{1 - \nu} = \sigma_d, \tag{14}$$

which provides the estimate of minimum pressure of the shock wave.

As at $\sigma_1 > \Delta\sigma_{1\max}$ there is also a plastic stage of unloading, except the elastic stage, which leads the metal into a state which is characterized by coordinates of points r_1 and r_2, then the range of effective pressures in the shock wave will be

$$1 < \frac{\sigma_1}{\sigma_{1h}} \le 2,$$

or

$$\frac{1-\nu}{1-2\nu} < \frac{\sigma_1}{\sigma_d} \le \frac{2(1-\nu)}{1-2\nu}. \qquad (15)$$

To determine the order of value of the pressures required for producing, for example, a maximum instantaneous intensity in steel St.3 (C — 0.18 wt.%; Fe — balance), the data of [9, 10] will be used in which value σ_d for the deformation rates $\dot{\varepsilon} \cong 10^4$ s^{-1}, typical of loading with a contact explosion, is evaluated by approximately 900 MPa. Assuming $\nu = 0.28$, we shall obtain

$$1500 < \sigma_1 \le 3000. \qquad (16)$$

This range can be additionally limited if to exclude a part of stresses in SST which is relaxed at the second stage of its formation in accordance with expression (4), i.e.

$$\sigma_2^{00} = \left(\frac{\sigma_1}{\sigma_{1h}} - 1\right)\sigma_d\sigma_y. \qquad (17)$$

Introducing $\sigma_d = \alpha\sigma_y$, from (17) and (15) we shall obtain

$$1 < \frac{\sigma_1}{\sigma_{1h}} \le \frac{1+\alpha}{\alpha}. \qquad (18)$$

Hence, we shall find $1500 < \sigma_1 < 2000$ MPa for steel St.3.

Thus, to produce SST of a maximum equilibrium intensity the pressure in a plane wave should by approximately 25 – 50 % higher than the Hugoniot's limit of elasticity which reaches 1000 – 2000 MPa for most metals [7].

Let us evaluate the sequence of deformations generated in metal by such loading. From (7), taking into account (17), we shall have

$$\varepsilon^*_{1max} = \varepsilon_{1h} + \frac{\sigma_{1h}}{K}, \qquad (19)$$

and from (9) —

$$\varepsilon^*_{1\max} = \frac{4\mu\sigma_{1h}}{3K(\lambda+2\mu)}. \qquad (20)$$

Here, the asterisk denotes maximum deformations which correspond to the conditions of formation of SST of equilibrium intensity, not leading to the plastic unloading.

Assuming for steel St.3 that $K = 1.52\cdot10^5$ MPa, $\lambda = 10^5$ MPa, $\mu = 0.78\cdot10^5$ MPa, $\alpha = 4$, $\sigma_{1h} = 1400$ MPa, we shale have $\varepsilon^*_{1\max} = 1.47$ % and $\varepsilon^0_{1\max} = 0.92$ %; we can also obtain from (7) the value of a plastic constituent of the deformation generated by a single shock compression

$$\varepsilon^*_{1pl} = \frac{\sigma_{1p}}{K} \cong 0.9\ \%,\quad \varepsilon^*_{2pl} = \frac{1}{2}\varepsilon^*_{1pl} \cong 0.45\ \%. \qquad (21)$$

Analysis of SST interaction with a field of residual welding stresses is made using relations obtained in works [1, 11].

Thus, the procedure described on the basis of a single approximation makes it possible to obtain the calculated relation which describes the stresses and strains in SST, which are created by a shock-wave loading. They can be used in determination of parameters of charges of explosive to relieve the residual stresses in welded joints of different classes of materials.

REFERENCES

1. Petushkov, V.G., Fadeenko, Yu.I. (1980) About the explosion treatment of welded joints. *Fizika Goreniya i Vzryva*, **5**, 64 – 68.
2. Petushkov, V.G. (1994) *Explosion treatment of welded joints. Welding and surfacing review*. Ed. by B.E. Paton. Harwood Acad. Publ.
3. Gakkenhaimer, D., Miclovits, D. (1969) Non-steady exciting of elastic half-space by spot loading moving along its surface. *Proc. ASEM, Ser. E, Applied Mechanics*, **3**, 131 – 143.
4. Petushkov, V.G., Kudinov, V.M., Berezina, N.V. (1974) Mechanism of redistribution of residual stresses at explosion loading. *Avtomaticheskaya Svarka*, **3**, 37 – 39.
5. Kudinov, V.M., Trufyakov, V.I., Petushkov, V.G. *et al.* (1976) Parameters of charges of explosive to relieve residual stresses in welded butt joints. *Ibid.*, **1**, 46 – 49.
6. Mikheev, P.P., Trufyakov, V.I., Bushtedt, Yu.P. (1967) Application of pulsed treatment to improve the fatigue life of welded joints. *Ibid.*, **10**, 63 – 64.
7. (1975) *Physics of explosion*. Ed. by K.P. Stanyukovich. Moscow: Nauka.
8. Novikov, S.A., Ivanov, A.G., Vasiliev, L.V. (1966) Elastic-plastic properties of some metals during explosion loading. *Fizika Metallov and Metallovedeniye*, **21**, 452 – 460.
9. Petushkov, V.G. (1969) *Examination of characteristics of strength and ductility of some materials at high-rate tension*. Abstract of thesis for Cand. of Techn. Sci. Kyiv.
10. Stepanov, G.V. (1979) *Elastic-plastic deformation of materials under the action of pulsed loading*. Kyiv: Naukova Dumka.
11. Petushkov, V.G., Pashchin, A.N. (1975) Evaluation of effectiveness of reducing welding stresses by applying external load. *Avtomaticheskaya Svarka*, **7**, 19 – 23.

HYDROGEN CONTENT IN LOW-ALLOYED WELD METAL IN TWIN-ARC WELDING

G.V. BURSKY and **M.M. SAVITSKY**
The E.O. Paton Electric Welding Institute, NASU, Kyiv, Ukraine

ABSTRACT

The effect of twin-arc welding on hydrogen content in low-alloyed weld metal was investigated. It was established that, as compared with a single-arc welding, the twin-arc welding can decrease significantly the amount of $[H]_{diff}$ in weld metal that is due greatly to the peculiarities of the thermal cycle.

Key words: *hydrogen, single-arc weld deposit, twin-arc weld deposit, thermal cycle, cold cracks, humidity of shielding mixture, time of hydrogen evolution*

As is shown in [1 – 3], the twin-arc welding promotes the increase in resistance of metal of the HAZ of hardening steels to the cold cracking. The data of these works prove that the decrease in probability of formation of defects of this type is greatly due to the HAZ structure, which was formed as a result of action of the twin-arc welding thermal cycle on the metal.

In addition, it is known [4, 5] that the hydrogen content in weld metal influences the resistance of HAZ metal to cold cracking. Hydrogen diffuses from the weld to the HAZ and, when its concentration is higher than critical values, causes the initiation of cracks, whose physical origin was studied in [6]. In the first approximation, it is possible to consider that with increase in hydrogen content in weld metal its concentration in HAZ metal is increased, other conditions being equal. In this connection the problem of hydrogen content decrease in weld metal is rather actual in welding steels prone to cracking.

Main regularities of hydrogen absorption with the electrode metal drops and weld pool have been established for the shielded-gas single-arc one- or multipass welding. It is shown that water vapours in the welding zone are one of main its sources [7, 8]. There are no data about the behaviour of this source in the shielded-gas twin-arc welding using the «tandem» method, however, they present practical and scientific interest.

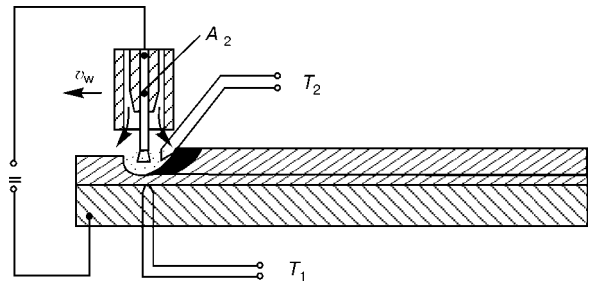

Figure 1. Scheme of recording of thermal cycles in deposition of control samples: A_2 — second arc; T_1, T_2 — thermocouple which records, respectively, thermal cycles in the fusion line and curve of cooling the metal of deposit made with two arcs

Therefore, this work is aimed at the comparative examination of hydrogen content in weld metal in single- and twin-arc welding and different humidity of the shielding gas, containing 80 % Ar + 20 % CO_2.

Samples for measuring hydrogen in weld metal (type II) were manufactured from steel of 14KhN3MDA and 30KhGSA types in accordance with requirements of GOST 23338–91. Deposits on samples were made with 2 mm diameter wires of Sv-10GN2SMD and Sv-08GSMT types (chemical composition of the materials used is given in the Table). Conditions of welding with single and twin arcs were,

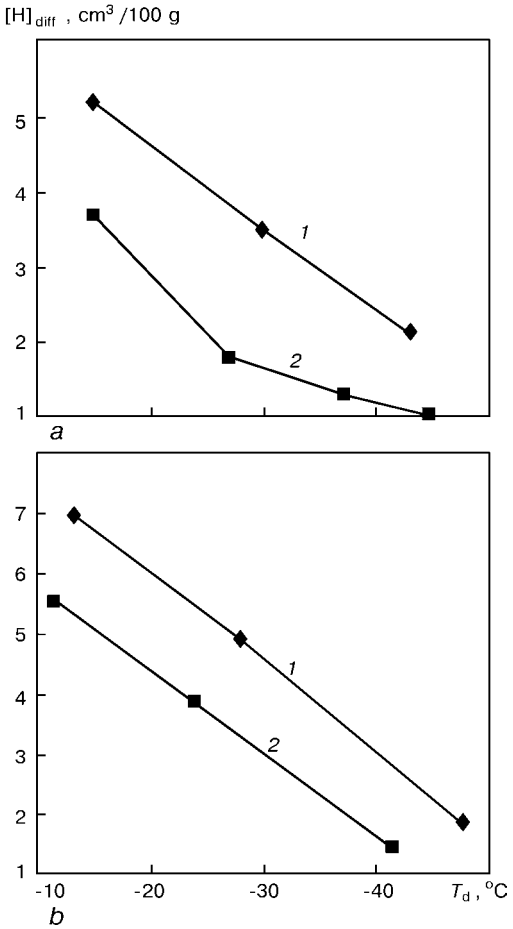

Figure 2. Dependence of content of $[H]_{diff}$ in metal during single- (*1*) and twin-arc (*2*) deposition: *a* — steel of 14KhN3MDA type, wire Sv-10GN2SMD; *b* — steel 30KhGSA, wire Sv-08GSMT

Material	Content of elements, wt.%							
	C	Si	Mn	Cr	Ni	Mo	Cu	Ti
14KhN3MDA	0.14	0.20	0.48	0.85	0.30	0.40	1.60	
30KhGSA	0.28 – 0.34	0.90 – 1.20	0.80 – 1.10					
Sv-10GN2SMD	0.05 – 0.10	0.30 – 0.60	0.50 – 0.80	0.40 – 0.70	2.00 – 2.40	0.40 – 0.70	0.40 – 0.70	
Sv-08GSMT	0.06 – 0.11	0.40 – 0.70	1.00 – 1.30	≤ 0.30	≤ 0.30	0.20 – 0.40		0.05 – 0.12

respectively, the following: I_w = 350 – 360 A, U_a = 32 – 34 V, v_w = 16 m/h; $I_{w1} = I_{w2}$ = 350 – 360 A, $U_{a1} = U_{a2}$ = 32 – 34 V, $v_{w1} = v_{w2}$ = 16 m/h, L_{1-2} = = 250 mm, where L_{1-2} is the distance between the arcs. The humidity of the shielding gas was measured with the help of a special device, in which a silica gel was used as an active substance. The humidity was controlled from the dew point T_d, determined by a condensation method. The humidity of mixture was controlled before and after welding of each sample. Thermal cycles were recorded by tungsten-rhenium thermocouples and an oscillograph of the N-105 type. Here, the thermocouple T_1 was introduced from beneath the sample (Figure 1) and it recorded the thermal cycles at the fusion line, while the second thermocouple T_2 was introduced to the tail part of the molten metal pool and it recorded the cycle of cooling the deposits made by twin arcs.

Content of diffusely-mobile hydrogen $[H]_{diff}$ in weld metal, which was determined by a chromatographic method using a unit OB-2781 according to GOST 23338–91, was selected as a main characteristic of metal saturation with hydrogen. The method of determination of $[H]_{diff}$ assumes deposition of samples, their cooling in water, and then in a liquid nitrogen with a subsequent analysis. The temperature of beginning the sample cooling T_c was controlled by a contact method using a chromel-alumel thermocouple.

The results of determination of amount of $[H]_{diff}$ depending on T_d are given in Figure 2. It is seen that the humidity of the shielding gas in twin-arc welding influences greatly the content of $[H]_{diff}$ in the weld metal. In single-arc welding it is more clearly expressed as compared with the twin-arc welding. However, the content of the residual hydrogen $[H]_r$ in welds made by the single- and twin-arc welding is almost similar. For example, when the shielding gas with T_d = –43 and –45 °C is used, it is ≈ 0.4 cm^3/100 g both in single- and twin-arc welding using wire Sv-10GN2SMD.

Weld metal is saturated with hydrogen during welding when the electrode metal drops are passed through the arc and hydrogen is absorbed by the weld pool. It is difficult to determine the initial content of hydrogen in welds without special instruments, because the process of hydrogen evolution starts even at the stage of the weld pool crystallizing due to an abrupt reduction in its solubility. At a further decrease in temperature the process of hydrogen removal from the weld is continued. The amount of hydrogen evolved depends on a number of factors, including also the time of its evolution.

Metal deposited with one arc is cooled to the temperature 400 °C during time τ_1 (Figure 3, *a*), when a part of hydrogen is evolved to the environment. During twin-arc welding the time of hydrogen evolution from the deposit, made by the first arc, is $\tau_2 > \tau_1$ and depends on the distance between the arcs and the welding speed. The amount of the evolving hydrogen is, respectively, increased. After the heat action of the second arc and deposition of the second bead a part of metal of the first bead is remelted (≈ 60 %), and its lower layers are subjected to a repeated heating

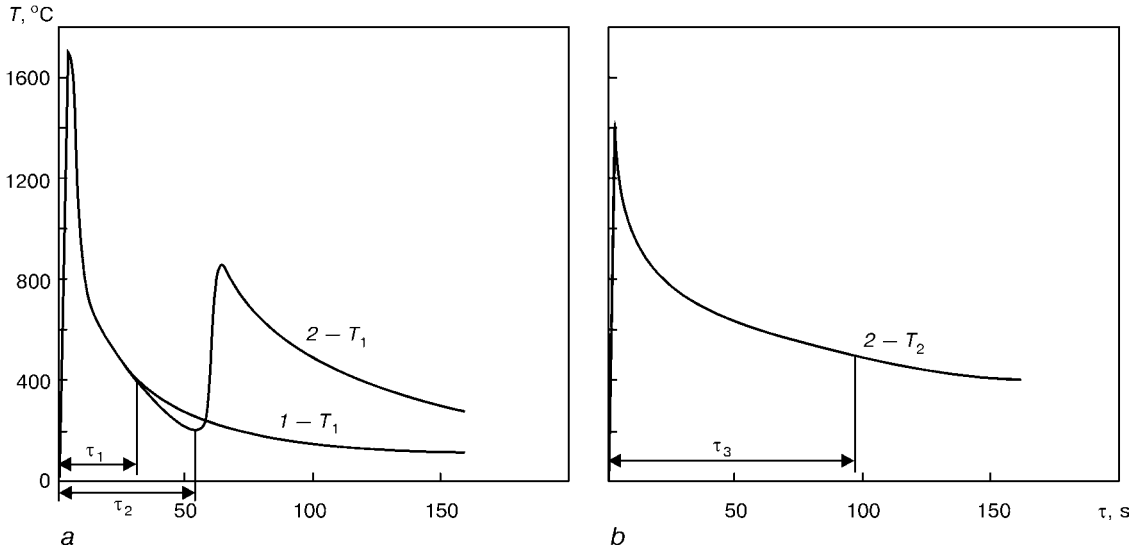

Figure 3. Thermal cycles (*a*), recorded in fusion line (*1* – T_1 – single-, *2* – T_1 – twin-arc deposition) and curve of cooling the deposit (*b*) made with two arcs (*2* – T_2)

to relatively high temperatures. An additional saturation of metal, deposited with the first arc, with hydrogen is occurred. However, the time until the temperature of cooling metal, deposited with two arcs, τ_3 (Figure 3, *b*) is much higher than τ_1, thus leading to more complete removal of hydrogen from the deposit.

Thus, reduction of $[H]_{diff}$ in low-alloyed weld metal made by twin arcs is greatly stipulated by increase in time of hydrogen evolution both from the first bead and from the weld metal as a whole. In addition, the time of evolution depends on the condition of welding with each of the arcs and the distance between them.

CONCLUSIONS

1. Twin-arc welding has a positive effect on content of $[H]_{diff}$ in the low-alloyed weld metal. Amount of $[H]_{diff}$ in weld metal in twin-arc welding, as compared with a single-arc welding, is much lower at all the examined values T_d.

2. Reduction of $[H]_{diff}$ in twin-arc welding is stipulated greatly by increase in time of hydrogen evolution from the weld metal at the stage of its crystallizing and cooling.

3. The amount of hydrogen evolved in twin-arc welding is determined by its thermal cycle. At optimum selection of conditions of welding with each of the arcs and distance between them it is possible to decrease significantly the content of $[H]_{diff}$ in weld metal.

REFERENCES

1. Bursky, G.V., Dovzhenko, V.A., Sterenbogen, Yu.A. (1990) Cold crack resistance of HAZ of 14KhN3MDA steel joints made by narrow-gap twin-arc welding. *Avtomaticheskaya Svarka*, **6**, 20 – 24.
2. Bursky, G.V., Novikova, D.P., Sterenbogen, Yu.A. (1991) Resistance of 14KhN3MDA type steel to a delayed fracture during twin-arc welding. *Ibid*., **8**, 7 – 11.
3. Gorbachev, Yu.I., Metelev, A.V., Kovalevsky, B.A. *et al*. (1985) Twin-arc automatic welding of steel 45 without preheating. *Svarochnoye Proizvodstvo*, **1**, 12 – 13.
4. Kozlov, R.A. (1962) *Hydrogen in welding of hull steels*. Leningrad: Sudostroyeniye.
5. Bursky, G.V., Savitsky, M.M., Novikova, D.P. (1998) Resistance of HAZ of welded joints made from hardening steels to a delayed fracture in twin-arc welding. *Avtomaticheskaya Svarka*, **2**, 35 – 38.
6. Pokhodnya, I.K., Shvachko, V.I. (1997) Physical origin of hydrogen-induced cold cracks in structural steel welded joints. *Ibid*., **5**, 3 – 12.
7. Pokhodnya, I.K. (1972) *Gases in welds*. Moscow: Mashinostroyeniye.
8. Asnis, A.E., Gutman, L.M., Pokladij, O.R. *et al*. (1982) *Welding in mixture of active gases*. Kyiv: Naukova Dumka.